Summer 2019

Dynamic impact induced by tornadoes through simulations based on two-way wind-structure interactions

Tiantian Li

Department: Civil, Architectural and Environmental Engineering

DYNAMIC IMPACT INDUCED BY TORNADOES THROUGH SIMULATIONS BASED ON TWO-WAY WIND-STRUCTURE INTERACTIONS

by

TIANTIAN LI

A DISSERTATION

Presented to the Faculty of the Graduate School of the

MISSOURI UNIVERSITY OF SCIENCE AND TECHNOLOGY

In Partial Fulfillment of the Requirements for the Degree

DOCTOR OF PHILOSOPHY

in

CIVIL ENGINEERING

2019

Approved by:

Dr. Guirong "Grace" Yan, Advisor
Dr. Genda Chen
Dr. Lesley Sneed
Dr. Cesar Mendoza
Dr. Kakkattukuzhy M. Isaac

PUBLICATION DISSERTATION OPTION

This dissertation consists of the following five articles, formatted in the style used by the Missouri University of Science and Technology:

Paper I: Pages 9-49 have been submitted to Journal of Fluids and Structures, entitled: “Influence of turbulence modeling on wind effects of straight-line winds on dome structures”.

Paper II: Pages 50-92 have been submitted to Engineering Structures, entitled: “Investigate the influence of flow structure of a tornado on wind effects”.

Paper III: Pages 93-140 have been accepted by Journal of Wind Engineering and Industrial Aerodynamics, entitled: “Dynamic structural responses of long-span dome structures induced by tornadoes”.

Paper IV: Pages 141-167 are intended for submission to Journal of Structural Engineering, entitled: “Modifying G to consider dynamic impact of tornadoes for achieving tornado-resistance design”.

Paper V: Pages 168-174 have been submitted to Journal of Wind Engineering and Industrial Aerodynamics, entitled: “Improve wind-induced structural responses on a cable-net roof structure using two-way coupled wind-structure-interaction simulation”.

ABSTRACT

Tornadoes have become a significant cause of property damage, injuries and life losses. Investigations of tornadoes indicate that most fatalities were caused by building failure. For example, in the Joplin, MO tornado of 22 May 2011, 161 people were killed, and 84% fatalities were related to building failure. Therefore, it is imperative to develop science-based tornado-resistant building codes, in order to provide a better level of occupant protection from tornadoes and to minimize the tornado-induced damage. This requires in-depth understanding of the wind characteristics of tornadoes and their wind effects on civil structures, based on which design tornadic wind loading can be properly determined. To achieve this, in this study, Computational Fluid Dynamics (CFD) simulations and Computational Structural Dynamics (CSD) simulations are combined for the first time to systematically investigate tornado dynamics and its dynamic impact on civil structures. First, wind effects on large-scale space structures induced by straight-line winds are investigated to fully understand the current building code against wind loads. Then, a real-world tornado is numerically simulated and verified based on full-scale radar-measured data. Based on the verified CFD model, non-stationary wind characteristics of tornadoes and the induced wind effects on large-scale space structures are investigated under different flow structures of tornadoes. Next, CFD and CSD are combined to investigate tornado-induced dynamic responses of large-scale space structures. Finally, tornado-induced dynamic responses of large-scale space structures are compared with that induced by the equivalent straight-line winds, in order to properly modify the equation for calculating the design wind pressure specified in ASCE7-16.

ACKNOWLEDGMENTS

I would like to express my sincere appreciations to my Ph.D. advisor, Dr. Grace Yan. She consistently helped and guided me throughout the entire time of the development of this research work. Her insightful advice and kind encouragement have been directing me into better accomplishments.

I would also like to thank my Ph.D. advising committee members, who are Dr. Genda Chen, Dr. Lesley Sneed, Dr. Cesar Mendoza, and Dr. Kakkattukuzhy M. Isaac. Their valuable suggestions and comments are essential to the accomplishment of the work.

I appreciate the financial support from National Science Foundation under Award No. 1455709. In addition, I would like to thank the support from Dr. Arindam Chowdhury and Dr. Zisis of Florida International University, where the wind tunnel testing of a large-scale dome structure was conducted in their "Wall of Wind (WOW)" facility.

Many thanks go to the strong support and assistance received from our WHAM lab teammates during various research tasks. Thanks also go to the faculties and staff over the years at the Department of Civil, Architectural, and Environmental Engineering at the Missouri University of Science and Technology.

Last, but not the least, I would like to express eternal gratitude to my parents for their everlasting love and support. Special thanks to my beloved husband, Hongya Qu, and my little son, Jay.

TABLE OF CONTENTS

Page

PUBLICATION DISSERTATION OPTION iii

ABSTRACT iv

ACKNOWLEDGMENTS v

LIST OF ILLUSTRATIONS xiii

LIST OF TABLES xix

SECTION

1. INTRODUCTION 1

1.1. BACKGROUND 1

1.2. OBJECTIVE AND SCOPE OF WORK 2

1.2.1. Task 1. 3

1.2.2. Task 2. 4

1.2.3. Task 3. 4

1.2.4. Task 4. 5

1.2.5. Task 5. 5

1.3. INTELLECTUAL MERITS 6

1.4. DISSERTATION ORGANIZATION 7

PAPER

I. INFLUENCE OF TURBULENCE MODELING ON WIND EFFECTS OF STRAIGHT-LINE WINDS ON DOME STRUCTURES 9

ABSTRACT 9

1. INTRODUCTION 10

2. DOME GEOMETRY AND EXPERIMENTAL SETUP 16

2.1. DOME DIMENSIONS 16

2.2. CONFIGURATION OF THE WOW FACILITY 16

2.3. EXPERIMENTAL SETUP 17

3. TESTING RESULTS AND DISCUSSION 21

3.1. MEAN VELOCITY PROFILE 21

3.2. TURBULENCE INTENSITY 22

3.3. CONTOUR PLOTS OF MEAN PRESSURE COEFFICIENT 23

3.3.1. Open Terrain 24

3.3.2. Suburban Terrain. 25

3.4. FORCE AND MOMENT COEFFICIENT 26

3.5. REYNOLDS NUMBER 28

4. NUMERICAL SIMULATION OF WIND FIELD PRODUCED IN WOW AND DISCUSSION OF RESULTS 29

4.1. COMPUTATIONAL DOMAIN 29

4.2. DETERMINATION OF VELOCITY INPUT 29

4.3. TURBULENCE MODELING AND OTHER CFD SIMULATION SETUP .. 31

4.4. GRID INDEPENDENCE STUDY 33

4.5. INFLUENCE OF DIFFERENT TURBULENCE MODELS 35

5. NUMERICAL SIMULATION OF WIND TUNNEL TESTING OF THE DOME STRUCTURE AND DISCUSSION OF RESULTS 37

5.1. GRID INDEPENDENCE STUDY 37

5.2. ALONG-WIND VELOCITY IN THE WIND FIELD 39

5.3. STATIC PRESSURE IN THE WIND FIELD 40

5.4. WIND PRESSURE DISTRIBUTION ON THE DOME SURFACE 42

6. CONCLUSIONS 45

ACKNOWLEDGEMENTS 47

REFERENCES 47

II. INVESTIGATE THE INFLUENCE OF FLOW STRUCTURE OF A TORNADO ON WIND EFFECTS 50

ABSTRACT 50

1. INTRODUCTION 51

2. SIMULATION OF TORNADIC WIND FIELD 56

2.1. CIVIL STRUCTURE CONSIDERED IN THIS STUDY 56

2.2. REAL-WORLD TORNADO SIMULATED IN THIS STUDY 57

2.3. ALL SIMULATED CASES AND SIMULATION SETUP 58

2.4. SIMULATION OF TORNADO TRANSLATION 61

3. VERIFICATION OF THE APPLIED CFD SIMULATION STRATEGIES 61

3.1. PROFILE OF TANGENTIAL VELOCITY (V_t) 62

3.2. RADIAL REYNOLDS NUMBER (R_{e_r}) AND SWIRL RATIO (S) 63

3.3. VERTICAL FLOW STRUCTURE 64

4. COMPARISON ON WIND CHARACTERISTICS OF TORNADIC WIND FIELD 66

4.1. TORNADIC FLOW STRUCTURE 67

4.2. TANGENTİAL VELOCİTY (V_t) 69

4.3. TURBULENCE İNTENSİTY (TI) 72

4.4. STATIC PRESSURE 74

5. COMPARISON ON TORNADO-INDUCED WIND EFFECTS ON THE DOME STRUCTURE 76

5.1. SURFACE PRESSURE 76

5.2. FORCE AND MOMENT COEFFICIENTS 82

6. CONCLUSIONS 86

ACKNOWLEDGEMENTS 88

REFERENCES 88

III. DYNAMIC STRUCTURAL RESPONSES OF LONG-SPAN DOME STRUCTURES INDUCED BY TORNADOES 93

ABSTRACT 93

1. INTRODUCTION 94

2. DOME STRUCTURE 99

3. SIMULATION OF TORNADIC WIND FIELD 100

3.1. TORNADOES SIMULATED IN THIS STUDY 100

3.2. COMPUTATIONAL DOMAIN 101

3.3. BOUNDARY CONDITION AT VELOCITY INLET 102

3.4. SIMULATED CASES 103

3.5. SIMULATION OF TORNADO TRANSLATION 103

3.6. MESH STRATEGY AND DYNAMIC MESH ZONES 104

3.7. SIMULATION SETUP 107

4. VERIFICATION OF THE APPLIED CFD SIMULATION STRATEGIES FOR EF3 TORNADO 108

5. MODAL ANALYSIS RESULTS 112

5.1. FINITE ELEMENT MODEL 112

5.2. NATURAL FREQUENCIES AND MODE SHAPES 113

6. WIND EFFECTS INDUCED BY TORNADO 115

6.1. WIND DIRECTION OF THE FLOW FIELD 115

6.2. WIND PRESSURE ON DOME SURFACE 116

7. TORNADO-INDUCED STRUCTURAL RESPONSES..... 121

7.1. DISPLACEMENT RESPONSES..... 121

7.2. ACCELERATION RESPONSES 125

7.3. INDUCED STRESS ON SHELLS AND BEAM MEMBERS 127

8. CONCLUSIONS 133

ACKNOWLEDGEMENTS 135

REFERENCES..... 135

IV. MODIFYING G TO CONSIDER DYNAMIC IMPACT OF TORNADOES FOR ACHIEVING TORNADO-RESISTANCE DESIGN 141

ABSTRACT 141

1. INTRODUCTION..... 141

2. REVIEW ON CURRENT WIND DESIGN PRACTICE AGAINST TORNADOES..... 144

2.1. RELATED EQUATIONS FOR CALCULATING TORNADIC WIND PRESSURE 144

2.2. THE DETERMINATION OF GUST-EFFECT FACTOR (G)..... 145

3. PROPOSED SOLUTION..... 148

4. SIMULATION OF WIND FIELDS..... 149

4.1. SIMULATION OF TORNADIC WIND FIELD..... 149

4.1.1. CFD Simulation Model. 149

4.1.2. Velocity Input at the Velocity Inlet. 152

4.2. SIMULATION OF EQUIVALENT STRAIGHT-LINE WIND FIELD 153

4.2.1. CFD Simulation Model. 153

4.2.2. Velocity Input at the Velocity Inlet. 155

5. COMPARISON BETWEEN TORNADIC WINDS AND STRAIGHT-LINE WINDS 155

5.1. WIND PRESSURE ON THE DOME SURFACE 155

5.2. DYNAMIC RESPONSES OF THE DOME STRUCTURE 158

6. DETERMINATION OF *G* 162

7. CONCLUSIONS 163

ACKNOWLEDGEMENT 165

REFERENCES 165

V. IMPROVE WIND-INDUCED STRUCTURAL RESPONSES ON A CABLE-NET ROOF STRUCTURE USING TWO-WAY COUPLED WIND-STRUCTURE-INTERACTION SIMULATION 168

ABSTRACT 168

1. INTRODUCTION 168

2. METHODOLOGY 170

3. NUMERICAL SIMULATION SETUP 171

4. NUMERICAL RESULTS 172

5. CONCLUSIONS 173

ACKNOWLEDGEMENTS 174

REFERENCES 174

SECTION

2. SUMMARY, CONCLUSIONS AND RECOMMENDATIONS 175

2.1. SUMMARY OF RESEARCH WORK 175

2.2. CONCLUSIONS 176

2.3. RECOMMENDATIONS 180

BIBLIOGRAPHY 182

VITA 183

LIST OF ILLUSTRATIONS

PAPER I Page

Figure 1. Stockholm Globe Arena. 11

Figure 2. Reno/Virginia peak dome failure. 11

Figure 3. The scaled dome model tested in the WOW facility. 17

Figure 4. The WOW facility used for experimental investigation. 18

Figure 5. Top view of the testing section. 19

Figure 6. Experimental setup to achieve two different terrain configurations. 19

Figure 7. Cobra Probe coordinate system. 19

Figure 8. Measurement of wind velocity profile for open terrain. 20

Figure 9. Distribution of pressure taps on the dome surface. 21

Figure 10. The obtained mean velocity profile for open terrain. 22

Figure 11. Power spectral density of the time history of along-wind velocity for 95% throttle at 0.67 m (dome apex) over open terrain. 23

Figure 12. TI along height under 95% throttle for open terrain. 24

Figure 13. Pressure coefficients over open terrain. 25

Figure 14. Pressure coefficients over suburban terrain. 26

Figure 15. Computational domain applied to simulate the wind field produced in WOW (unit: m). 31

Figure 16. Comparison of the regression equation (“Regr. eq.”) and the mean velocity profile obtained from the wind tunnel testing (“Exp.”). 31

Figure 17. Structured mesh of the computational domain without the dome model present (Mesh 1). 34

Figure 18. Mean along-wind velocity profile among the three cases with different meshes. 35

Figure 19. Mean along-wind velocity profile among the three cases with different turbulence models, regression equation ("Regr. eq."), and the wind tunnel testing data ("Exp."). 36

Figure 20. Computational domain to simulate the wind tunnel testing of the dome model in WOW (unit: m). 37

Figure 21. Grid arrangement of the computational domain with the dome model present (Mesh 1). 38

Figure 22. Pressure coefficients on the dome surface over open terrain at 95% throttle. 39

Figure 23. Contour plot of the along-wind velocity in the wind field on the XZ plane where Y=0. 41

Figure 24. Contour plot of static pressure in the wind field on XZ plane where Y=0. 42

Figure 25. Pressure coefficient over open terrain at 95% throttle. 43

Figure 26. Pressure distribution on the dome surface superimposed on the streamline of the along-wind velocity around the dome model. 44

PAPER II

Figure 1. Spherical dome structure. 57

Figure 2. Computational domains of the simulated tornadic wind fields (unit: m). 60

Figure 3. Schematic diagram of the simulation of tornado translation. 62

Figure 4. Comparison of the tangential velocity profiles extracted from the CFD simulation (Case 1) and the radar-measured data. 63

Figure 5. Swirl ratio at representative heights for Case 1. 65

Figure 6. Schematic diagrams of tornadic flow structures on the vertical plane. 65

Figure 7. Instantaneous flow structure of the simulated tornado in Case 1. 66

Figure 8. Instantaneous flow structure on the vertical plane of the tornadic flow 68

Figure 9. Instantaneous horizontal flow structure of the tornadic wind field at the elevation of 25 m. 69

Figure 10. Instantaneous contour plots of tangential velocity on the horizontal plane at the elevation of 25 m. 70

Figure 11. Time- and space-averaged profile of tangential velocity along radial distance. 70

Figure 12. Instantaneous profile of tangential velocity along radial distance at the elevation of 25 m. 71

Figure 13. Contour plot of tangential velocity on the vertical plane. 71

Figure 14. Comparison of turbulence intensity between Case 1 and Case 2. 73

Figure 15. Time histories of tangential velocity of the double-celled tornado. 73

Figure 16. Time histories of tangential velocity of the single-celled tornado. 74

Figure 17. Instantaneous contour plot of static pressure on the horizontal plane at the elevation of 25 m. 75

Figure 18. Static pressure profile as a function of radial distance. 75

Figure 19. Surface pressure for the double-celled tornado. 77

Figure 20. Surface pressure for the single-celled tornado. 79

Figure 21. Instantaneous contour plot of static pressure on a 12.5-m-high horizontal plane of the wind field and on the dome surface induced by the double-celled tornado. 80

Figure 22. Instantaneous contour plot of static pressure on a 12.5-m-high horizontal plane (except as otherwise specified) of the wind field and on the dome surface induced by the single-celled tornado. 81

Figure 23. Time history of the surface pressure at the dome apex induced by the double-celled tornado. 82

Figure 24. Time history of the surface pressure at the dome apex induced by the single-celled tornado. 82

Figure 25. Forces acting on the dome structure. 84

Figure 26. Force coefficients. 84

Figure 27. Moments acting on the dome structure. 85

Figure 28. Moment coefficients. 86

PAPER III

Figure 1. Spherical dome structure. 100

Figure 2. Computational domain of the simulated tornadic wind field. 101

Figure 3. Comparison between regression equation and radar-measured data of velocity profiles. 102

Figure 4. Schematic diagram of the simulation of tornado translation. 104

Figure 5. Hybrid meshes of the computational domain. 106

Figure 6. Comparison of numerically-simulated and radar-measured tangential velocity profile as a function of radial distance. 108

Figure 7. Numerically-simulated velocity profile as a function of height. 109

Figure 8. Time history of the velocity components at a point in space. 110

Figure 9. Static pressure profile as a function of radial distance. 111

Figure 10. Swirl ratio at representative heights for EF3 tornado. 112

Figure 11. FEM of the dome structure. 113

Figure 12. Representative mode shapes of the dome structure with the beam frame and shell. 114

Figure 13. Streamline of the resultant wind velocity. 116

Figure 14. Surface pressure for EF3 tornado. 118

Figure 15. Time history of tornado-induced surface pressure. 119

Figure 16. Surface pressure at the dome apex. 119

Figure 17. Deformation profile of the entire structure for EF3 tornado. 122

Figure 18. Deformation profile of the beam frame for EF3 tornado. 123

Figure 19. Time history of maximum resultant displacement on the beam frame. 124

Figure 20. Time history of displacement components in three directions at the dome apex. 125

Figure 21. Time history of acceleration components in three directions at the dome apex. 126

Figure 22. Time history of acceleration components in three directions at other representative locations. 127

Figure 23. Contours of von-Mises stress for shells for EF3 tornado. 128

Figure 24. Time history of maximum von-Mises stress of the shells. 129

Figure 25. Contours of minimum combined stress of the beam frame for EF3 tornado. 130

Figure 26. Contours of maximum combined stress of the beam frame for EF3 tornado. 131

Figure 27. Time history of maximum and minimum values of the two combined stresses of the beam frame 131

Figure 28. Time history of combined and von-Mises stresses at dome apex. 132

Figure 29. Time history of combined and von-Mises stresses at other representative locations 133

PAPER IV

Figure 1. Spherical dome structure. 150

Figure 2. (a) Computational domain of the simulated tornadic wind field; (b) Schematic diagram of the simulation of tornado translation. 151

Figure 3. Mesh strategies of the computational domain. 152

Figure 4. The averaged tangential velocity profile along radial distance at the elevation of 25 m. 153

Figure 5. Computational domain and boundary conditions of the equivalent straight-line wind field. 154

Figure 6. Mesh strategies of the computational domain. 155

Figure 7. Peak surface pressure at each time instant induced by: (a) Tornadic winds; (b) Straight-line winds. 156

Figure 8. Wind pressure on the dome surface induced by tornadic winds. 157

Figure 9. Wind pressure on the dome surface induced by straight-line winds. 158

Figure 10. Time history of surface pressure induced by tornadic winds. 159

Figure 11. Time history of surface pressure induced by SL winds. 159

Figure 12. FEM of the dome structure in CSD simulations. 160

Figure 13. Maximum displacement of the dome structure at each time instant induced by: (a) Tornadic winds; (b) Straight-line winds. 161

Figure 14. Deformation profile of the dome structure induced by: (a) Tornadic winds; (b) Straight-line winds. 161

Figure 15. Time history of displacement induced by tornadic winds. 162

Figure 16. Time history of displacement induced by SL winds. 162

Figure 17. 3-s averaged maximum displacement. 164

Figure 18. Definition of U_{3s} and $\overline{U}_{3s}$. 164

Figure 19. Time history of G_{3s} 164

PAPER V

Figure 1. (a) CFD model; (b) Finite element model of the cable-net structure. 172

Figure 2. (a) Streamline of velocity on the vertical plane; (b) Wind pressure distribution on the roof surface; (c) Time history of displacement at the center of the roof. 173

LIST OF TABLES

PAPER I Page

Table 1. Force and moment. 27

Table 2. Force coefficient and moment coefficient. 28

Table 3. Turbulence model equations. 32

Table 4. Meshing strategies of the wind field without the dome model present. 34

PAPER II

Table 1. Mathematical expression of analytical tornado models. 53

Table 2. All cases simulated in this study. 58

PAPER III

Table 1. Natural frequencies of the dome structure. 114

1. INTRODUCTION

1.1. BACKGROUND

A tornado is a rotating column of air extending from a cumulonimbus cloud to the ground. It is claimed to be one of the most violent natural hazards and strikes the United States very frequently, about 1200 tornadoes per year (Verbout et al., 2006). In recent years, it have become a significant cause of , injury, loss of life and property damage in the United States, contributing $10B annually to the nation's loss portfolio. In 2011 only, the tornado-induced property loss exceeded $20B and 550 people were killed (Lott et al., 2012; FEMA, 2012).

In particular, the Joplin, MO tornado of 22 May 2011 killed 161 people, injured 1150 people and led to $2.8B of property damage (Wurman, 2002). It is claimed to be the costliest tornado on record. The El Reno, OK tornado of 31 May 2013 took the lives of an experienced tornado researcher, Tim Samaras, his son Paul, and their TWISTEX colleague, as well as an amateur storm chaser and four others, injured 158 people, and resulted in $35-40M of property loss (Wurman et al., 2014). It is claimed to be the largest tornado ever documented. The "Tri-state" tornado of 18 March 1925 killed 695 people.

In fact, tornadoes have killed more people historically than hurricanes. This is because the generation of tornadoes cannot be predicted. Many tornadoes occur in the evening of sunny, clear days. They are unexpected. The average warning time of a tornado is roughly 8 to 10 minutes. Obviously, there is no way to evacuate the community in 8-10 minutes. From another perspective, due to the unpredictability of a tornado path, the community may not want to be evacuated before an impending tornado,

as it is unknown where exactly a tornado will occur and in which way exactly a tornado will go. If there is not a public tornado shelter in their community, the only way for people to survive is to make sure that the building they stay in, at least a designated area, is strong enough. Therefore, to provide a better level of occupant protection from tornadoes and minimize the tornado-induced damage, eventually achieving tornado-ready and tornado-resilient communities, it is important to develop science-based tornado-resistant building codes, which requires in-depth understanding of tornado-structure interaction.

The civil structures of interest investigated in this study are two representative large-scale space structures (dome structures and cable-net roof structures). Large-scale space structures are considered here because this type of structure is usually built as public assembly venues that hold many people. They are subjected to significant wind loads because of large surface areas. Failure of this type of structure may endanger the safety of hundreds or even thousands of people. Therefore, it is important to quantify the tornadic wind loads on this type of structure, eventually achieving tornado-resistant design of large-scale space structures.

1.2. OBJECTIVE AND SCOPE OF WORK

Although the static impact of tornadoes (mean aerodynamic loading) on civil structures has been widely studied (Selvam and Millett, 2003), the research on the non-stationary characteristics of tornadoes and their dynamic impact on civil structures has been lacking, which has prevented the tornadic wind loading from being properly determined. To bridge this research gap, the research objective of this study is to

investigate the tornado dynamics and its dynamic impact on civil structures using the combination of Computational Fluid Dynamics (CFD) simulations and Computational Structural Dynamics (CSD) simulations. The obtained research finding will help to develop science-based building codes for tornado-resistance design and to improve disaster resilience in Tornado Alley.

To achieve the proposed research objective, the following research tasks have been planned:

1.2.1. Task 1. Characterize the winds effects on dome structures under straight-line winds using systematic CFD simulations, in which the influence of turbulence modeling on the wind effects is investigated. To verify the accuracy of the CFD simulations, wind tunnel testing of a large-scale dome model (1/60) is carried out in the WOW facility at Florida International University. Then, the wind tunnel testing is numerically simulated. Three different turbulence models, Spalart-Allmaras, shear stress transport (SST) k-ω, and large eddy simulation (LES) models, are employed in the CFD simulations to investigate their influence on the wind effects acting on the dome structure. One purpose to conduct this study is due to the fact that the current building design code against wind loads (the related equation to calculate the design pressure on structural surface ASCE7-16) is still based on straight-line winds (ASCE, 2016). To develop tornado-resistant design code, it is necessary to compare the wind effects induced by tornadic winds and those induced by straight-line winds; then, the obtained findings can be used to properly modify the existing pressure-calculating equation in ASCE7-16 (for straight-line winds) to determine the tornado-induced wind pressure. In addition, considering that CFD simulations still demand validation at this stage (Blocken,

2014), the high-quality wind tunnel testing data obtained in WOW allows the adjustment of CFD simulation setup to be practiced, which lays a good foundation on adjusting CFD simulation setup under tornadic winds to obtain good CFD simulation results under tornadic winds.

1.2.2. Task 2. Verify the CFD simulation of tornadic wind fields based on full-scale radar-measured data from a real-world tornado and investigate the influence of flow structure of a tornado on wind effects acting on civil structures. CFD simulations offer an effective and economic way to characterize tornadic wind fields, as an alternative to laboratory simulations. However, its accuracy and effectiveness should be verified first before its wide application. A real-world F4 tornado, the Spencer, SD tornado of 30 May 1998, is numerically simulated using CFD simulations and verified based on the associated full-scale radar-measured data. Then, the validated CFD model is used to investigate how the number of cells in the flow structure affects the wind effects acting on civil structures. It will also provide a good basis for the investigation of structural responses.

1.2.3. Task 3. Determine dynamic responses induced by tornadic winds through the combination of CFD simulations and CSD simulations. A large-scale dome structure is taken as an example to investigate tornado-induced dynamic responses. The dome structure is placed into the simulated tornadic wind field to quantify tornadic wind loads on the dome surface. The velocity profiles applied at the velocity inlet are scaled by 150%, 130%, 100%, and 87% to simulate tornadoes with different intensities, that is, EF5, EF4, EF3, and EF2 tornadoes. To simulate the translation of the tornado, rather than having the tornado moved, the structure is assumed to move in the opposite direction. To

achieve this, the dynamic mesh technique is turned on in the CFD simulations. Then, the obtained time histories of wind pressure from CFD simulations are imported onto the finite element model (FEM) of the dome structure; And a nonlinear, transient CSD analysis is conducted to obtain structural responses at each time instant, considering all geometric (large strain/deformation) and material nonlinearity.

1.2.4. Task 4. Investigate dynamic wind effects induced by the non-stationary characteristics of tornadoes and reflect this on associated parameters (gust-effect factor, G) in ASCE 7-16 tornadic wind loading calculation. Current wind design practice against tornadoes is first reviewed on related equations for calculating tornadic wind pressure and on the determination of G. Then, CFD simulations of tornadic wind field and equivalent straight-line wind field are conducted and compared, in order to investigate the non-stationary characteristics of tornadic wind field and their dynamic impact on civil structures. Finally, based on the dynamic structural responses, G is calculated to reflect the dynamic impact of tornadoes on the structure and compared to the G defined in ASCE 7-16.

1.2.5. Task 5. Investigate the tornado-structure interaction on a cable-net roof structure using numerical simulations based on two-way coupled wind-structure interaction (WSI) under straight-line winds. For the structures whose structural deformation is large and will affect the wind field, the interaction between the structure and the wind field should be considered. To illustrate this, a flexible cable-net roof structure is modeled under straight-line winds to investigate how the wind field and the structure will interact with each other. The two-way coupled WSI is achieved by coupling the flow analysis (CFD simulation) and the finite element analysis (CSD simulation).

Herein, after the wind pressure on structural surface at one time step is obtained from CFD simulation, it will be transferred to the finite element model of the structure though wind-structure interface. Then, a nonlinear, transient CSD analysis will be conducted to obtain structural responses for this time step. Next, the obtained structural displacements will be transferred back to the CFD solver to set up the new boundary condition of the wind field for the next cycle of CFD simulation. A number of cycles are conducted to reach the desired structural responses. The findings of this study will improve the understanding of two-way coupled WSI and will facilitate two-way WSI under tornadic winds, leading to more accurate tornadic wind loading.

This study will increase fundamental knowledge on the tornado-structure interaction and tornadic wind effects, and help to properly determine design tornadic wind loading, which can be used for tornado-resistance design of new buildings and reinforcement of existing buildings. This will contribute to the NIST's mission of improving building codes and standards against tornadoes and the specific mission of Disaster Resilience Programs. The implementation of the research findings will significantly improve occupant protection by preventing civil structures from collapse or severe damage and reduce property loss, ultimately achieving tornado-ready and tornado-resilient communities.

1.3. INTELLECTUAL MERITS

This study will thoroughly investigate wind effects on civil structures and tornado-structure interactions through systematic CFD and CSD simulations. First, wind tunnel testing is conducted on a large-scale dome model, which allows a better resolution

of pressure distribution on structural surface and hence accurate evaluations of wind effects on civil structures. Second, non-stationary characteristics of tornadic winds and their dynamic impact on civil structures are systematically investigated, filling a fundamental knowledge gap. It will potentially provide more realistic design tornadic wind loading for the development of tornado-resistant design code. Third, the coupling of CFD simulation and CSD simulation (finite element analysis) allows the consideration of wind-structure interaction. This will improve the quantification of tornadic wind loading on flexible structures.

1.4. DISSERTATION ORGANIZATION

This dissertation includes three sections. Section 1 gives a brief introduction to the subject area and explains the need for the current research study. The first section also presents the overarching objective and scope of work of the investigation.

Section 2 presents the results of this study in the form of five manuscripts: four journal papers are under review and one journal paper is intended to submit. The first paper presents wind tunnel testing and CFD simulations of wind effects on dome structures induced by straight-line winds, in which the influence of turbulence modeling on the wind effects is discussed. The second paper presents the validation and verification of CFD simulations of tornadic wind fields and the investigation of the influence of flow structure of a tornado on wind effects. Both single-cell, single vortex and double-cell, single vortex flow structures are explored. The third paper presents dynamic responses of a large-scale dome structure induced by tornadic winds through the combination of CFD simulation and nonlinear, transient structural analyses. The fourth paper calculates gust-

effect factor for tornadic wind field to reflect its non-stationary characteristics and induced dynamic impact on civil structures, aiming to determine the design tornadic wind pressure more accurately. CFD simulations of both tornadic wind field and equivalent straight-line wind field are conducted and compared. The fifth paper presents the dynamic responses of a cable-net roof structure using numerical simulations based on two-way coupled wind-structure interaction (WSI) under straight-line winds. The findings of this study will improve the understanding of two-way WSI and will facilitate two-way WSI under tornadic winds, leading to more accurate tornadic wind loading.

Section 3 summarizes the conducted research work and conclusions of the obtained research findings, and proposes future research.

PAPER

I. INFLUENCE OF TURBULENCE MODELING ON WIND EFFECTS OF STRAIGHT-LINE WINDS ON DOME STRUCTURES

Tiantian Li, Yi Zhao, and Guirong Yan

ABSTRACT

In this study, systematic Computational Fluid Dynamics (CFD) simulations are conducted to investigate the influence of turbulence modeling on wind effects acting on dome structures induced by straight-line winds. First, wind tunnel testing of a large-scale dome model (1/60) is carried out in the WOW facility at Florida International University. Then, the wind tunnel testing is numerically simulated. Three different turbulence models, Spalart-Allmaras, shear stress transport (SST) k-ω, and large eddy simulation (LES) models, are employed in the CFD simulations to investigate their influence on the wind effects acting on the dome structure. The distribution of the along-wind velocity and the static pressure in the entire wind field indicates that the LES model provides detailed, turbulent flow condition while the Spalart-Allmaras and SST k-ω models provide the averaged flow condition. With respect to the wind pressure distribution on the dome surface and the total suction force, the simulated results associated with the Spalart-Allmaras model match the wind tunnel testing the best and the LES model the poorest. A close examination of the pressure distribution on the leeward side shows that the Spalart-

Allmaras model predicts the boundary layer separation with the highest accuracy and hence the most accurate wind pressure distribution. In summary, when averaged quantities are targeted to be matched, the Spalart-Allmaras model is a better option than the LES model.

1. INTRODUCTION

A spherical dome structure is a common geometric shape of long-span space structures for public assembly venues (e.g. sport stadiums, auditoriums, and shopping malls), due to the fact that this type of structure offers little spatial obstruction, material efficiency and economic benefit. Figure 1 presents an example of an arena in a spherical shape in Stockholm, Sweden. Since the outer surface area of the spherical dome is large, this type of structure can be subjected to significant wind loads. Also, its long-span and lightweight roofs can be subjected to severe vibrations under strong winds. In fact, this type of structure has been found to be collapsed during strong winds. For example, the Reno/Virginia peak dome failure as shown in Figure 2, which was caused by strong winds on Dec. 19, 2008.

To avoid structural failure and to ensure the safety of this type of structure, proper wind resistance design is necessary, which demands the comprehensive understanding of the aerodynamic behavior of spherical dome structures and corresponding wind loads. Experimental and numerical studies have been conducted to investigate aerodynamics of spherical dome structures in straight-line winds. Literature of direct relevance to this study is briefly reviewed as below.

Figure 1. Stockholm Globe Arena.

Figure 2. Reno/Virginia peak dome failure (by NWS Reno Electronics Team).

Experimental investigations were first undertaken in wind tunnels by researchers (Maher, 1965; Blessman, 1971; Taniguchi et al., 1982; Newman et al., 1984; Savoy and Toy, 1986) to obtain mean pressure on spherical dome structures. Then, fluctuations of pressure about mean pressure with time were characterized using wind tunnel testing (Taylor, 1991; Ogawa, 1991). Later on, the influence of dome surface roughness on the pressure distribution was investigated, and it was found that the dome structure with a rougher surface was subjected to lower suctions over the apex of the dome and higher suctions in the wake region on the leeward side (Letchford and Sarkar, 2000). The

influence of Reynolds number on the mean pressure coefficient was also studied using wind tunnel testing and it was found that the mean pressure coefficient became independent of Reynolds number when it fell into 1.0×10^5 and 2.0×10^5 (Cheng and Fu, 2010). Apart from the mean and fluctuating wind pressures, the spectra of the wind pressure acting on spherical dome structures were also investigated (Qiu et al., 2011). The results indicated that the wind pressure spectra were attributed from both the flow turbulence and the dome-generated turbulence that was induced by the boundary layer separation over the dome apex and the vortex shedding in the wake.

Besides wind tunnel testing, numerical simulations were also carried out to understand the aerodynamic behavior of spherical dome structures. Due to the curved surface of a spherical dome structure, the boundary layer separation points cannot be identified based on geometry. Computational Fluid Dynamics (CFD) simulations offer an insight into the boundary layer separation point and the characteristics of the flow near the separation location. However, the simulated wind field depends on the selection of turbulence models, turbulence intensities, surface roughness, and boundary conditions, and so on. Meroney et al. (2002) examined the influence of surface roughness on the mean pressure coefficient of dome structures in a straight-line wind field using CFD simulations, and it was concluded that the surface roughness reduced mean suctions over the surface of the domes, which was consistent with the wind tunnel testing performed by Letchford and Sarkar (2000). Tavakol et al. (2010; 2015) investigated the influence of turbulence modeling on the velocity profile along height in the wake behind a spherical dome structure in a straight-line wind field. Two turbulence models were studied, including renormalization group (RNG) k-ε turbulence model and large eddy simulation

(LES) model. It was found that the LES model showed better agreement with wind tunnel testing than the RNG k-ε model. Wood et al. (2016) investigated the influence of different subgrid-scale models adopted in LES on the boundary layer separation points on a spherical dome structure in a straight-line wind field. The adopted subgrid-scale models included the Smagorinsky-Lily model (Smagorinsky, 1963), the dynamic Smagorinsky-Lily model (Germano et al., 1991; Lilly, 1992), and the wall-adapting local eddy-viscosity (WALE) model (Nicoud and Ducros, 1999). It was concluded that the location of boundary layer separation was the same for all subgrid-scale models. Fu et al. (2015) applied the LES model in CFD simulations to determine mean pressure coefficients of a spherical dome structure in a straight-line wind field, and the numerical results agreed fairly well with the wind tunnel testing.

Since the selection of a turbulence model affects the reproduction of the flow structure of the wind field around the dome structure and hence the accuracy of wind pressure distribution on the dome surface, the commonly used turbulence models, Reynolds averaged Navier-Stokes (RANS) turbulence models and the LES model, are reviewed here.

RANS models modify the original unsteady Navier-Stokes equations by treating velocity/pressure into the superimposition of averaged and fluctuating quantities. The averaged quantities are solved by RANS equations. The fluctuating quantities, also called Reynolds stresses, are assumed to be related to the turbulent eddy viscosity and the mean velocity gradient. The turbulent eddy viscosity is determined based on additional transport equations. Based on the number of transport equations required, the RANS models can be classified into one-equation RANS turbulence models, two-equation

RANS turbulence models, three-equation RANS turbulence models, and so on. In one-equation RANS turbulence models, only one transport equation is needed to determine the turbulent eddy viscosity. A representative one-equation RANS model is the Spalart-Allmaras model (Spalart and Allmaras, 1994). This model is developed for wall-bounded flows and has been proved to offer good results for airflows with mild separation and recirculation. It is robust and fast to implement, and it is not memory-intensive and easy to converge. In two-equation RANS turbulence models, two transport equations are needed to determine the turbulent eddy viscosity. The representative two-equation models include the standard k-ε model (Launder and Spalding, 1972) and the standard k-ω model (Wilcox, 1998). k represents turbulent kinetic energy. ε and ω are two different forms to represent the dissipation rate of turbulent kinetic energy. The main drawback of the standard k-ε model is that it overestimates k at impinging region when the wind passes the civil structure (Murakami, 1998). To tackle this problem, more advanced k-ε models were developed, e.g., realizable k-ε model (Shih et al., 1995) and RNG k-ε model (Yakhot et al., 1992). The primary drawback of standard k-ω model is its sensitivity to the inlet conditions compared to k-ε models. One of the improved k-ω models is the shear stress transport (SST) k-ω model (Menter, 1994; Menter, 1997; Menter et al., 2003). It overcomes the flaw of the original k-ω model and can predict the boundary layer separation and reattachment better than the standard k-ω model and k-ε model.

Different from RANS models, LES model separates turbulent eddies into large and small scales. The original unsteady Navier-Stokes equations are filtered in the physical space, and the eddies whose scales are smaller than the filter width are filtered out. Thus, the filtered Navier-Stokes equations only resolve the dynamics of the large

eddies. The small eddies are analytically modeled by subgrid-scale models, e.g., the Smagorinsky-Lily model, the dynamic Smagorinsky-Lilly model, and the WALE model. LES is a time-dependent approach, and thus it can generally reproduce main turbulence properties with a higher accuracy compared to statistically steady RANS simulations (Franke et al., 2004; Murakami, 2002; Tominaga and Stathopoulos, 2010). However, this is achieved at a significantly higher cost in memory and CPU time.

In current study, to investigate the influence of turbulence modeling on the wind effects acting on dome structures induced by straight-line winds, three turbulence models are employed, i.e., Spalart-Allmaras model, SST k-ω model and LES model. Spalart-Allmaras and SST k-ω models are selected due to the following three reasons. First, they are able to better predict boundary layer separation and reattachment than other RANS models; Second, they can reach a compromise between accuracy and computational cost; and Third, they have good convergence properties. LES model is selected because it is a time-dependent approach, which is able to provide more detailed information of the wind field than RANS models that only provide statistically steady solution. All CFD simulation results are compared to a wind tunnel testing to evaluate their accuracy on the prediction of wind pressure distribution on the dome surface.

The remainder of the paper is organized as follows. First, the spherical dome structure of interest and the setup of wind tunnel testing are described. Then, wind tunnel testing results are presented in terms of velocity profile and pressure distribution on the dome surface. Third, CFD simulations of the wind field produced in the wind tunnel (when the dome model is not present) are conducted, and the influence of the turbulence modeling on the wind field is discussed. The verification of velocity input and grid

independence study are also discussed in this section. Fourth, CFD simulations of the wind tunnel testing of the dome model are conducted, and the influence of turbulence modeling is investigated in regard to the along-wind velocity and static pressure in the entire wind field and the wind pressure distribution on the dome surface. Finally, conclusions are drawn.

2. DOME GEOMETRY AND EXPERIMENTAL SETUP

Wind tunnel testing of a large-scale dome structure is conducted in the "Wall of Wind (WOW)" facility at Florida International University (FIU). This section introduces the dimensions of the dome model and the testing setup in the WOW.

2.1. DOME DIMENSIONS

The prototype spherical dome selected for this study has a base diameter of 120 m and apex height of 40 m. At a scale of 1:60, a dome model with a base diameter of 2.0 m and apex height of 0.67 m is created, as shown in Figure 3. It is made of a smooth shell with the thickness of 9.0 mm. The blockage rate of this dome model in the wind tunnel is 0.7%, which is the ratio of the projected area of the dome model to the cross-sectional area of the testing section of the WOW facility.

2.2. CONFIGURATION OF THE WOW FACILITY

The WOW facility is a large open circuit wind tunnel, as shown in Figure 4. A 30.5 m × 24.4 m × 10.7 m building (Figure 4(a)) is used to house the WOW facility, of

which the big door is 15.24 m × 9.14 m. Twelve fans, located on the South end, are used to generate winds. The flow conditioning section is 6.10 m wide and 4.27 m high, which is used to generate desired wind velocity profile and turbulence using spires and/or floor roughness elements (Figure 4(c)). A 4.9 m-diameter turning table is located 6.1 m downstream of the end of the flow conditioning section. This turning table allows the investigation of the effect of wind directionality for testing models. The wind-borne debris stopping wall (Figure 4(b)) is 60 m to the North of the center of the turning table. The WOW facility is capable of generating up to Category 5 hurricane winds, together with wind-driven rain and wind-borne debris. The generated wind field is sufficient to engulf a small single-story building, and thus it is able to test small structures at full-scale to failure.

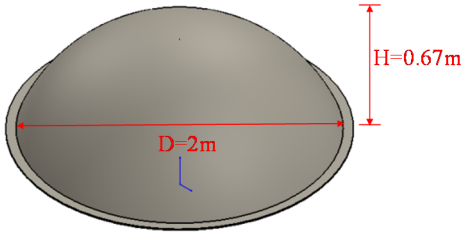

Figure 3. The scaled dome model tested in the WOW facility.

2.3. EXPERIMENTAL SETUP

The dome model is placed at the center of the turning table, which is the origin of the global coordinate system, as shown in Figure 5. The angle (θ) of the turning table is illustrated in Figure 5(a). 0° represents the case when the North side (Figure 5(b)) of the dome model faces the North. Positive angle ($+\theta$) is for the case when the turning table is rotated clockwise. The dome model is tested under two different terrain configurations,

open and suburban terrains, as shown in Figure 6. The open terrain is achieved by spires (Figure 6(a)), while the suburban terrain is achieved by both spires and surface roughness elements (Figure 6(b)).

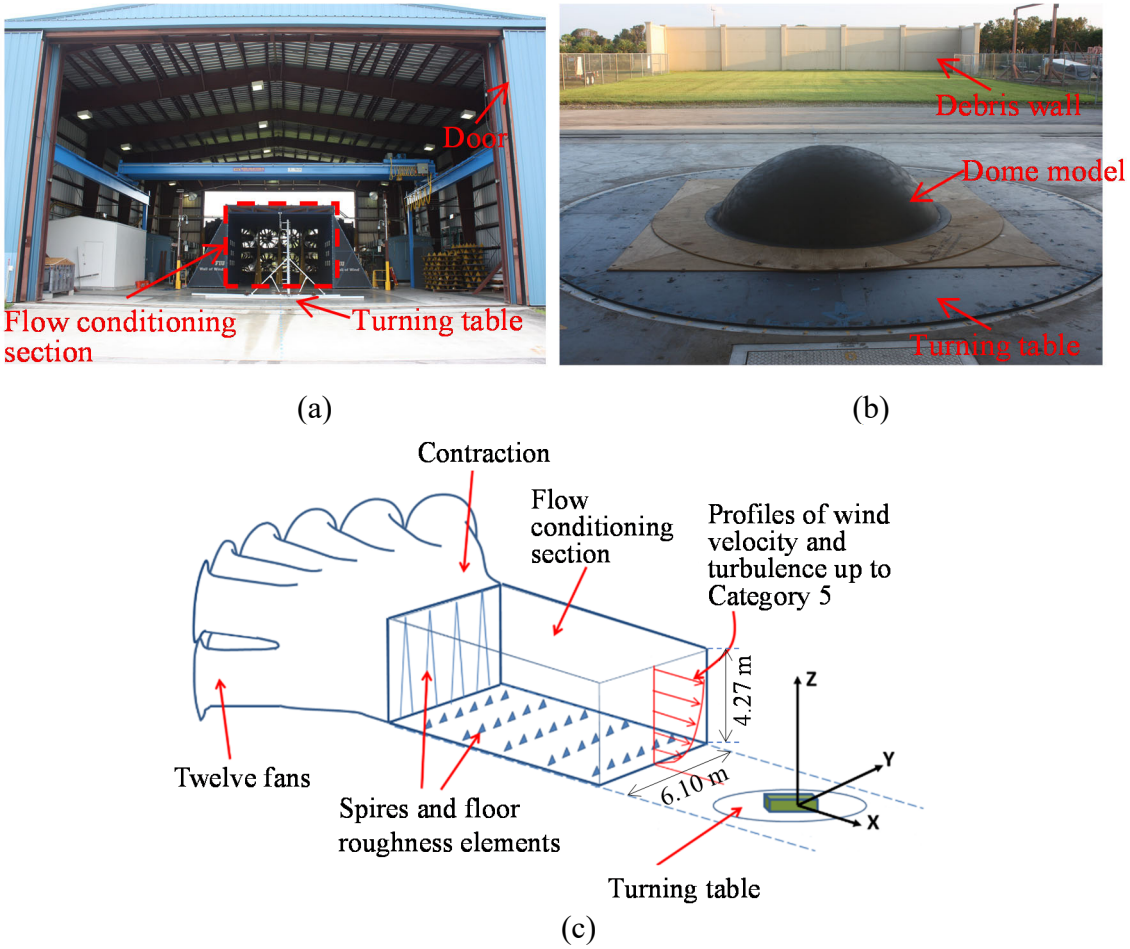

Figure 4. The WOW facility used for experimental investigation: (a) One end of the WOW facility; (b) The other end of the WOW facility; (c) Schematic diagram of the picture in (a).

Wind velocity is measured by TFI Cobra Probes, which are four-hole pressure probes that provide 3-component velocity and local static pressure measurements in real-time. The sampling rate is 2,500 Hz and the sampling duration is 300 s. The velocity

components are calculated based on the local coordinate system of each probe. The coordinate system is shown in Figure 7.

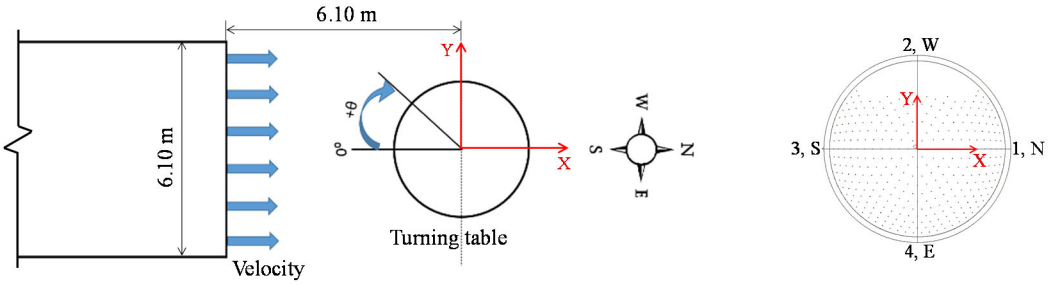

(a) (b)

Figure 5. Top view of the testing section: (a) Angle of the turning table; (b) Orientation of the dome model.

(a) (b)

Figure 6. Experimental setup to achieve two different terrain configurations: (a) Open terrain; (b) Suburban terrain.

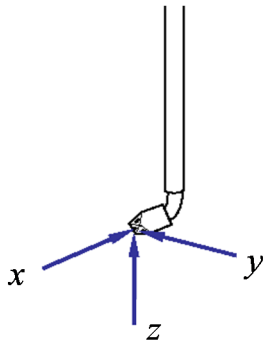

Figure 7. Cobra Probe coordinate system.

In order to get the wind velocity profile along the height, Cobra Probes are placed at the center of the turning table (X=0 and Y=0) at various heights (16.5 cm, 33.3 cm, 66.7 cm, and 133.4 cm) when the dome model is not present, as shown in Figure 8. This measurement is only conducted for open terrain.

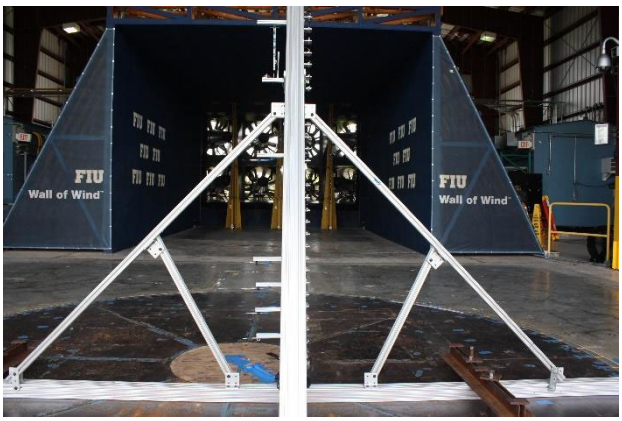

Figure 8. Measurement of wind velocity profile for open terrain.

The wind pressure on the surface of the dome model is measured by pressure taps. The pressure data is acquired by Scanivalve ZOC33 electronic pressure scanners at the sampling rate of 520 Hz for 60 s. Each ZOC33 module incorporates 64 individual piezoresistive pressure sensors with full scale range of ±10 inch H_2O. The pressure taps on the dome model are connected to these sensors using PVC-105-16 tubing. The PVC tubing attached to the tap hole is 0.3 m long, and that attached to the sensor side is 0.6 m long. These two PVC tubing pieces are connected through a piece of steel tubing. In total, 384 pressure taps are placed across the entire surface of the dome model. The distribution of pressure taps on the dome surface is shown in Figure 9. Due to the limitation of the

number of pressure taps, a small area along the positive Y axis is not deployed with pressure taps.

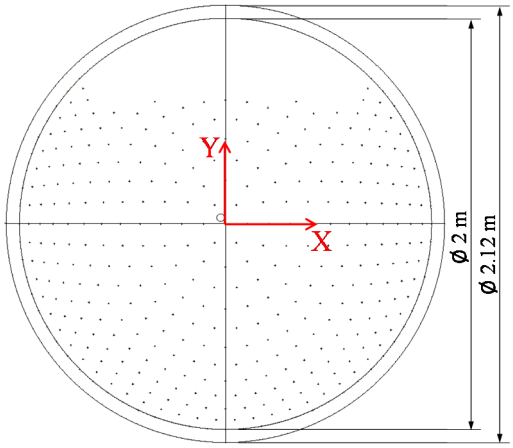

Figure 9. Distribution of pressure taps on the dome surface (black dots represent the locations of pressure taps).

3. TESTING RESULTS AND DISCUSSION

3.1. MEAN VELOCITY PROFILE

The measured wind velocity profiles along height over open terrain are presented in Figure 10. They are time-averaged. In each subfigure of Figure 10, 52%, 74%, and 95% represent that the fans are kept at 52%, 74%, and 95% throttle for 300 s. Time-averaging is conducted on 280 s of each velocity component, eliminating the first and last 10 s to avoid uncertainties. From Figure 10, the along-wind mean velocity increases with the increase of elevation, while the vertical and across-wind mean velocities decrease with the increase of elevation. It is noted that the same across-wind mean velocity is observed at the elevation of 1.33 m for the three cases (Figure 10(b)).

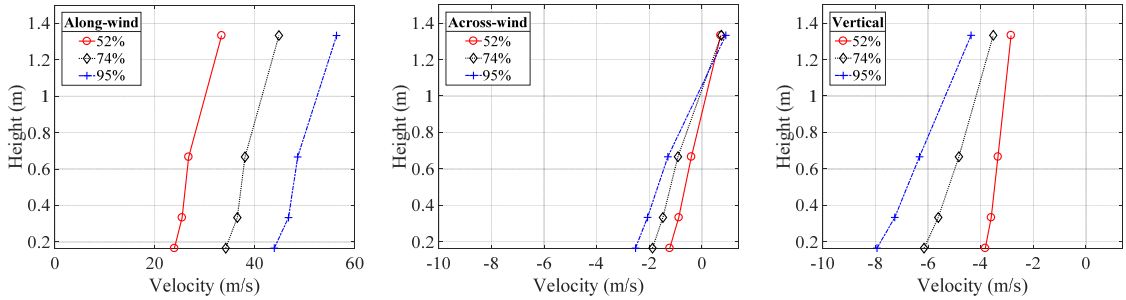

(a) (b) (c)

Figure 10. The obtained mean velocity profile for open terrain: (a) Along-wind; (b) Across-wind; (c) Vertical.

The power spectral density (PSD) of the time history of the along-wind velocity at 0.67 m, which is the same as the elevation of the dome apex, for 95% throttle over open terrain is presented in Figure 11. The obtained PSD from wind tunnel testing matches the ESDU spectrum in the high frequency range, which is acceptable since the high frequency range is important in the design of civil structures where resonance is possible.

3.2. TURBULENCE INTENSITY

Turbulence intensity (TI) is used to quantify turbulence of the airflow, which is obtained based on the time histories of wind velocity from the wind tunnel testing. TI is defined as

$$I = \frac{u'}{U}$$

$$u' = \sqrt{\frac{1}{3}\left(u_X'^{\,2} + u_Y'^{\,2} + u_Z'^{\,2}\right)} \tag{1}$$

$$U = \sqrt{U_X^2 + U_Y^2 + U_Z^2}$$

where u' is the root-mean-square of the fluctuating components of the measured velocity, and U is the mean resultant velocity. Subscripts X, Y, and Z represent three velocity components. According to Equation (1), TI for open terrain under 95% throttle is shown in Figure 12. They are all close to 10% at the four different heights.

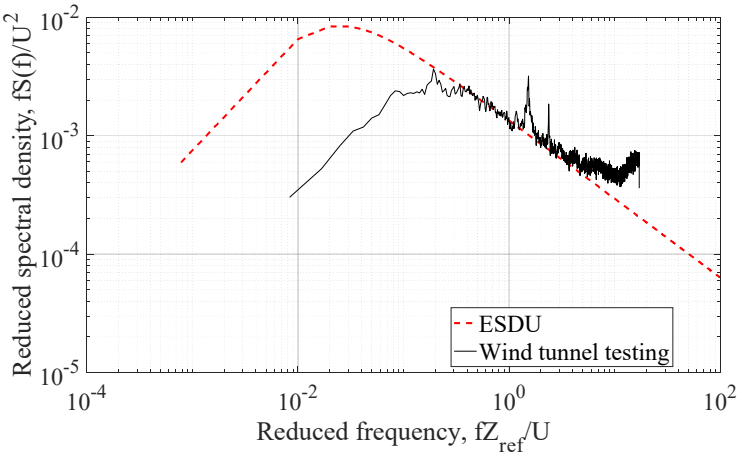

Figure 11. Power spectral density of the time history of along-wind velocity for 95% throttle at 0.67 m (dome apex) over open terrain.

3.3. CONTOUR PLOTS OF MEAN PRESSURE COEFFICIENT

All pressure data are non-dimensionalized into pressure coefficients based on the reference dynamic pressure at the dome apex as

$$C_{P_i} = \frac{P_i - P_\infty}{\frac{1}{2}\rho V^2} \tag{2}$$

where $P_i - P_\infty$ represents the pressure difference between local and reference pressure P_∞, which is directly obtained via the Scanivalve measurements. P_∞ is atmospheric pressure. ρ is the density of air (1.16 kg/m^3), and it is determined based on the air temperature (30 °C), humidity (65%), and atmospheric pressure (101 kPa) at the time of

the test. V is the reference mean velocity that is taken at the elevation of 0.67 m for 95% throttle over open terrain, which is 49 m/s.

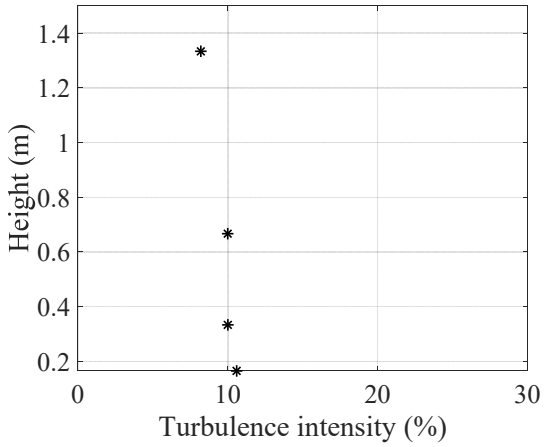

Figure 12. TI along height under 95% throttle for open terrain.

3.3.1. Open Terrain. Figure 13 presents the contour plots of mean pressure coefficient over open terrain at 52%, 74%, and 95% throttle, which are obtained from the averaging of 40-s-record of pressure data. In each case, the fans were started from 0% throttle, then ramped to the specified throttle, and were kept constant thereafter for 60 s. During the last 60 s of data, the middle 40 s (10 s - 50 s) is used to do the time averaging in order to eliminate the uncertainties from the first and last 10 s. Since pressure taps did not cover the entire surface of the dome model, pressure coefficient in the unmeasured small area along the positive Y axis (see Figure 9) is mapped from the corresponding area along the negative Y axis. Figure 13 shows that generally the wind pressure distributions are similar when the dome model is under the three different fan throttles, that is, positive pressure on the windward side, negative (suction) pressure on the leeward side, and maximum negative pressure around the dome apex. However, the pressure distribution on

the leeward side is slightly different. In general, the magnitudes of positive and negative pressure coefficients increase with the increase of fan throttle. Comparison of Figures 13(a) and 13(c) indicates that the magnitudes of positive and negative pressure coefficients increase four times when the fan throttle is doubled, which is consistent with the relationship between the upstream velocity and surface pressure based on the equation for calculating the surface pressure.

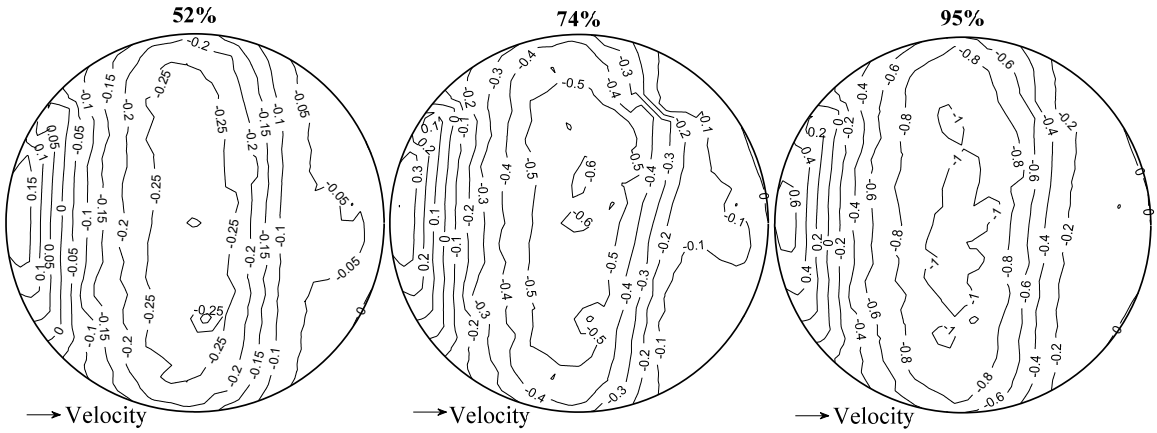

Figure 13. Pressure coefficients over open terrain: (a) 52% throttle; (b) 74% throttle; (c) 95% throttle.

3.3.2. Suburban Terrain. Contour plots of mean pressure coefficients over suburban terrain at 52%, 74%, and 95% throttle are presented in Figure 14. The testing procedure and averaging method for suburban terrain are the same as those for open terrain. Comparison between Figures 13 and 14 indicates that the wind pressure distribution over the two different terrains follows a similar pattern, while the magnitudes of both positive and negative pressure coefficients are lower over the suburban terrain.

This is expected because wind velocity over suburban terrain is lower due to higher surface roughness over suburban terrain.

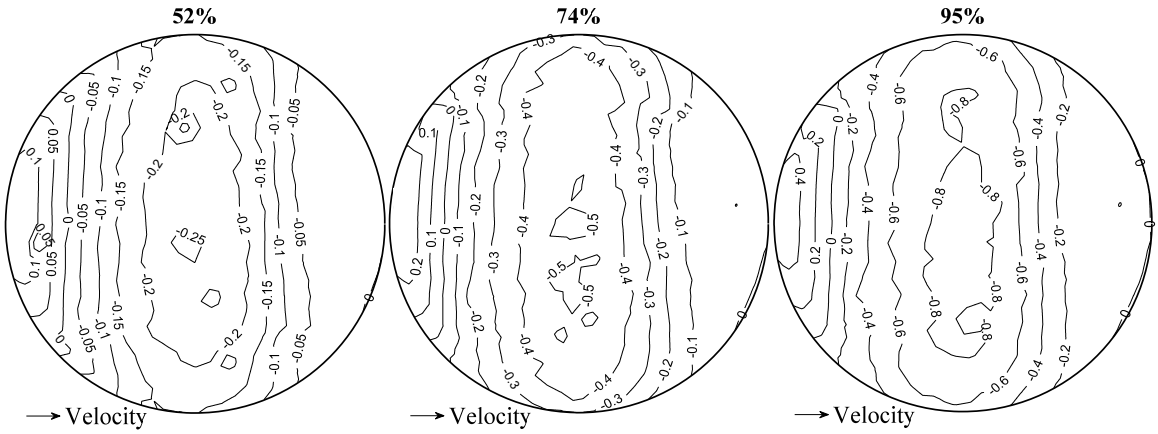

(a) (b) (c)

Figure 14. Pressure coefficients over suburban terrain: (a) 52% throttle; (b) 74% throttle; (c) 95% throttle.

3.4. FORCE AND MOMENT COEFFICIENT

By the integration of the surface pressures, the overall forces and moments acting on the dome model can be determined. The obtained forces and moments over both open and suburban terrains at all fan throttles (52%, 74%, and 95%) are listed in Table 1. Suction force (F_Z) is the most significant among all six forces and moments. The drag force F_Y, the overturning moment M_X, and the rotational moment M_Z are extremely small that can be neglected, which is due to the symmetry of the dome model and the symmetric distribution of static pressure on the dome surface about X axis. For F_X, F_Z, and M_Y, they increase with the increase of the fan throttle. Because of the significance of the suction force F_Z, it serves as one parameter for the match between CFD simulations and the wind tunnel testing.

Table 1. Force and moment.

	Open terrain			Suburban terrain		
	52%	74%	95%	52%	74%	95%
F_X (N)	45.9	74.1	136.3	59.7	76.4	127.4
F_Y (N)	-2.6	16.5	1.1	-9.6	-19.6	-23.5
F_Z (N)	597.2	1188.4	2151.8	479.2	1056.0	1764.8
M_X (N·m)	-1.1	6.9	0.4	-4.0	-8.2	-9.8
M_Y (N·m)	-19.1	-31.0	-57.0	-24.9	-31.9	-53.2
M_Z (N·m)	-0.02	-0.03	-0.08	-0.03	-0.05	-0.08

All forces and moments are normalized by the dynamic pressure, which are calculated using Equation (3). The obtained force and moment coefficients are listed in Table 2. Suction force coefficient is the most significant. While the difference between the suction force is large (e.g., around 72% difference between 52% and 95% throttle), the difference between the suction force coefficient is pretty small (e.g., around 9% difference between 52% and 95% throttle).

$$C_{F_X} = \frac{F_X}{\frac{1}{2}\rho V^2 A}, C_{M_X} = \frac{M_X}{\frac{1}{2}\rho V^2 A H}$$

$$C_{F_Y} = \frac{F_Y}{\frac{1}{2}\rho V^2 A}, C_{M_Y} = \frac{M_Y}{\frac{1}{2}\rho V^2 A H} \quad (3)$$

$$C_{F_Z} = \frac{F_Z}{\frac{1}{2}\rho V^2 A}, C_{M_Z} = \frac{M_Z}{\frac{1}{2}\rho V^2 A H}$$

where F_X, F_Y, and F_Z, are the forces applied on the dome model; M_X, M_Y, and M_Z are the moments applied on the dome model; ρ is the same as in Equation (2), 1.16 $\mathrm{kg/m^3}$; A is the projected area of the dome model on a plane parallel to the cross-section of the wind tunnel (0.97 $\mathrm{m^2}$); H is the height of the dome apex (0.67 m); V is the reference mean

velocity (27 m/s under 52% throttle, 38 m/s under 74% throttle, and 49 m/s under 95% throttle, which are all from the open terrain).

Table 2. Force coefficient and moment coefficient.

	Open terrain			Suburban terrain		
	52%	74%	95%	52%	74%	95%
C_{F_X}	0.11	0.09	0.10	0.15	0.09	0.09
C_{F_Y}	-0.01	0.02	0.00	-0.02	-0.02	-0.02
C_{F_Z}	1.46	1.46	1.59	1.17	1.30	1.31
C_{M_X}	0.00	0.01	0.00	-0.01	-0.02	-0.01
C_{M_Y}	-0.07	-0.06	-0.06	-0.09	-0.06	-0.06
C_{M_Z}	0.00	0.00	0.00	0.00	0.00	0.00

3.5. REYNOLDS NUMBER

The Reynolds number (Re) is the ratio of inertial forces to viscous forces, expressed as:

$$Re = \frac{\rho V H}{\mu} \tag{4}$$

where ρ is the same as in Equation (2), $1.16\ \mathrm{kg/m^3}$; V is the reference mean velocity (27 m/s under 52% throttle, 38 m/s under 74% throttle, and 49 m/s under 95% throttle, which are all measured over open terrain at the height of 0.67 m that is the same height as the dome apex); H is the same as in Equation (3), 0.67 m; μ is dynamic viscosity of air at the air temperature of 30 °C ($1.86 \times 10^{-5}\ \mathrm{N{\cdot}s/m^2}$).

According to Equation (4), the Reynolds numbers for 52%, 74%, and 95% throttle over open terrain (when the dome model is not present) are determined as 1.13×10^6, 1.59×10^6, and 2.03×10^6, respectively.

4. NUMERICAL SIMULATION OF WIND FIELD PRODUCED IN WOW AND DISCUSSION OF RESULTS

4.1. COMPUTATIONAL DOMAIN

To simulate the straight-line wind field, a rectangular computational domain is applied, as shown in Figure 15. It consists of two parts, Part A and Part B. Part A is from the end of the flow conditioning section to the WOW door, and Part B is from the WOW door to the debris wall. The total length of the computational domain is 66.10 m. The cross section of the computational domain is 15.24 m wide and 9.14 m high, which has the same dimensions as the WOW door. On the left boundary surface of Part A, the area associated with the flow conditioning section is defined as the velocity inlet, with the width and height of 6.10 m and 4.27 m, respectively. The rest of the left boundary surface of part A, excluding the velocity inlet, is defined as no-slip wall, so are the front, back, top, and bottom boundary surfaces. For Part B, the front, top, and back boundary surfaces are defined as pressure outlet, as these three sides are open to air, and the bottom surface and the debris wall are defined as no-slip wall. All boundary surfaces that are defined as no-slip wall are shaded in Figure 15 except the bottom surface. The origin of the Cartesian coordinate system is located at the center of the turning table, which is 6.1 m away from the velocity inlet.

4.2. DETERMINATION OF VELOCITY INPUT

The velocity input at the velocity inlet is obtained from the mean velocity data presented in Figure 10, which was measured at the center of the turning table in the wind field when no dome model was present. The velocity was measured over open terrain at

95% throttle at four elevations. Only the along-wind velocity is considered for velocity input, since the other two velocity components are relatively small and thus can be neglected. To obtain the velocity input, the regression technique is applied to the mean velocity data at the four elevations. The regression equation is based on the power law (Simiu and Scanlan, 1986) and expressed as

$$\bar{V}(z) = \bar{V}(z_{ref}) \times (\frac{z}{z_{ref}})^{1/\alpha} \quad (5)$$

where z is the elevation above the ground; z_{ref} denotes the reference height, 0.167 m in this wind tunnel testing, which is associated with 10 m in full-scale; $\bar{V}(z_{ref})$ denotes the mean velocity at the reference height z_{ref}, 43.95 m/s for the along-wind velocity at 0.167 m; α is a function of surface roughness, which will be determined using the regression technique.

The obtained regression equation of the mean along-wind velocity profile along height (95% throttle over open terrain) is shown in Equation (6) with α determined as 9.41.

$$V_{along-wind} = 43.95 \times (\frac{z}{0.167})^{1/9.41} \quad (6)$$

The comparison between the power law regression equation and the mean along-wind velocity data from the wind tunnel testing is presented in Figure 16. It is found that the regression equation is in good agreement with the velocity data from the wind tunnel testing. In this study, it is assumed that the mean velocity profile measured at the end of the flow conditioning section (Figure 4) is the same as that measured at the center of the turning table. Therefore, Equation (6) is directly used as the velocity input at the velocity inlet in the following CFD simulations.

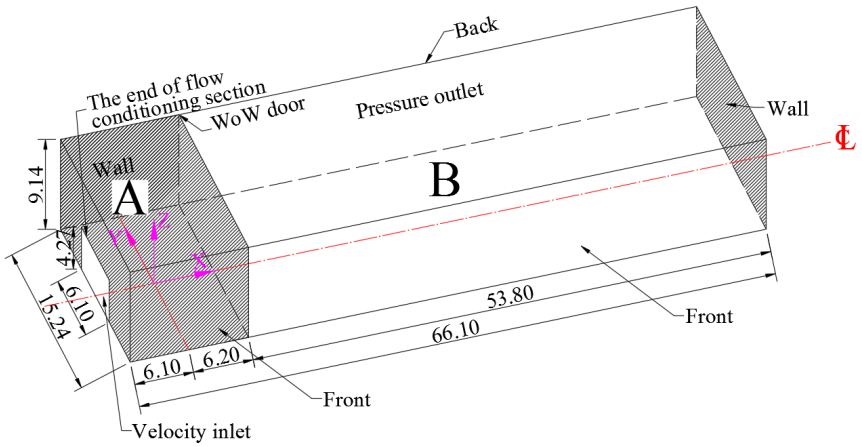

Figure 15. Computational domain applied to simulate the wind field produced in WOW (unit: m).

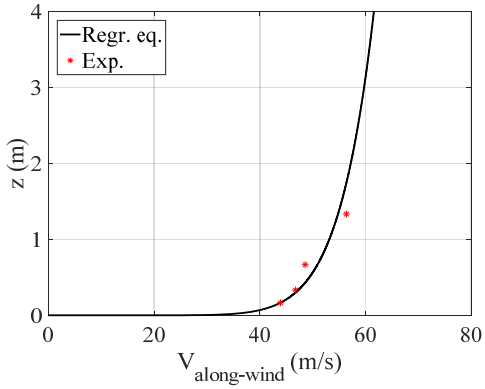

Figure 16. Comparison of the regression equation ("Regr. eq.") and the mean velocity profile obtained from the wind tunnel testing ("Exp.").

4.3. TURBULENCE MODELING AND OTHER CFD SIMULATION SETUP

Three different turbulence models (Spalart-Allmaras model, SST *k*-ω model and LES model) are employed sequentially. The transport equations for Spalart-Allmaras and SST *k*-ω models are listed in Table 3. The model constants used in the CFD simulations are also listed in Table 3. The filtered Navier-Stokes equations employed by the LES

model is presented in Table 3, and Smagorinsky-Lilly model with constant $c_s = 0.1$ is selected as the subgrid-scale model.

Table 3. Turbulence model equations.

Spalart-Allmaras model	Transport equation: $\frac{\partial}{\partial t}(\rho\tilde{\nu}) + \frac{\partial}{\partial x_i}(\rho\tilde{\nu}u_i) = G_\nu + \frac{1}{\sigma_{\tilde{\nu}}}\left\{\frac{\partial}{\partial x_j}\left[(\mu + \rho\tilde{\nu})\frac{\partial\tilde{\nu}}{\partial x_j}\right] + C_{b2}\rho\left(\frac{\partial\tilde{\nu}}{\partial x_j}\right)^2\right\} - Y_V + S_{\tilde{\nu}}$ where $\tilde{\nu}$ is the modified turbulent viscosity; G_ν is the production of turbulent viscosity, and Y_V is the destruction of turbulent viscosity that occurs in the near-wall region due to wall blocking and viscous damping. $\sigma_{\tilde{\nu}}$ and C_{b2} are the constants and ν is the molecular kinematic viscosity. $S_{\tilde{\nu}}$ is a user-defined source term. Model constants: $C_{b1} = 0.1355$, $C_{b2} = 0.622$, $C_{v1} = 7.1$, $C_{w1} = \frac{C_{b1}}{\kappa^2} + \frac{1+C_{b2}}{\sigma_{\tilde{\nu}}}$, $C_{w2} = 0.3$, $C_{w3} = 2$, $\sigma_{\tilde{\nu}} = 0.667$, $\kappa = 0.4187$.
SST k-ω model	Transport equation for k: $\frac{\partial}{\partial t}(\rho k) + \frac{\partial}{\partial x_i}(\rho k u_i) = \frac{\partial}{\partial x_j}\left(\Gamma_k\frac{\partial k}{\partial x_j}\right) + G_k - Y_k + S_k$ Transport equation for ω: $\frac{\partial}{\partial t}(\rho\omega) + \frac{\partial}{\partial x_i}(\rho\omega u_i) = \frac{\partial}{\partial x_j}\left(\Gamma_\omega\frac{\partial\omega}{\partial x_j}\right) + G_\omega - Y_\omega + D_\omega + S_\omega$ where G_k represents the production of k. G_ω represents the generation of ω. Γ_k and Γ_ω are the effective diffusivity of k and ω, respectively. Y_k and Y_ω represent the dissipation of k and ω due to turbulence. D_ω is the cross-diffusion term. S_k and S_ω are user-defined source terms. Model constants: $\alpha^*_\infty = 1$, $\alpha_\infty = 0.52$, $\beta^*_\infty = 0.09$, $a_1 = 0.31$, $\beta_{i,1} = 0.075$, $\beta_{i,2} = 0.0828$, $\sigma_{k,1} = 1.176$, $\sigma_{k,2} = 1.0$, $\sigma_{\omega,1} = 2.0$, $\sigma_{\omega,2} = 1.168$.
LES model	Filtered Navier-Stokes equation: $\frac{\partial\overline{U}_i}{\partial t} + \overline{U}_j\frac{\partial\overline{U}_i}{\partial x_j} + \frac{\partial\tau^r_{ij}}{\partial x_j} = -\frac{1}{\rho}\frac{\partial\bar{p}}{\partial x_i} + \nu\nabla^2\overline{U}_i$ where τ^r_{ij} is the anisotropic residual stress tensor, $\bar{p}$ is the modified filtered pressure, ν is kinematic viscosity, and ρ is the fluid density. Subgrid-scale model: Dynamic Smagorinsky-Lilly model with constant $c_s = 0.1$.

For each turbulence model, the segregated implicit solver, semi-implicit method for pressure linked equation-consistent (SIMPLEC) pressure velocity coupling, second order discretization for pressure, and bounded second order implicit for transient formulation are used. Second order upwind discretization scheme for momentum equations is used for Spalart-Allmaras and SST k-ω model, and bounded central difference discretization scheme for momentum equations is used for the LES model. The CFD simulation is run for 5 s with the time step of 0.0001 s. Such a small time step is used to accurately capture sufficient information from the simulation. The convergence criterion for the residual within one time step is defined as "Error between two time steps < 0.001".

4.4. GRID INDEPENDENCE STUDY

To investigate the influence of meshing size on the generated wind field and to determine the optimal number of cells, three cases with different meshing sizes are simulated, as shown in Table 4. For each case, structured mesh is applied to the entire computational domain (Figure 15).

The inflation grid technique is applied to the ground surface in order to capture the velocity gradients in the lowest layers near the ground, with the thickness of the first layer of 0.001 m, the growth rate of 1.19, and the total height of 1.2 m. Figure 17 presents the details of Mesh 1. Part A and Part B are all divided into four zones. The dimensions of Zone 1 are the same as those of the velocity inlet. The grid arrangement of Mesh 2 and Mesh 3 is similar to that of Mesh 1. The total number of generated cells is 0.85 million, 0.43 million, and 0.17 million for Mesh1, Mesh 2, and Mesh 3, respectively.

Table 4. Meshing strategies of the wind field without the dome model present.

	Mesh 1	Mesh 2	Mesh 3
Grid size of Part A (m×m×m)	0.2×0.2×0.2	0.3×0.3×0.3	0.4×0.4×0.4
Grid size of Part B (m×m×m)	0.2×0.2×0.5	0.3×0.3×0.6	0.4×0.4×0.8
Total No. of Cells (million)	0.85	0.43	0.17

Note: a×b×c represents width×height×length.

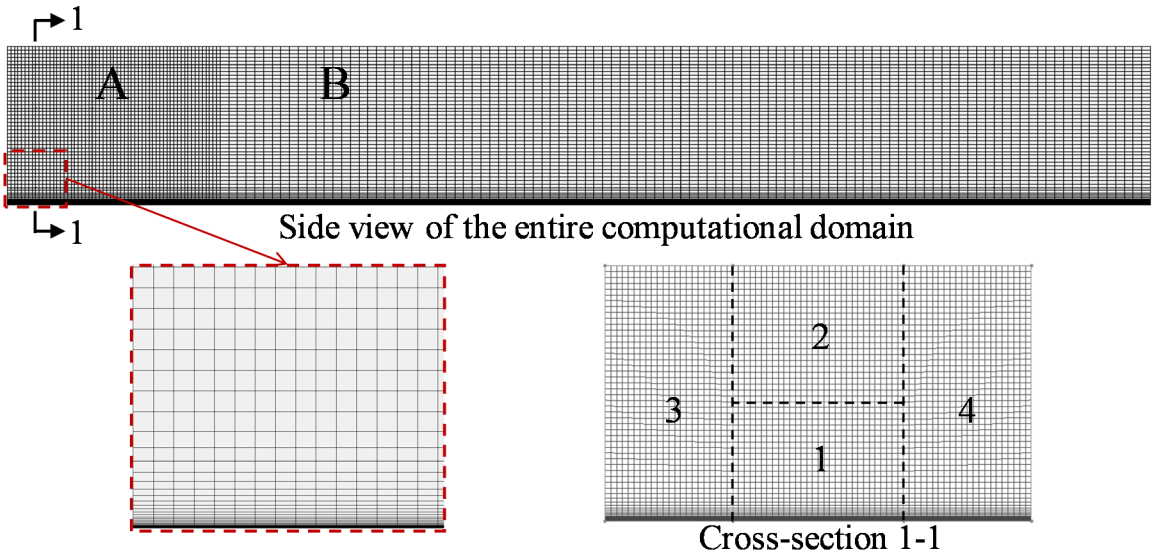

Figure 17. Structured mesh of the computational domain without the dome model present (Mesh 1).

For each case, the mean velocity profile is extracted at the center of the turning table, that is, the origin of the global coordinate system. The time averaging is based on the velocity data from 4 s to 5 s at the time interval of 0.0001 s. In all the three simulated cases, only the turbulence model of Spalart-Allmaras is considered for simplicity. Figure 18 presents the comparison of the mean velocity profiles among the three cases with different meshes. No large difference is found between these three cases, and thus the

independence of numerical results can be preserved. To achieve computational efficiency, Mesh 3 is employed to investigate the influence of turbulence modeling on the mean along-wind velocity profile.

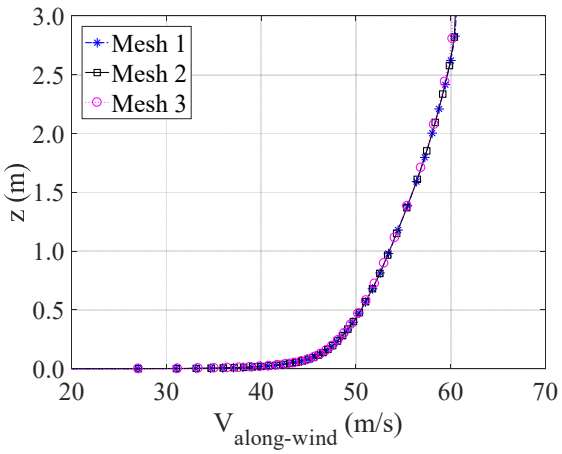

Figure 18. Mean along-wind velocity profile among the three cases with different meshes.

4.5. INFLUENCE OF DIFFERENT TURBULENCE MODELS

To investigate the influence of turbulence modeling on the simulated wind field, three cases with different turbulence models (Spalart-Allmaras, SST k-ω and LES models) are simulated. Figure 19 presents the comparison of the mean velocity profile extracted from the three simulated cases. Above 1.4 m, very minor differences are found among the three simulated cases, while larger differences are observed below 1.4 m. To be specific, the mean velocities with the Spalart-Allmaras and SST k-ω models are larger than that with the LES model at the same height. This indicates that the turbulence modeling affects the airflow characteristics in the near-wall regions more significantly than at higher elevations.

For comparison, the mean velocity profile obtained from the wind tunnel testing is also presented in Figure 19. The error of the velocity results based on the LES model is the smallest. The maximum error is associated with the SST *k*-ω model and less than 9%. Therefore, no matter which turbulence model is used, the numerically obtained mean velocity profiles are in general agreement with the wind tunnel testing. In addition, the Reynolds numbers in the three simulated cases (at the elevation of 0.67 m) are 2.16×10^6, 2.12×10^6, and 2.13×10^6 for Spalart-Allmaras, SST *k*-ω, and LES models, respectively, which are in the error of 6.4%, 4.4%, and 4.9% with the wind tunnel testing (2.03×10^6). Therefore, with respect to the mean velocity profile and the Reynolds number, the CFD simulation results match the wind tunnel testing very well. By comparing the regression equation (Equation (6), which is taken as the velocity input at the velocity inlet) with the three numerically obtained velocity profiles in Figure 19, the aforementioned assumption is verified that the velocity profile measured at the end of the flow conditioning section is very close to that measured at the center of the turning table.

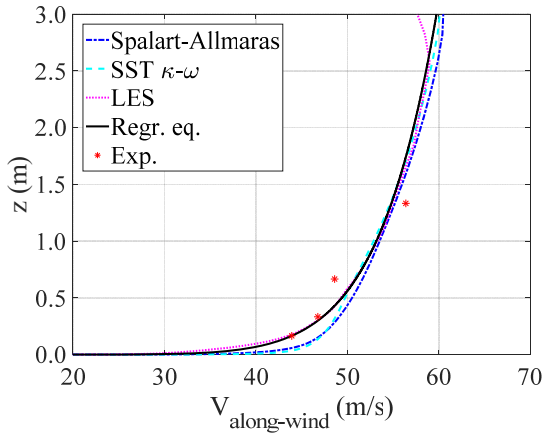

Figure 19. Mean along-wind velocity profile among the three cases with different turbulence models, regression equation ("Regr. eq."), and the wind tunnel testing data ("Exp.").

5. NUMERICAL SIMULATION OF WIND TUNNEL TESTING OF THE DOME STRUCTURE AND DISCUSSION OF RESULTS

A dome model is placed in the computational domain, as shown in Figure 20, to determine the wind effects acting on the dome model. The dome model is placed at the center of the turning table, which is 6.1 m away from the velocity inlet and 6.2 m away from the WOW door. To investigate the influence of turbulence modeling on simulation results, three cases with different turbulence models (Spalart-Allmaras model, SST *k*-*ω*, and LES models) are simulated.

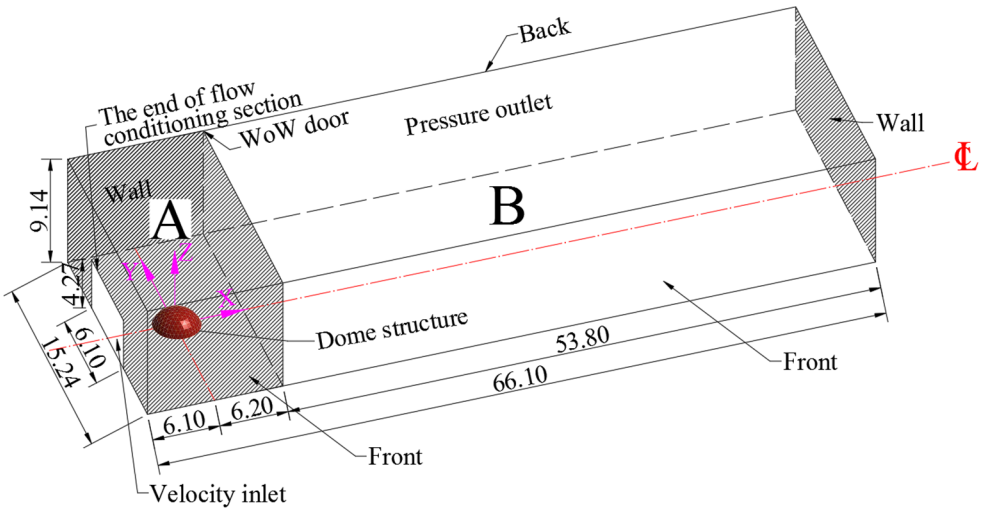

Figure 20. Computational domain to simulate the wind tunnel testing of the dome model in WOW (unit: m).

5.1. GRID INDEPENDENCE STUDY

To investigate the grid sensitivity on the simulation results, three cases with different meshing sizes are simulated. For all the three simulated cases, the turbulence is only modeled by the Spalart-Allmaras model for simplicity. The applied meshing sizes

are the same as the ones listed in Table 4 for the computational domain except zone 1 of Part A. Because of the presence of the dome model, unstructured mesh is applied to Zone 1 of Part A. For Zone 1 of Part A, the global sizes of the cells are 0.2 m, 0.3 m, and 0.4 m for Mesh 1, Mesh 2, and Mesh 3, respectively. The meshing sizes of the dome surface are 0.02 m, 0.03 m, and 0.04 m for Mesh 1, Mesh 2, and Mesh 3, respectively. Besides the ground surface, the inflation grid technique is applied to the area around the dome surface. The total numbers of the generated cells are 2.2 million, 1.4 million, and 0.51 million for these three cases, respectively. Figure 21 presents the grid arrangement of Mesh 1. Similar grid arrangement is applied to Mesh 2 and Mesh 3.

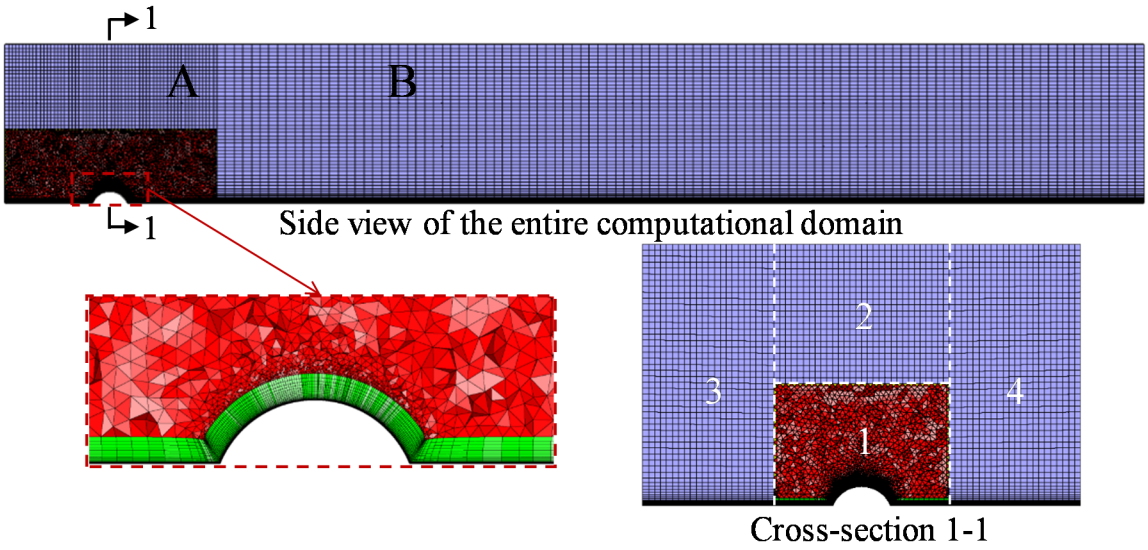

Figure 21. Grid arrangement of the computational domain with the dome model present (Mesh 1).

The distribution of the mean pressure coefficients on the dome surface and the total suction force F_Z are extracted. It is noted that all other moments and forces acting on the entire dome structure (e.g., the drag force F_Y and the rotational moment M_Z) are so

small that they are negligible. Equation (2) is used to determine pressure coefficients, with the reference velocity for each case extracted from its corresponding CFD simulation results at the elevation of 0.67 m. Figure 22 presents the distribution of the mean pressure coefficient on the dome surface for the three cases. No distinct difference is found. The suction forces F_Z are 2209 N, 2205 N, and 2195 N for the three cases associated with Mesh 1, Mesh 2, and Mesh 3, respectively. The maximum error of F_Z among these three cases is less than 1%. Therefore, the numerical results are independent of the meshing size. Considering the computational efficiency, Mesh 3 is used for further analyses. The following CFD simulations are all based on Mesh 3 unless otherwise stated.

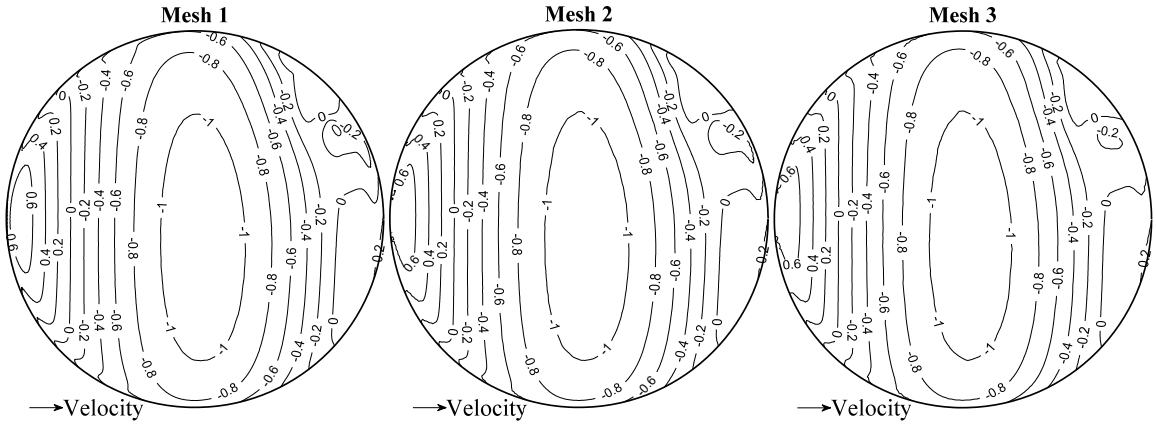

(a) (b) (c)

Figure 22. Pressure coefficients on the dome surface over open terrain at 95% throttle: (a) Mesh 1; (b) Mesh 2; (c) Mesh 3.

5.2. ALONG-WIND VELOCITY IN THE WIND FIELD

For each case, the contour plot of the along-wind velocity on the XZ plane where Y=0 in the entire wind field is presented in Figure 23. The results show that the general

trend of velocity contour is similar when the Spalart-Allmaras and SST k-ω models are used. However, the trend of the velocity contour is significantly different when the LES model is used. The numerically simulated wind field associated with the LES model tends to exhibit more turbulent characteristics. The difference is consistent with the inherent characteristics of the RANS and LES models. To be more specific, the RANS models provide the ensemble-averaged flow condition while the LES model provides detailed, turbulent flow condition.

The zoom-in figures of the velocity contour around the dome model are also presented in Figure 23. It reveals that the airflow on the windward side split at the stagnation point, as indicated by the black dot in each Zoom-in figure of Figure 23. Below the stagnation point, at the corner in front of the dome model, negative velocities appear, indicating the reversal of the flow. Above the stagnation point, the airflow accelerates over and surrounding the dome model due to the convergence of streamlines, which is caused by the blockage of the dome model. On the leeward side, the airflow decelerates, forming the boundary layer separation, and a wake region is present behind the dome model.

5.3. STATIC PRESSURE IN THE WIND FIELD

For each case, the distribution of the static pressure on the XZ plane where Y=0 in the entire wind field is presented in Figure 24. In general, the variation of the static pressure in the wind field is greater when the LES model is used, indicating that the corresponding wind field is more turbulent. This is consistent with the nature of the LES model, since it is a time-dependent approach.

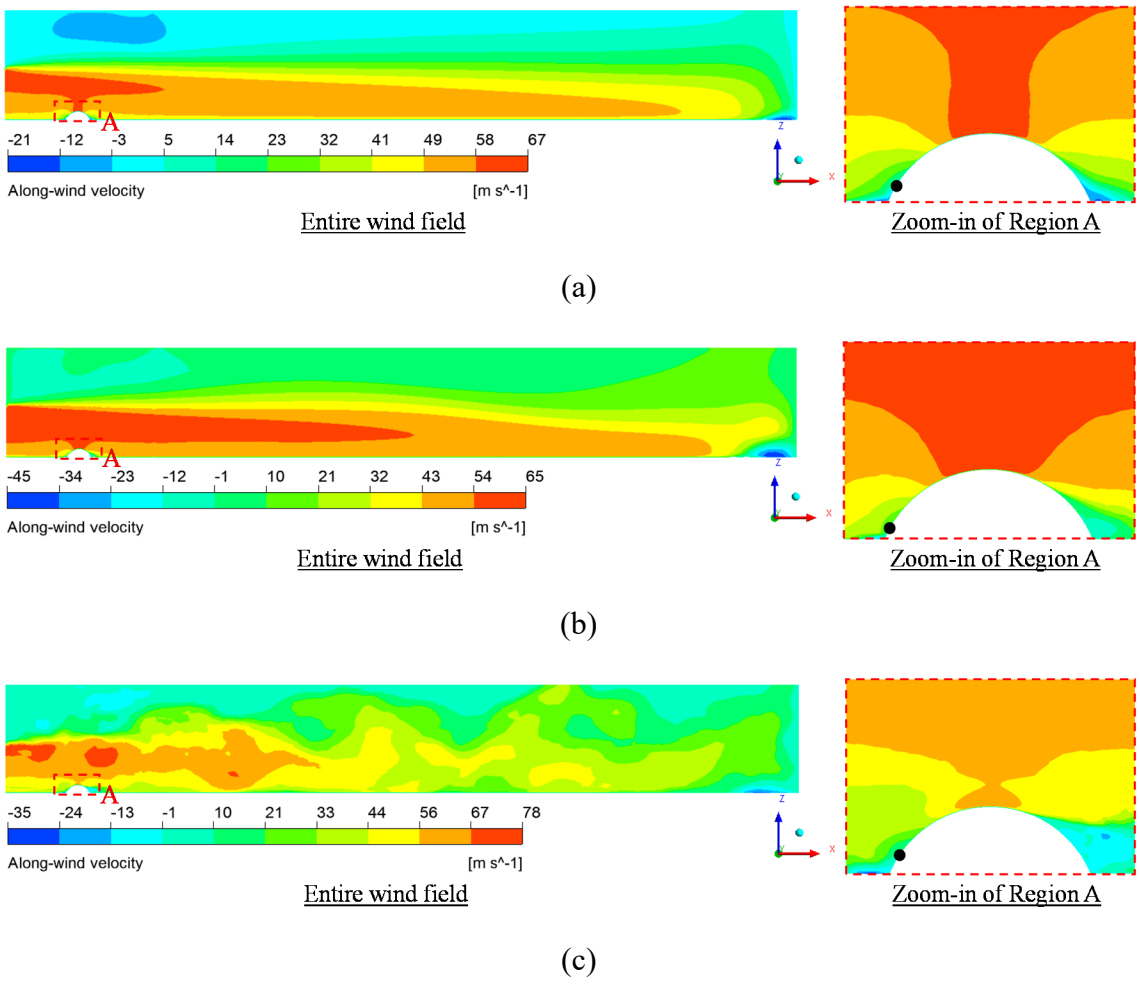

Figure 23. Contour plot of the along-wind velocity in the wind field on the XZ plane where Y=0: (a) Spalart-Allmaras; (b) SST k-ω; (c) LES.

The zoom-in figures of the static pressure distribution around the dome model are also presented in Figure 24. On the windward side of the dome model, positive pressure is observed in the wind field. This is due to the decrease in velocity, which is caused by the divergence of streamline. Around the dome apex and on the top of the dome model, negative pressure is observed in the wind field. This is due to the increase in velocity, which is caused by the convergence of streamline. All the above is based on mass continuity and Bernoulli theorems. On the leeward side of the dome model, negative

pressure is observed in the wind field. This is due to the boundary layer separation on the leeward side of the dome, i.e., less air on the leeward side leads to negative pressure.

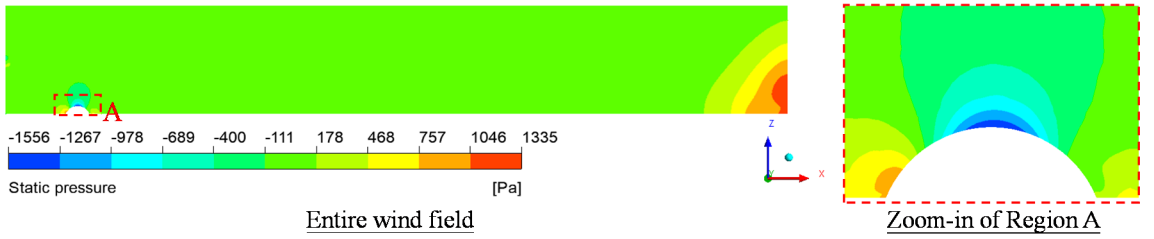

(a)

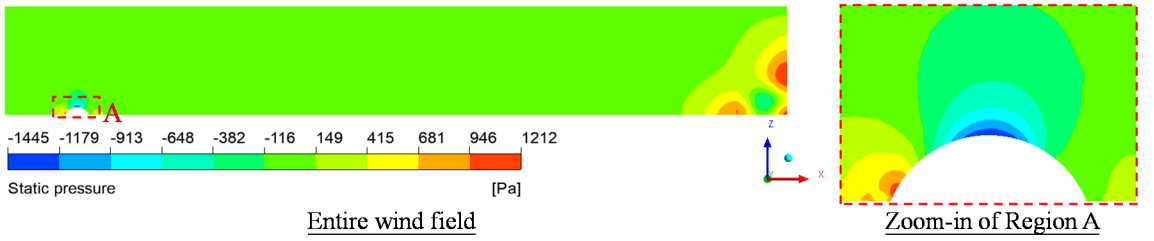

(b)

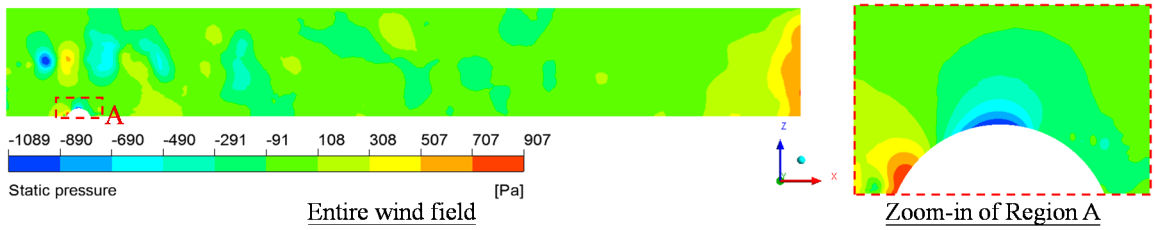

(c)

Figure 24. Contour plot of static pressure in the wind field on XZ plane where Y=0: (a) Spalart-Allmaras; (b) SST *k*-*ω*; (c) LES.

5.4. WIND PRESSURE DISTRIBUTION ON THE DOME SURFACE

Figure 25 presents the mean pressure distribution on the dome surface for all the three simulated cases associated with different turbulence models. Figure 25(a) is associated with the Spalart-Allmaras model, which is exactly the same as Figure 22(c)

and duplicated here for convenience. For comparison, the mean pressure distribution obtained from the wind tunnel testing is presented in Figure 25(d), which is exactly the same as Figure 13(c) and duplicated here for convenience. From Figure 25, although the simulation based on all the three turbulence models follow a similar trend for the wind pressure distribution, the pressure distribution based on the Spalart-Allmaras model (Figure 25(a)) is in the best agreement with the wind tunnel testing in terms of the pressure distribution on the dome surface and F_Z.

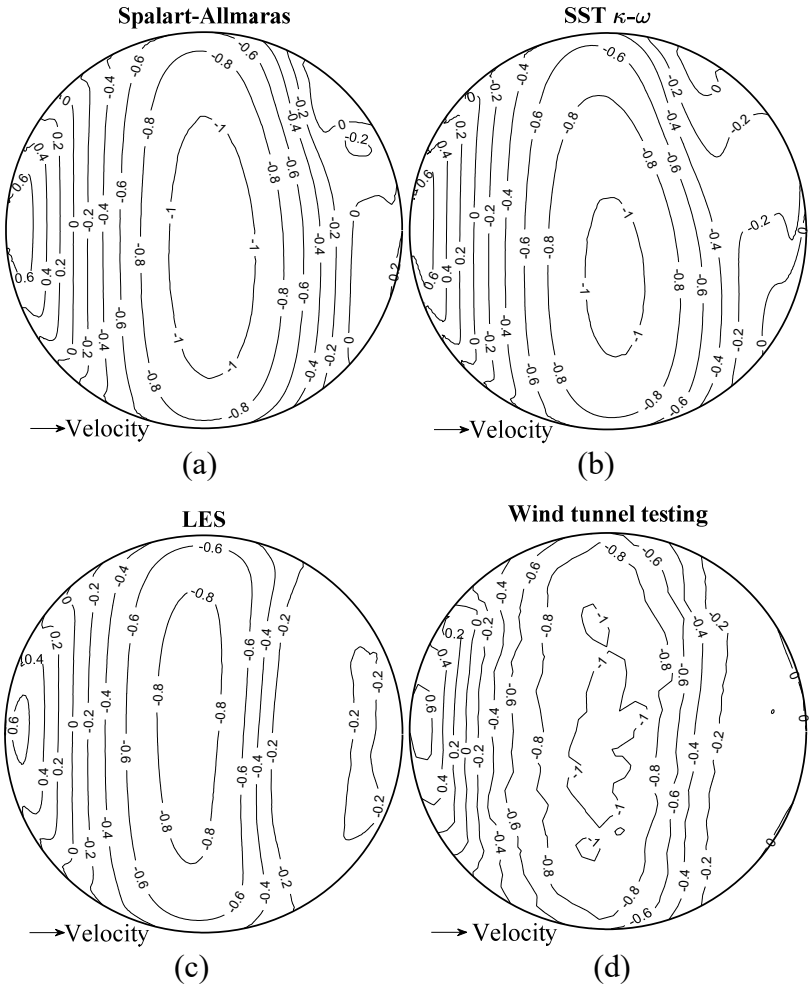

Figure 25. Pressure coefficient over open terrain at 95% throttle: (a) Spalart-Allmaras; (b) SST *k*-ω; (c) LES; (d) Wind tunnel testing.

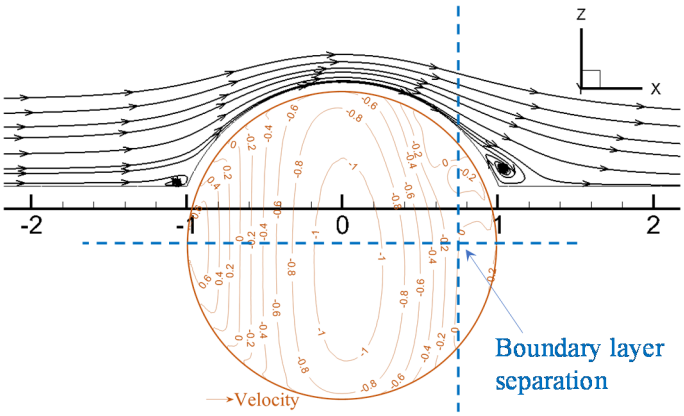

(a)

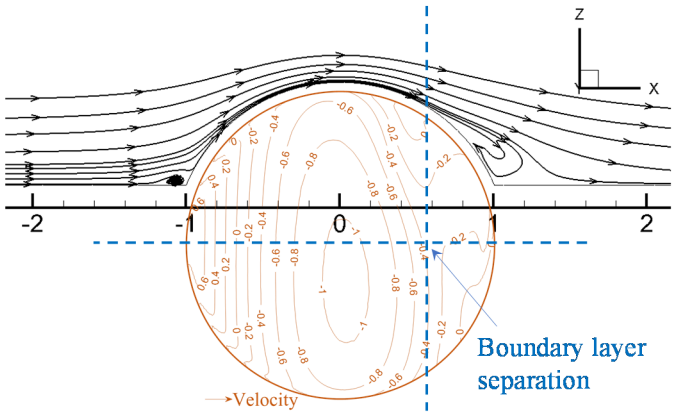

(b)

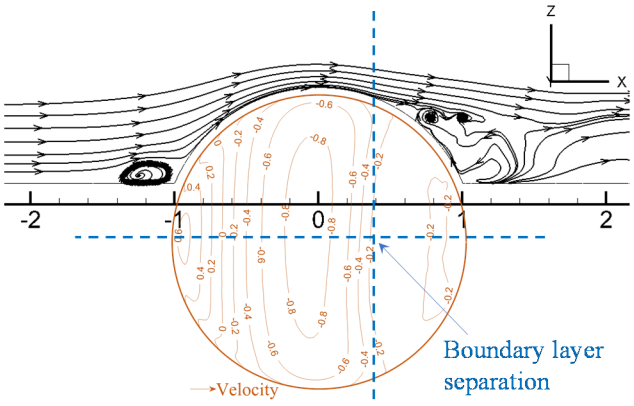

(c)

Figure 26. Pressure distribution on the dome surface superimposed on the streamline of the along-wind velocity around the dome model: (a) Spalart-Allmaras; (b) SST k-ω; (c) LES.

To be specific, for the pressure distribution associated with the SST k-ω model (Figure 25(b)), the maximum mean positive and negative pressure can match that from the wind tunnel testing data. However, the enclosed areas by the contour line of -1 and -0.8 appear to be smaller. For the pressure distribution associated with the LES model (Figure 25(c)), the maximum mean negative pressure is smaller than that from the wind tunnel testing. By closely examining the pressure distributions on the leeward side for each simulated case, the boundary layer separation occurs the earliest when the LES model is applied and the latest when the Spalart-Allmaras model is applied, as indicated in Figure 26. In terms of the location of the boundary layer separation, the obtained surface pressure distribution when the Spalart-Allmaras model is applied matches the wind tunnel testing better. The suction forces F_Z extracted from the cases associated with the Spalart-Allmaras, SST k-ω and LES models are 2205 N, 2044 N, and 1597 N, respectively, which are in the error of 2.5%, 5.0%, and 25.8% compared to that from the wind tunnel testing (2152 N). In summary, the simulated results associated with the Spalart-Allmaras model match the wind tunnel testing the best in terms of both the wind pressure distribution on the dome surface and the total suction force F_Z.

6. CONCLUSIONS

A large-scale (1/60) spherical dome model is tested in a straight-line wind tunnel and the wind tunnel testing is numerically simulated using CFD simulations. In the wind tunnel testing, the dome model is tested at three levels of fan throttles (52%, 74%, and 95%) over both open and suburban terrains. Systematic CFD simulations are conducted

to investigate the influence of turbulence modeling on the wind effects induced by the straight-line winds on the dome model. The following conclusions can be drawn:

- In the wind tunnel testing, when the fan throttle is doubled, the corresponding maximum mean positive and negative pressure coefficients increase four times. When the terrain type changes from open terrain to suburban terrain, the magnitudes of both positive and negative pressure coefficients are reduced due to higher surface roughness. Among all wind-induced forces and moments, suction force (F_Z) is the most significant.
- In the CFD simulations, the velocity input is obtained from the wind tunnel testing. Grid independence study is conducted. The coarser mesh (Mesh 3) is selected as the final meshing strategy due to its low computational cost.
- Three different turbulence models are applied, i.e., Spalart-Allmaras, SST k-ω, and LES models. The simulated results associated with the Spalart-Allmaras model match the wind tunnel testing the best in terms of both the wind pressure distribution on the dome surface and the total suction force F_Z. The simulated results associated with the LES model show the poorest accuracy of wind effects on the dome model, which is attributed to the earlier boundary layer separation compared to wind tunnel testing.
- The mismatch between the CFD simulations and the wind tunnel testing is mainly caused by the inaccurate prediction of boundary layer separation. This can be greatly improved by applying a proper turbulence model.

- Although the LES model is able to provide detailed, turbulent flow condition of the wind field, it may not be the best option when the averaged quantities are targeted to be matched.

ACKNOWLEDGEMENTS

This work was supported by the National Science Foundation [award number 1455709], the Hazard Mitigation and Structural Engineering program, through the project of "Damage and Instability Detection of Civil Large-scale Space Structures under Operational and Multi-hazard Environments".

REFERENCES

Blessmann J. Pressures on domes with several wind profiles. Proceedings of the 3rd International Conference on Wind Effects on Buildings and Structures, Tokyo, 1971, pp. 317-26.

Cheng CM, Fu CL. Characteristic of wind loads on a hemispherical dome in smooth flow and turbulent boundary layer flow. Journal of Wind Engineering and Industrial Aerodynamics. 2010;98(6-7):328-44.

Franke J, Hirsch C, Jensen AG, Krüs HW, Schatzmann M, Westbury PS, Miles SD, Wisse JA, Wright NG. Recommendations on the use of CFD in wind engineering. In Cost action C. 2004;14:C1.

Fu CL, Cheng CM, Lo YL, Cheng DQ. LES simulation of hemispherical dome's aerodynamic characteristics in smooth and turbulence boundary layer flows. Journal of Wind Engineering and Industrial Aerodynamics. 2015;144:53-61.

Germano M, Piomelli U, Moin P, Cabot WH. A dynamic subgrid-scale eddy viscosity model. Physics of Fluids A: Fluid Dynamics. 1991;3(7):1760-5.

Launder BE and Spalding DB. Lectures in Mathematical Models of Turbulence. Academic Press, London, England. 1972.

Letchford CW, Sarkar PP. Mean and fluctuating wind loads on rough and smooth parabolic domes. Journal of Wind Engineering and Industrial Aerodynamics. 2000;88(1):101-17.

Lilly DK. A proposed modification of the Germano subgrid-scale closure method. Physics of Fluids A: Fluid Dynamics. 1992;4(3):633-5.

Maher FJ. Wind loads on basic dome shapes. Journal of the Structural Division. 1965;91(3):219-28.

Meroney RN, Letchford CW, Sarkar PP. Comparison of numerical and wind tunnel simulation of wind loads on smooth, rough and dual domes immersed in a boundary layer. Wind and Structures. 2002;5(2/4):347-58.

Menter FR. Two-equation eddy-viscosity turbulence models for engineering applications. AIAA Journal. 1994;32(8):1598-1605.

Menter FR. Eddy viscosity transport equations and their relation to the k-ε model. Journal of Fluids Engineering. 1997;119(4):876-84.

Menter FR, Kuntz M, Langtry R. Ten years of industrial experience with the SST turbulence model. Turbulence, Heat and Mass Transfer. 2003;4(1):625-32.

Murakami S. Overview of turbulence models applied in CWE–1997. Journal of Wind Engineering and Industrial Aerodynamics. 1998;74:1-24.

Murakami S. Setting the scene: CFD and symposium overview. Wind and Structures. 2002;5(2_3_4):83-8.

Newman BG, Ganguli U, Shrivastava SC. Flow over spherical inflated buildings. Journal of wind engineering and industrial aerodynamics. 1984;17(3):305-27.

Nicoud F, Ducros F. Subgrid-scale stress modelling based on the square of the velocity gradient tensor. Flow, Turbulence and Combustion. 1999;62(3):183-200.

Ogawa T, Nakayama M, Murayama S, Sasaki Y. Characteristics of wind pressures on basic structures with curved surfaces and their response in turbulent flow. Journal of Wind Engineering and Industrial Aerodynamics. 1991;38(2-3):427-38.

Qiu Y, Sun Y, Wu Y. Characteristics of wind loads on spherical shells with large rise-span ratio. Advanced Materials Research. 2011;163:4149-55.

Savory E, Toy N. Hemisphere and hemisphere-cylinders in turbulent boundary layers. Journal of Wind Engineering and Industrial Aerodynamics. 1986;23:345-64.

Shih TH, Liou WW, Shabbir A, Yang Z, Zhu J. A new k-ϵ eddy viscosity model for high reynolds number turbulent flows. Computers & Fluids. 1995;24(3):227-38.

Simiu E, Scanlan RH. Wind Effects on Structures: Fundamentals and Applications to Design (3rd ed.). John Wiley and Sons, Inc; 1986.

Smagorinsky J. General circulation experiments with the primitive equations: I. The basic experiment. Monthly Weather Review. 1963;91(3):99-164.

Spalart P, Allmaras S. A one-equation turbulence model for aerodynamic flows. Recherche Aerospatiale.1994;1:5-21.

Taylor TJ. Wind pressures on a hemispherical dome. Journal of Wind Engineering and Industrial Aerodynamics. 1991;40(2):199-213.

Taniguchi S, Sakamoto H, Kiya M, Arie M. Time-averaged aerodynamic forces acting on a hemisphere immersed in a turbulent boundary. Journal of Wind Engineering and Industrial Aerodynamics. 1982;9(3):257-73.

Tavakol MM, Yaghoubi M, Motlagh MM. Air flow aerodynamic on a wall-mounted hemisphere for various turbulent boundary layers. Experimental Thermal and Fluid Science. 2010;34(5):538-53.

Tavakol MM, Abouali O, Yaghoubi M. Large eddy simulation of turbulent flow around a wall mounted hemisphere. Applied Mathematical Modelling. 2015;39(13):3596-618.

Tominaga Y, Stathopoulos T. Numerical simulation of dispersion around an isolated cubic building: model evaluation of RANS and LES. Building and Environment. 2010;45(10):2231-9.

Wood JN, De Nayer G, Schmidt S, Breuer M. Experimental investigation and large-eddy simulation of the turbulent flow past a smooth and rigid hemisphere. Flow, Turbulence and Combustion. 2016;97(1):79-119.

Wilcox DC. Turbulence modeling for CFD. La Canada, CA: DCW industries; 1998.

Yakhot VS, Orszag SA, Thangam S, Gatski TB, Speziale CG. Development of turbulence models for shear flows by a double expansion technique. Physics of Fluids A: Fluid Dynamics. 1992;4(7):1510-20.

II. INVESTIGATE THE INFLUENCE OF FLOW STRUCTURE OF A TORNADO ON WIND EFFECTS

Tiantian Li, Guirong Yan, and Daoru Han

ABSTRACT

Due to the incredible property loss and significant fatalities induced by tornadoes each year, tornado research has attracted considerable attention. However, previous studies mainly focused on the wind characteristics of tornadoes with the single-cell flow structure, and only a few targeted tornadoes with the double-cell flow structure. Limited attempts have been made for quantifying the tornado-induced wind effects on civil structures. The influence of flow structure of the tornado on its wind effects has not been sufficiently explored. This study is therefore aimed to investigate how the number of cells in the flow structure affects the wind effects acting on civil structures through Computational Fluid Dynamics (CFD) simulations. The paper is focused on the single-cell and double-cell flow structure, both of which belong to the category of single-vortex tornadoes. For completeness, the wind characteristics of both types of tornadoes are also studied and compared. The applied CFD simulation strategies are verified based on a real-world tornado. The obtained results show that, due to the central downdraft in the double-celled tornado, its turbulence intensity is higher than that of the single-celled tornado. The pressure profile for the double-celled tornado has a wide, flat distribution, while the corresponding profile for the single-celled tornado has a narrow, single peak. The two drag forces induced by the single-celled tornado follow a typical trend, i.e., they

reach their peak values when the dome center moves to the tornado core radius, while the corresponding variations under the double-celled tornado tend to be more random. Similar observations can be found from the two overturning moments. This suggests that the wind loading induced by the double-celled tornado is more dynamic than that induced by the single-celled tornado.

1. INTRODUCTION

In recent years, tornadoes have become a significant cause of injury, death, and property damage. On average, they cause $10B of property loss each year in the United States. Tornadoes are violently rotating columns of air that extend from a thunderstorm to the ground. They can generate intense winds at the speed of up to 135 m/s or 302 mph [1]. Due to the violent nature and unpredicted path of tornadoes, it is very challenging to obtain the in situ measurements of tornadoes, especially near-ground measurements [2]. Therefore, to characterize tornadic wind fields and to study tornado-induced wind effects on civil structures, researchers developed analytical models and simulated tornadoes using laboratory tornado simulators and Computational Fluid Dynamics (CFD) simulations.

Analytical modeling of tornadic wind flow has first been applied to investigate flow characteristics of tornado vortices. Several analytical models have been developed. The mathematical expressions of some representative analytical models are listed in Table 1. Rankine vortex model only defined tangential velocity (V_t) in the flow [3], as shown in Table 1. This model divided the vortex into two parts: the inner part of the

vortex in which V_t linearly increased with the radial distance and the outer part of the vortex in which V_t was a decreasing function of radial distance in hyperbolic form. The changeover from linear to hyperbolic form of V_t profile created a sharp pinnacle at core radius (designated as R_c, which was the radius where the maximum tangential velocity ($V_{t,max}$) occurred. Later on, Rankine model was modified by Deppermann [4]. A single equation was used to represent the vortex, and the sharp pinnacle at R_c observed in Rankine model was smoothed out. Then, a more advanced model (Burgers-Rott vortex model) was developed [5, 6], which defined all three wind velocity components (Tangential velocity V_t, Radial velocity V_r, and Axial velocity V_v) to better capture the wind characteristics of tornadoes. However, almost all the previous analytical models pertain to single-celled single-vortex tornadoes except the following. An analytical model (Sullivan model) of a double-celled tornado was proposed [7], and its mathematical expression is also listed in Table 1. In the flow generated by this model, V_r and V_v reversed their directions around the tornado center, generating a central recirculation pattern that was absent in the single-celled tornado. However, in this model, V_r grew without limits, which was not consistent with the real-world situation. Later on, a new model (Vatistas model) was reported for intense vortices [8], as shown in Table 1, which was able to produce a double-celled tornado by a proper selection of the scaling constants, e.g. κ=1.1, η=0.625, and β=0.6. In this model, the velocities were bounded. It was shown that V_r profile along a radius exhibited a direction reversal near the tornado center when a double-celled tornado appeared. Burgers-Rott model [5, 6] was employed to generate a single-celled vortex and Sullivan model [7] to generate a double-celled vortex to investigate the effects of different flow structures on the basic characteristics of

tornado vortices [9]. Recently, Manikis extended the work of Vatistas [8] to consider the time effect, decaying of vortices, on the double-celled tornadoes [10].

Table 1. Mathematical expression of analytical tornado models.

Vortex model	Radial velocity (V_r)	Tangential velocity (V_t)	Axial velocity (V_v)
Rankine model	0	$\frac{V_{t,max}r}{R_c}, r < R_c$ $\frac{V_{t,max}R_c}{r}, r \geq R_c$	0
Modified Rankine model	0	$\frac{2rV_{t,max}R_c}{r^2 + R_c^2}$	0
Burgers-Rott model	$-ar$	$\frac{\Gamma}{2\pi r}(1 - e^{-\frac{ar^2}{2\nu}})$	$2az$
Sullivan model	$-ar + \frac{6\nu}{r}(1 - e^{-\frac{ar^2}{2\nu}})$	$\frac{\Gamma}{2\pi r}\frac{H(\frac{ar^2}{2\nu})}{H(\infty)}$	$2az(1 - 3e^{-\frac{ar^2}{2\nu}})$
Vatistas model	$\alpha r(\frac{\kappa}{1 + \beta r^2} - \frac{1}{1 + \eta\beta r^2})$	$\frac{C_\infty}{r}\int_0^r \left[\frac{1 + \beta r^2}{(1 + \eta\beta r^2)^{(1/\eta\kappa)}}\right]^m rdr$	$2\alpha z[\frac{1}{(1 + \eta\beta r^2)^2} - \frac{\kappa}{(1 + \beta r^2)^2}]$

Note: $V_{t,max}$ denotes the maximum tangential velocity; R_c the core radius where $V_{t,max}$ is observed; r the radial distance from the vortex center; Γ the strength of circulation; a the strength of the suction; ν the kinematic viscosity; $H(x) = \int_0^x e^{f(t)}dt$, $f(t) = -t + 3\int_0^t (1 - e^{-y})\frac{dy}{y}$; α, κ, η, and β are scaling constants, $\alpha = \frac{2\eta\beta}{R_e\kappa}$; $C_\infty = 1/\int_0^\infty \left[\frac{1+\beta r^2}{(1+\eta\beta r^2)^{(1/\eta\kappa)}}\right]^m rdr$; $m = \frac{\alpha\kappa R_e}{2\beta}$, R_e is the Reynolds number.

Besides analytical modeling, experimental simulations also play an important role in generating essential features of real-world tornadoes. Ward developed the first laboratory tornado simulator and simulated single-celled tornadoes [11]. He investigated the influence of the aspect ratio on R_c and surface pressure profile. Later on, extensive laboratory simulations were conducted through the updated Ward-type simulators, and

different aspects regarding tornado flow characteristics were investigated [12-17]. For example, various tornado-like vortex configurations were generated as a function of swirl ratio (S), radial Reynolds number (R_{e_r}), and aspect ratio, including a single laminar vortex, a single vortex with breakdown, and multiple vortices [12, 13]. V_r and V_t as well as R_c of the tornado increase with the increase of S [13, 16]. The influence of tornado translation [14] and surface friction [15] on the wind field were also studied. Tornado translation caused a local increase in S and increased R_c compared to a stationary vortex. Surface friction made the flow more turbulent and thus caused greater eddy exchange of momentum. In addition to the Ward-type tornado simulator, tornadoes have been simulated and studied in the other two recently built laboratory tornado simulators at Iowa State University [18] and Western University [19] to characterize tornadic wind fields [20-23]. During the simulations in the Ward-type laboratory tornado simulator at Texas Tech University, the transition of the flow structure from a single-cell to a double-cell with the increase of S was observed [24, 25]. It was found that the aspect ratio not only affected R_c of both single- and double-celled tornadoes but also S at which the critical transition occurred. It also showed that the Burgers-Rott model [5, 6] closely fitted the averaged V_t profile of the single-celled tornado generated in the laboratory tornado simulator, and the Sullivan model [7] fitted the double-celled tornadoes produced in the lab very well.

In addition, CFD simulations have been applied to numerically simulate the different types of laboratory tornado simulators, including Ward-type tornado simulator, tornado simulators at Iowa State University and Western University, and the Atmospheric Vortex Engine, to investigate the generated tornado vortices and the airflow through

these tornado simulators [26-30]. Among these studies, Ishihara et al. [26] simulated a Ward-type tornado simulator and investigated both single- and double-celled tornadoes regarding the mean velocity field and pressure field. It was found that a single-celled tornado appeared when S is low and V_v showed peaks at the tornado center; and that a double-celled tornado appeared when S is high and $V_{t,max}$ appeared near ground.

Based on the comprehensive understanding of the tornado vortex itself, the tornado-induced wind effects and its static impact on civil structures have then been investigated [18, 28, 31-36]. A few attempts have also been made on the study of non-stationary characteristics of tornadoes. Dynamic wind pressure on a low-rise building frame was studied through laboratory tornado simulations and the results showed that the characteristics of dynamic pressures were strongly affected by the relative location of the structure to the tornado and were very different from those under straight-line winds [37]. Transient wind loads on a cubic building under a translating tornado were investigated in a laboratory simulator [38] and through CFD simulations [39]. In addition, tornado-induced wind loads on a low-rise gable-roofed building were explored in respect to S, translation speed and building parameters [40]. However, the tornadoes from which the wind effects are induced are mainly single-celled tornadoes.

According to the comprehensive literature review, previous studies were mainly focused on the characterization of the wind field induced by single-celled tornadoes and little if any research is about the comparison on the wind characteristics between single- and double-celled tornadic wind fields. Although Tang et al. [25] and Ishihara et al. [26] have compared single- and double-celled tornadoes through laboratory and numerical tornado simulations, respectively, their emphases were primarily on the mean velocity

field and pressure field, and they did not compare and discuss the characteristics of turbulence in the two tornadic wind fields and the tornado-induced wind effects on civil structures. However, turbulence can significantly affect the wind flow around civil structures and aerodynamic force; and can produce significant dynamic effect on some types of civil structures. To fill this research gap, in this study, CFD simulations will be employed to systematically investigate the differences between single- and double-celled tornadoes regarding the wind characteristics and the induced wind effects on civil structures. The remainder of this study is organized as follows. First, the civil structure of interest, a dome structure, will be introduced. The CFD simulation setup for generating a single-celled tornado and a double-celled tornado will be described. Second, the verification of the applied CFD simulation strategies will be demonstrated by comparing the simulated results to radar-measured data of a real-world tornado. Third, the wind characteristics of the two types of tornadoes will be investigated and compared, with respect to the flow structure, tangential velocity, turbulence intensity, and static pressure. At last, the wind effects on the dome structure induced by these two types of tornadoes will be compared in terms of the wind pressure on the dome surface and the total forces and moments.

2. SIMULATION OF TORNADIC WIND FIELD

2.1. CIVIL STRUCTURE CONSIDERED IN THIS STUDY

The civil structure considered in this study is a Kiewitt-type K6-7 single-layer spherical dome structure, as shown in Figure 1. It spans 75 m and rises 25 m. It consists

of 462 tubular beam members, which form a frame, and 294 shells, which cover the frame.

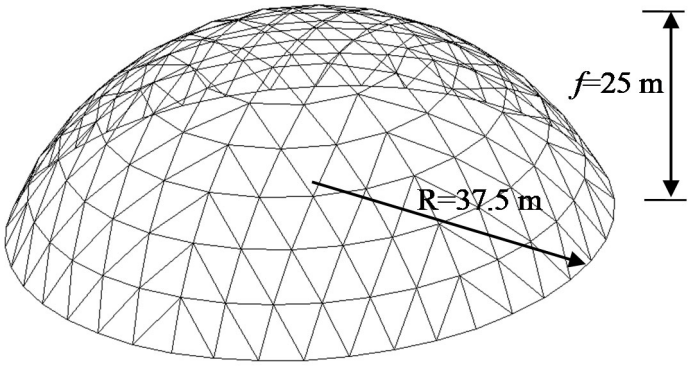

Figure 1. Spherical dome structure.

2.2. REAL-WORLD TORNADO SIMULATED IN THIS STUDY

Simulation of the tornadic wind field is based on a real-world F4 tornado, the Spencer, SD tornado of May 30, 1998 (hereafter "Spencer Tornado"). From the three-dimensional ground-based velocity track display analysis conducted by Kosiba and Wurman, a double-celled single-vortex flow structure is maintained for Spencer Tornado throughout their 8-min observation period [41]. Recent research findings also demonstrate the double-celled vortex structure of Spencer Tornado [42]. $V_{t,max}$ of Spencer Tornado is around 63 m/s, and its R_c fluctuates around 220 m at the elevation of 80 m during the observation period [28]. This tornado will be taken as the baseline and parameters will be adjusted to generate tornadoes with different flow structures, i.e., double- and single-celled flow structure. The CFD simulation software, ANSYS FLUENT, is employed to simulate the tornadic wind field.

2.3. ALL SIMULATED CASES AND SIMULATION SETUP

All simulated cases are listed in Table 2. Case 1 is simulated to reproduce Spencer Tornado and to verify the applied CFD simulation strategies. In Case 1, all civil structures are eliminated to simulate the tornadic wind field only; the radius of pressure outlet is set to be 340 m to achieve the double-celled flow structure. Case 2 is targeted to generate a tornado with the single-celled flow structure, which will be achieved by modifying the radius of the pressure outlet in Case 1 to 150 m. Again, no civil structures are present in this wind field. The results from Case 1 and Case 2 will be used to compare the wind characteristics of tornadic wind fields between double- and single-celled flow structures. In Cases 3 and 4, the dome structure described in Section 2.1 is placed in the computational domain in order to compare the wind effects on the dome surface induced by tornadoes with different flow structures.

Table 2. All cases simulated in this study.

Cases	Flow structure	With civil structure present?	Radius of pressure outlet (m)
Case 1	Double-celled	No	340
Case 2	Single-celled	No	150
Case 3	Double-celled	Yes	340
Case 4	Single-celled	Yes	150

Four different computational domains (Figure 2) are established corresponding to the four simulated cases. In each case, the computational domain consists of two cylinders to simulate the swirling wind flow. The bottom cylinder is 100 m high, resembling the inflow zone. The top cylinder is 1,000 m high, resembling the convection

zone. The radii of the two cylinders are both 800 m. The boundary condition on the inflow surface is velocity-inlet and that on the outflow circle is pressure-outlet. The rest top and side boundary surfaces are defined as symmetry. The bottom boundary surface is a no-slip wall when a stationary tornado is simulated and is a moving wall when a translating tornado is simulated. The main difference in CFD simulation setup between Cases 1 and 2 lies in the radius of the pressure outlet, which are 340 m and 150 m for Case 1 (Figure 2(a)) and Case 2 (Figure 2(b)), respectively. The dome structure is not present in these two cases. To investigate tornadic wind loads on dome structures, the dome structure is included in Case 1 and Case 2 to generate Case 3 (Figure 2(c)) and Case 4 (Figure 2(d)), respectively.

For all the four simulated cases, an inflow with tangential velocity (V_t) and radial velocity (V_r) enters the velocity inlet and exits from the pressure outlet. The equations used for V_t and V_r along the height are shown in Equations (1)-(2). They are obtained from the radar-measured data only at a location 800 m away from the tornado center through the height of 320 m. More details about the regression equations can be found in [43].

$$V_t = 20.61\left(\frac{z}{20}\right)^{0.1774} \tag{1}$$

$$V_r = \begin{cases} -31.14\left(\frac{z}{20}\right)^{0.169}, & z < 20 \text{ m} \\ 45.14\left(\frac{z}{20}\right)^{0.1826} - 76.48, & z \geq 20 \text{ m} \end{cases} \tag{2}$$

where z is the height above the ground.

Pointwise [44] is applied to develop the geometric model of the computational domain. For Cases 1 and 2, only structured mesh is applied. For Cases 3 and 4, hybrid

mesh is applied, including hexahedra, tetrahedra, pyramids and prisms. In Cases 1 and 2, inflation grid sizing is applied to the ground surface; in Cases 3 and 4, inflation grid sizing is applied to both the ground surface and the dome surface. The thickness of the first layer is 0.002 m and the corresponding Y+ value is 250 using the flat-plate boundary layer theory. The growth rate is 1.2 and a total of 36 layers is used. More details about the mesh strategies can be found in [43].

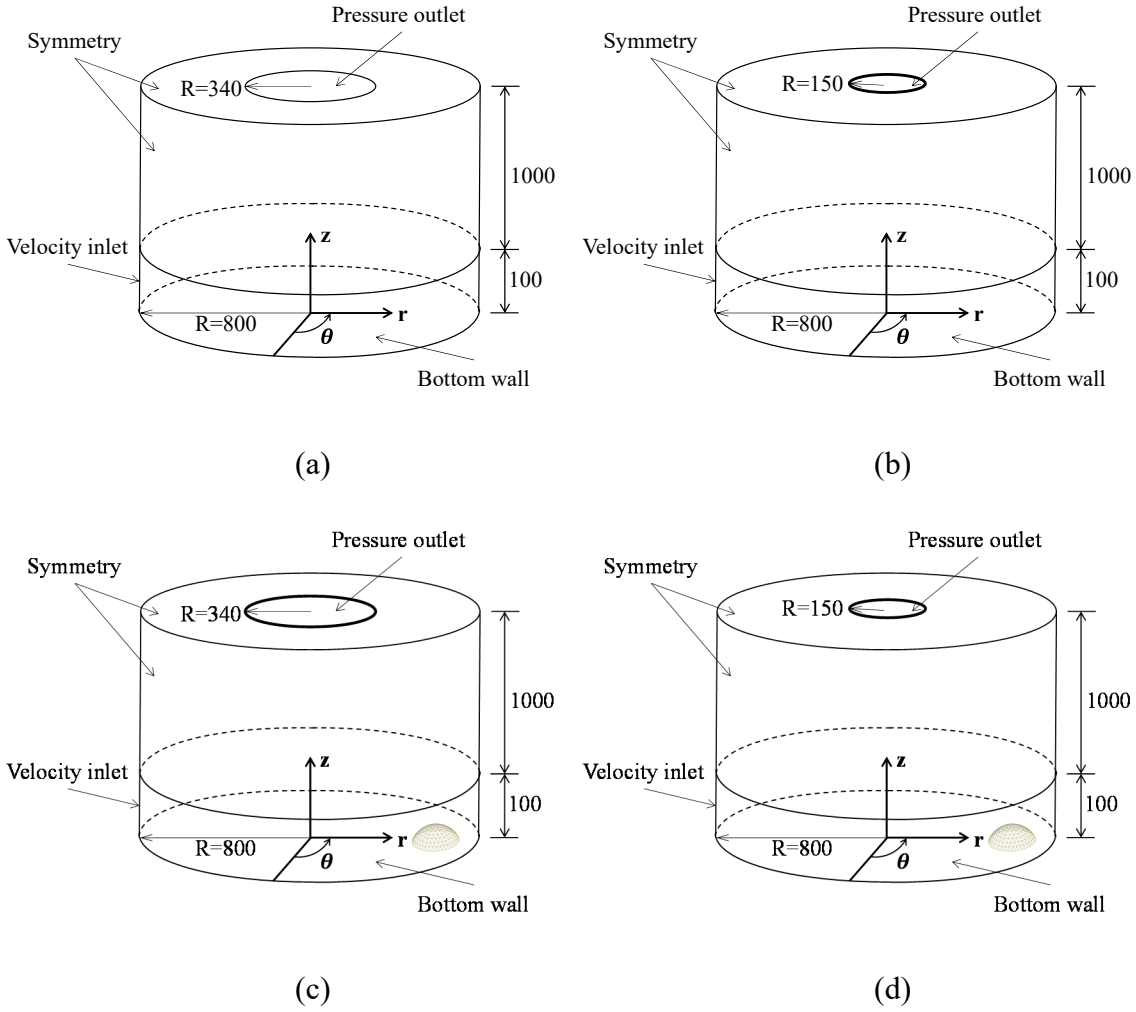

Figure 2. Computational domains of the simulated tornadic wind fields (unit: m): (a) Case 1; (b) Case 2; (c) Case 3; (d) Case 4.

2.4. SIMULATION OF TORNADO TRANSLATION

In Cases 3 and 4 where the dome structure is present, the whole process of a tornado translating over the dome structure is simulated to determine more realistic tornadic wind loads. To simulate the tornado translation, rather than having the tornado move, the dome structure is made to move at the same speed as tornado translating, but in the opposite direction to the direction of tornado translating, to establish the relative motion. As shown in Figure 3, the dome structure is originally located at 360 m on the X axis (t = 0 s). To simulate that the tornado translates to the right, the dome translates to the left (along the negative X direction) at a speed of 15 m/s, which is the translating speed of Spencer Tornado based on the field measurement data [45]. When t = 24 s, the dome center reaches the tornado center. The calculation terminates when the dome structure moves to -360 m on the X axis (t = 48 s). In the CFD simulation, the dynamic mesh technique is applied to simulate that the dome structure travels inside the computational domain. Besides, to simulate the relative motion between the ground plane and the tornado, a moving wall boundary condition is applied on the ground plane with the speed of 15 m/s in the negative X direction. Details about the application of dynamic mesh can be found in [43].

3. VERIFICATION OF THE APPLIED CFD SIMULATION STRATEGIES

Case 1 aims to reproduce Spencer Tornado, a double-celled tornado. To verify the applied CFD simulation strategies, the obtained simulation results are compared with the

radar-measured data in terms of the tangential velocity profile (V_t), radial Reynolds number (R_{e_r}) and swirl ratio (S), as well as the flow structure on the vertical plane.

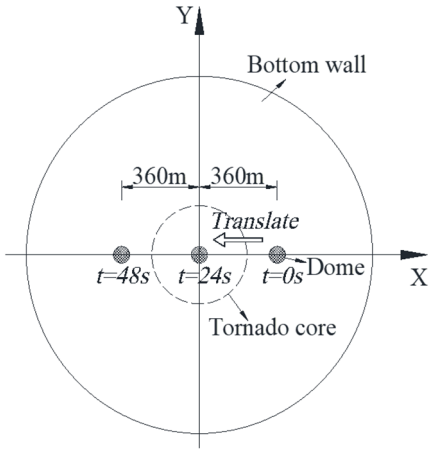

Figure 3. Schematic diagram of the simulation of tornado translation.

3.1. PROFILE OF TANGENTIAL VELOCITY (V_t)

The comparison between the simulated results and the radar-measured data is shown in Figure 4, with respect to the averaged V_t profile as a function of radial distance at the elevation of 80 m. V_t profile at the elevation of 80 m is selected to do the comparison to eliminate the requirement of matching the ground roughness between the CFD simulation and radar measurement, assuming that the influence of ground roughness on the wind flow at the elevation of 80 m is minimal. To achieve an appropriate comparison, the averaging method applied to the simulated V_t profile is the same as the one applied to process the radar-measured data [28]. To be specific, first, V_t along a radius on the horizontal 80-m-high plane is extracted during a period of 20 s, and then it is time-averaged. Time-averaged V_t along 36 radii are obtained. Next, the space-averaged

V_t at each specified radial distance is calculated by averaging the values at the same radial distance over the 36 azimuth angles. A data regression technique is applied on the time-averaged V_t profile along each radius to ensure the data availability at the specified radial distances. A similar method was also used to obtain the averaged V_t from laboratory tornado simulations [16, 23, 46]. As shown in Figure 4, the averaged V_t profile obtained from the CFD simulation is in agreement with that obtained from the radar-measured data. From Figure 4, tornado center is located at the radial distance of 0 m; R_c of the simulated tornado is 230 m and the corresponding $V_{t,max}$ is 65 m/s. In terms of R_c and $V_{t,max}$, the simulated results match the radar-measured data very well.

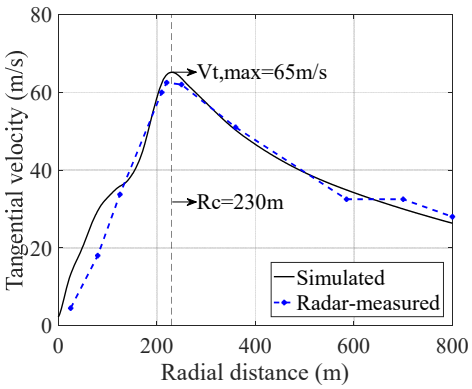

Figure 4. Comparison of the tangential velocity profiles extracted from the CFD simulation (Case 1) and the radar-measured data.

3.2. RADIAL REYNOLDS NUMBER (R_{e_r}) AND SWIRL RATIO (S)

R_{e_r} and S control the flow structure of the tornado [13]. R_{e_r} is essentially a measure of the relative amount of the flow updraft strength to flow viscosity, reflecting the degree of flow turbulence, and it is defined as the ratio of volume flow rate to viscosity:

$$\mathrm{R}_{e_r} = \frac{Q'}{2\pi\nu} = \frac{Q}{2\pi\nu h} \tag{3}$$

where Q' represents the volume flow rate per unit axial length of inflow height and Q represents the total volume flow rate through the system. Herein, $Q = 1.15 \times 10^7$ m^3/s. ν denotes kinematic viscosity (1.53×10^{-5} m^2/s), and h denotes the height of the velocity inlet (100 m). R_{e_r} of the simulated tornado is 1.20×10^9, which falls into the estimated range of actual tornado cyclone flows, 10^9-10^{11} [13].

S is essentially a measure of the relative amount of angular to radial momentum in the vortex, reflecting the amount of rotational energy in the vortex relative to the convective energy in the vortex [18]. S at a certain height is defined as:

$$\mathrm{S} = \frac{\pi {R_c}^2 V_{t,max}}{Q} \tag{4}$$

where R_c is the core radius at that specific height, and $V_{t,max}$ is the corresponding maximum V_t (the V_t at R_c) at that height. S of the simulated tornado at seven representative heights are presented in Figure 5. S is larger than 1 within 200 m, which is consistent with the radar observation that S of Spencer Tornado exceeds 1 [41]. It is also consistent with the conclusions drawn by Hangan and Kim [47], in which the best fit between the CFD data and the radar-measure data from Spencer Tornado was found for a S of approximately S=2.

3.3. VERTICAL FLOW STRUCTURE

The schematic diagrams of ideal tornadic flow structures on a vertical plane are shown in Figure 6 [48]. Figure 6(a) presents a double-celled single-vortex flow structure, which is formed when S is relatively high. A downdraft is formed at the tornado center

and touches the ground surface, widening the corner flow. Figure 6(b) presents a single-celled single-vortex flow structure and it is formed when S is low. No downdraft is observed and the corner flow forms an intense lateral inflow and upward jet.

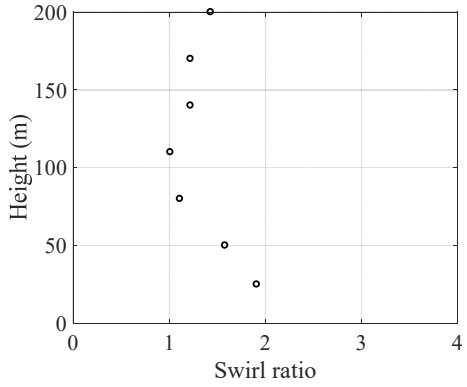

Figure 5. Swirl ratio at representative heights for Case 1 (double-celled tornado).

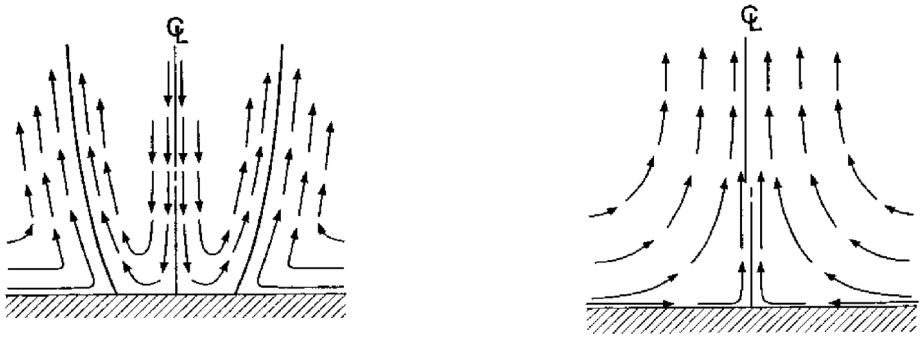

(a) (b)

Figure 6. Schematic diagrams of tornadic flow structures on the vertical plane [48]: (a) Double-celled single-vortex flow structure; (b) Single-celled single-vortex flow structure.

To demonstrate a double-celled single-vortex tornado is generated in Case 1, the instantaneous flow structure of the simulated tornado at 300 s is shown in Figure 7. It is extracted from a meridional plane of the computational domain. From the flow structure on the vertical plane, it can be seen that a downdraft is formed at the tornado center,

impinging the ground, indicating a double-celled flow structure comparing to Figure 6(a). Such a central downdraft is a main feature of double-celled tornadoes, as also reported by Fiedler and Rotunno [49]. Updraft is formed at the outer region. Small vortices are formed due to local turbulence of airflow. Thus far, the simulated results are in general agreement with the radar-measured data, thus validating the feasibility of the applied CFD simulation strategies. Further analyses will be conducted based on these CFD simulation strategies.

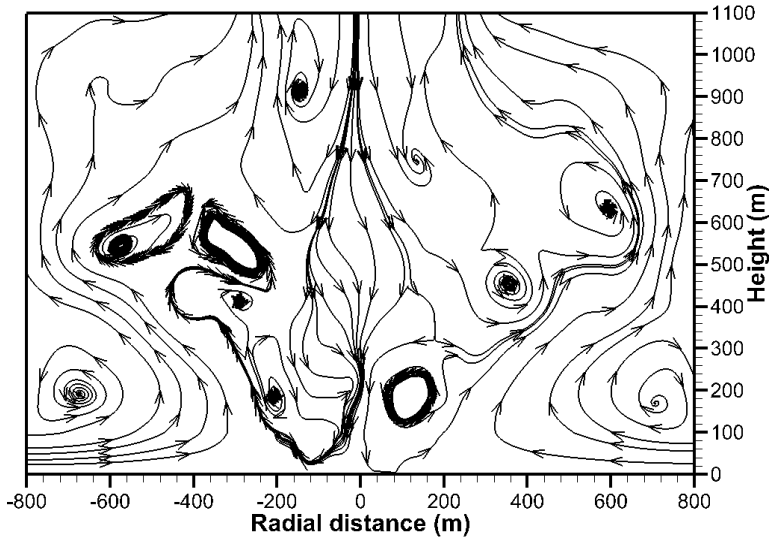

Figure 7. Instantaneous flow structure of the simulated tornado in Case 1 (double-celled tornado).

4. COMPARISON ON WIND CHARACTERISTICS OF TORNADIC WIND FIELD

In this section, the wind characteristics of tornadic wind field with the two different flow structures will be investigated. Comparisons between Cases 1 and 2 will be

made regarding the flow structure, tangential velocity (V_t), turbulence intensity (TI), and static pressure.

4.1. TORNADIC FLOW STRUCTURE

The instantaneous flow structures on the vertical plane of the two types of tornadoes at 300 s are shown in Figure 8. Figure 8(a) is for the double-celled tornado, which is exactly the same as Figure 7 and duplicated here for convenience. From Figure 8, updraft is formed at the outer region of the computational domain for both cases. However, downdraft is only formed at the tornado center of the double-celled tornado (Figure 8(a)), while the airflow at the tornado center of the single-celled tornado is still updraft (Figure 8(b)). This is the main difference between double- and single-celled tornadoes regarding the flow structure on the vertical plane. Small vortices due to local turbulence are observed for both cases. In general, the flow structures of both cases match the corresponding schematic diagram of ideal tornadic flow structure (Figure 6) well.

According to Equation (4), S is determined as 1.1 for the double-celled tornado and 0.12 for the single-celled tornado at the elevation of 80 m. S is consistent with the research findings about the effect of increasing S on tornadic flow structure [16, 25, 26, 46, 48], i.e., a double-celled tornado is formed when S is high and a single-celled tornado is formed when S is low. Based on Equation (3), R_{e_r} of both cases is the same, that is, 1.20×10^9, since they share the same velocity input and dimensions at the velocity inlet.

The instantaneous flow structure (at 300 s) on the horizontal plane at the elevation of 25 m is shown in Figure 9. The elevation of 25 m is chosen, as this is the height of the dome apex. In both cases, the air rotates counterclockwise. From the radius where $V_{t,max}$

is reached (core radius, R_c), R_c for the double-celled tornado (Case 1) is 159 m and that for the single-celled tornado (Case 2) is 56 m. Here, R_c is instantaneous result that is determined based on this time instant of data. As shown in Figure 9(a), it is interesting to point out that, the outer air flows in towards R_c, and the inner air flows out towards R_c due to the centrifugal force induced by the air rotation. In other words, the airflow converges at R_c for the double-celled tornado. For the single-celled tornado, a similar phenomenon is observed but the airflow converges at a radial distance that is 50 m away from R_c, as shown in Figure 9(b). The convergence location of the airflow depends on the force balance between the pressure gradient force (inwards) and the centrifugal force (outwards). For the single-celled tornado (Case 2), $V_{t,max}$ is much higher (see Figure 10), leading to a much higher centrifugal force. This is why the convergence location of the airflow is further away from R_c. Based on the flow analysis on the horizontal plane, it is worth noting that the large atmospheric pressure drop at tornado center (the maximum negative pressure) is due to the fact that the air flows outwards in the core region.

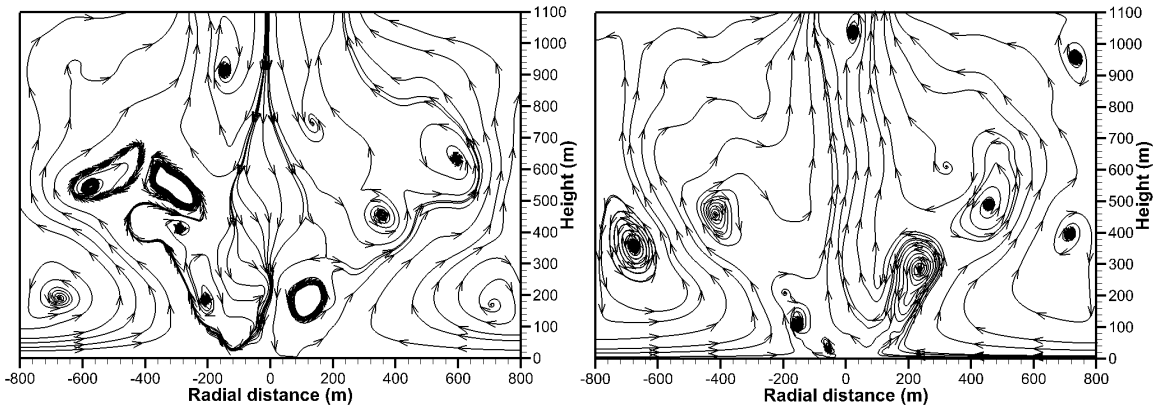

(a) (b)

Figure 8. Instantaneous flow structure on the vertical plane of the tornadic flow: (a) Case 1: Double-celled; (b) Case 2: Single-celled.

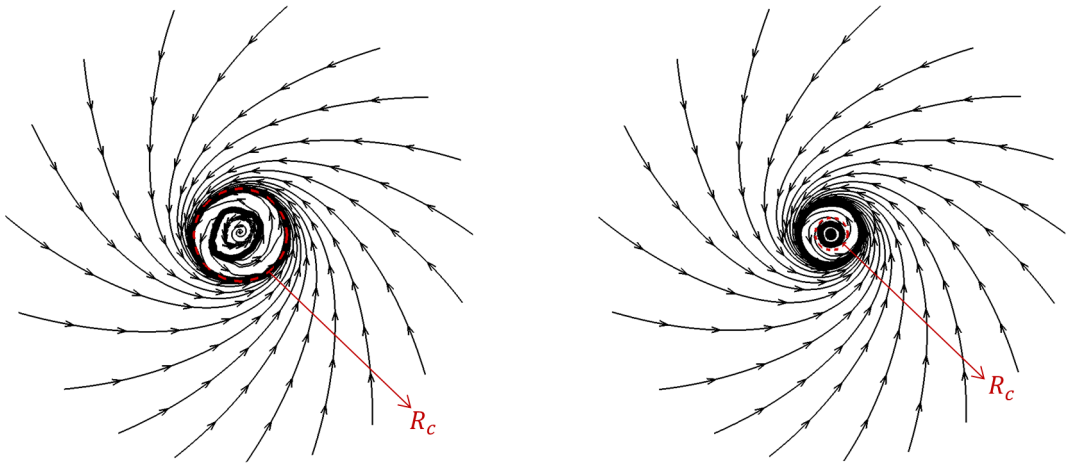

(a) (b)

Figure 9. Instantaneous horizontal flow structure of the tornadic wind field at the elevation of 25 m (Note: R_c denotes the core radius in each case): (a) Case 1: Double-celled; (b) Case 2: Single-celled.

4.2. TANGENTİAL VELOCİTY (V_t)

Instantaneous contour plots of V_t on the horizontal plane at the elevation of 25 m at 300 s are shown in Figure 10. For both cases, the distribution of V_t is in the pattern of concentric circles. R_c of the double-celled tornado is much larger than that of the single-celled tornado. They are 159 m and 56 m, respectively, and indicated by dashed circles in Figure 10. $V_{t,max}$ of the single-celled tornado (214 m/s) is much larger than that of the double-celled tornado (98 m/s), which can be explained by the conservation of angular momentum. The minimum V_t for both cases is similar. Here, R_c and $V_{t,max}$ are instantaneous results based on this time instant of data.

To be more specific, V_t profiles along one radius at the elevation of 25 m and 80 m are presented in Figure 11. Here, V_t is time- and space-averaged. For both elevations, R_c of the double-celled tornado is larger than that of the single-celled tornado, while $V_{t,max}$ of the double-celled tornado is smaller. Qualitatively, this is consistent with the

conservation of the angular momentum. Figure 12 presents the instantaneous V_t profile (space-averaged) at the elevation of 25 m for both types of tornadoes. It is in general agreement with the corresponding time- and space-averaged V_t profile, although some extra peaks show up, which is due to the turbulence in tornadic wind field.

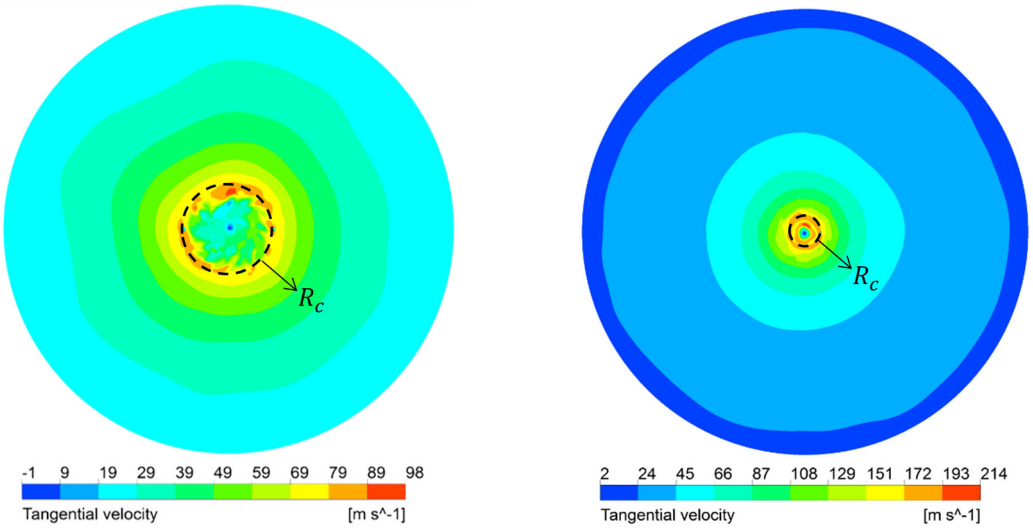

(a) (b)

Figure 10. Instantaneous contour plots of tangential velocity on the horizontal plane at the elevation of 25 m: (a) Case 1: Double-celled; (b) Case 2: Single-celled.

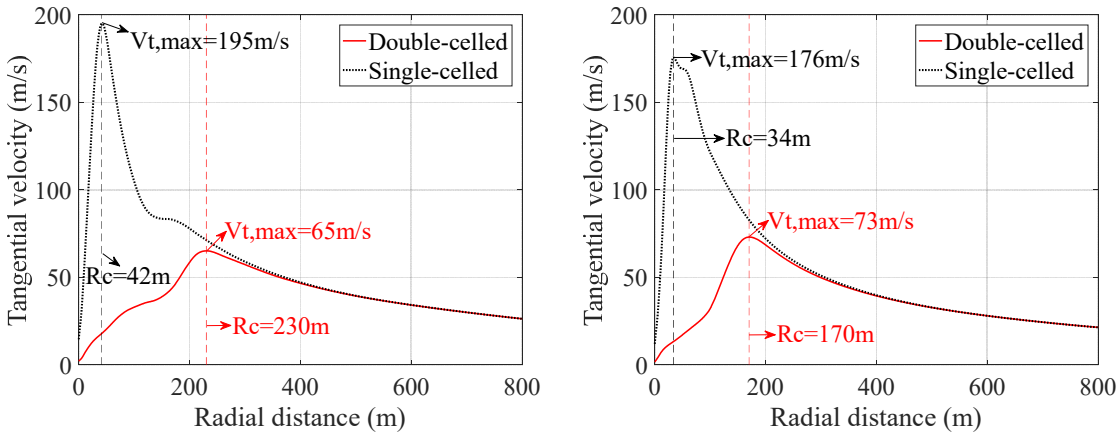

(a) (b)

Figure 11. Time- and space-averaged profile of tangential velocity along radial distance: (a) At the elevation of 80 m; (b) At the elevation of 25 m.

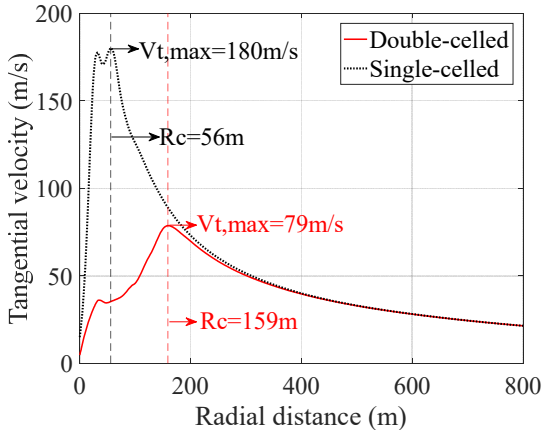

Figure 12. Instantaneous profile of tangential velocity along radial distance at the elevation of 25 m (space-averaged).

Instantaneous contour plots of V_t on a meridional plane at 300 s is shown in Figure 13. For lower elevations, in both cases, the distribution of V_t is symmetric about the central axis; for higher elevation, the distribution of V_t for the double-celled tornado (Case 1) is less symmetric than that for the single-celled tornado (Case 2). This is due to the fact that there exists central downdraft and the airflow is more turbulent in the double-celled tornado.

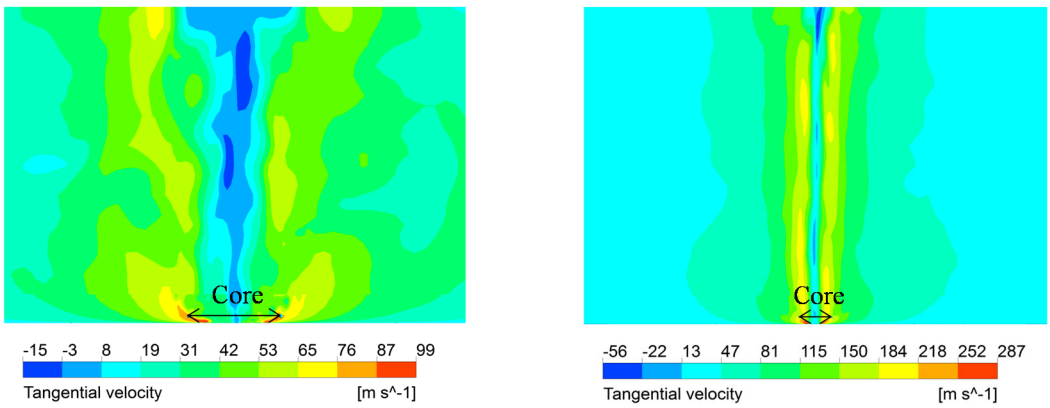

(a) (b)

Figure 13. Contour plot of tangential velocity on the vertical plane: (a) Case 1: Double-celled; (b) Case 2: Single-celled.

4.3. TURBULENCE İNTENSİTY (TI)

TI is used to measure the strength of turbulence, which in this study is obtained based on the time histories of wind velocity at the elevation of 25 m. TI is defined as the ratio of the root-mean-square of velocity fluctuation to the mean resultant velocity [50]:

$$TI_u = \frac{\sigma_u}{U}, \qquad TI_v = \frac{\sigma_v}{U}, \qquad TI_w = \frac{\sigma_w}{U} \tag{5}$$

where $\sigma_u^2 = \frac{1}{T}\int_0^T u^2 dt$, $\sigma_v^2 = \frac{1}{T}\int_0^T v^2 dt$, and $\sigma_w^2 = \frac{1}{T}\int_0^T w^2 dt$; u, v, and w are the velocity fluctuation in the radial, tangential and axial directions; U is the mean resultant wind velocity.

Based on Equation (5), TI at different radial distances in the axial, radial, and tangential directions for both cases are obtained and presented in Figure 14. Radial distance is normalized using R_c of each case, i.e., 170 m for the double-celled tornado (Figure 11(b)) and 34 m for the single-celled tornado (Figure 11(b)).

From Figure 14, for the single-celled tornado, TIs of the three velocity components are similar. For the double-celled tornado, TI of the axial velocity component is much higher than TIs of the other two velocity components; and TI of each velocity is generally larger than that of the single-celled tornado, especially at the locations close to the tornado center. Both phenomena are attributed to the presence of the central touching-down downdraft in the double-celled tornado. This indicates that the airflow of the double-celled tornado is more turbulent than that of single-celled tornado, which also demonstrates the aforementioned statement that the vertical distribution of V_t for the double-celled tornado is less symmetric than that for the single-celled tornado at higher elevations.

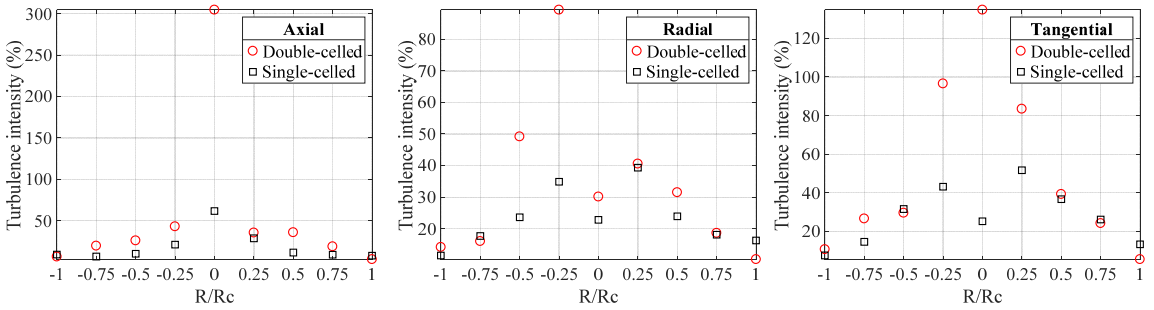

(a) (b) (c)

Figure 14. Comparison of turbulence intensity between Case 1 and Case 2: (a) For axial velocity; (b) For radial velocity; (c) For tangential velocity.

To demonstrate the fluctuations in velocities, the time histories of V_t for both cases at three representative locations, i.e., R_c, half of R_c and tornado center, are presented in Figures 15-16. For both cases, the mean value decreases when the radial distance gets closer to the tornado center. At each representative radial distance, although V_t of the double-celled tornado fluctuates less frequently than that of the single-celled tornado and the corresponding variance of the velocity data is much smaller, TI of the double-celled tornado is higher based on Equation (5) due to the lower mean V_t in the double-celled tornado.

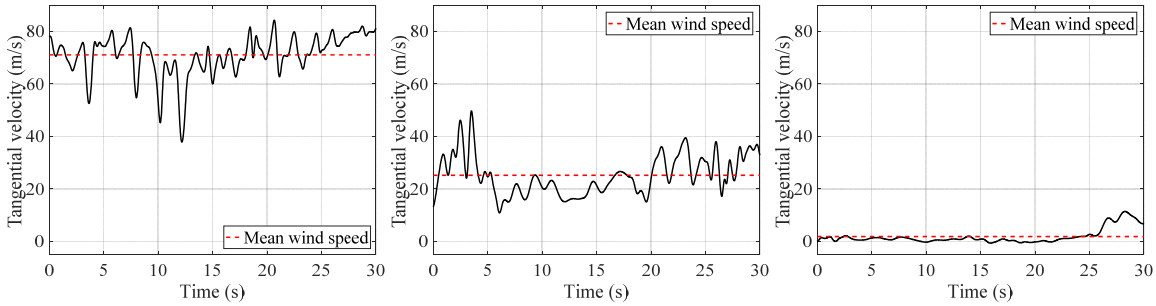

(a) (b) (c)

Figure 15. Time histories of tangential velocity of the double-celled tornado: (a) At R_c, $\sigma_v = 7.7$; (b) At half of R_c, $\sigma_v = 7.5$; (c) At tornado center, $\sigma_v = 2.8$ (Note: σ_v denotes the root-mean-square of tangential velocity fluctuation).

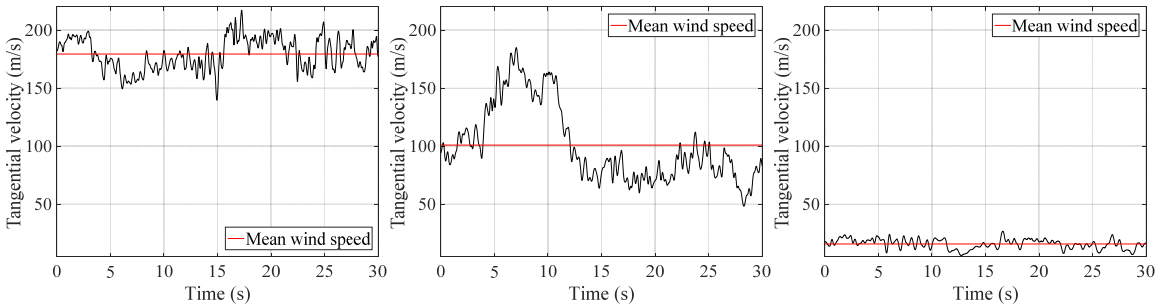

Figure 16. Time histories of tangential velocity of the single-celled tornado: (a) At R_c, $\sigma_v = 13.7$; (b) At half of R_c, $\sigma_v = 32.9$; (c) At tornado center, $\sigma_v = 4.1$.

4.4. STATIC PRESSURE

Figure 17 shows the instantaneous contour plots of static pressure on the horizontal plane at the elevation of 25 m at 300 s. It is shown that, for both cases, the distribution of static pressure is in the pattern of concentric circles. Within the tornado core, negative pressure is present due to a high atmospheric pressure drop. Static pressure increases with the increase of radial distance. It is also observed that the distribution of negative pressure within R_c is scattered for the double-celled tornado (Figure 17(a)) and is centered for the single-celled tornado (Figure 17(b)). This further verifies that the double-celled tornado is more turbulent inside the tornado core than the single-celled tornado.

To be more specific, the profile of static pressure along a diameter of the computational domain is shown in Figure 18. Here, static pressure is time- and space-averaged. In both cases, the maximum negative pressure occurs at the tornado center, as the air flows outwards away from tornado center within the tornado core. There are three main differences between the two cases. First, the pressure gradient of the double-celled tornado is much smaller than that of the single-celled tornado. Second, for the double-

celled tornado, the region with the maximum negative pressure is wide, while that for the single-celled tornado is narrow, exhibiting as a peak. Third, the pressure magnitude range of the double-celled tornado is much smaller than that of the single-celled tornado. These findings are consistent with experimental results obtained from laboratory tornado simulators [25, 51].

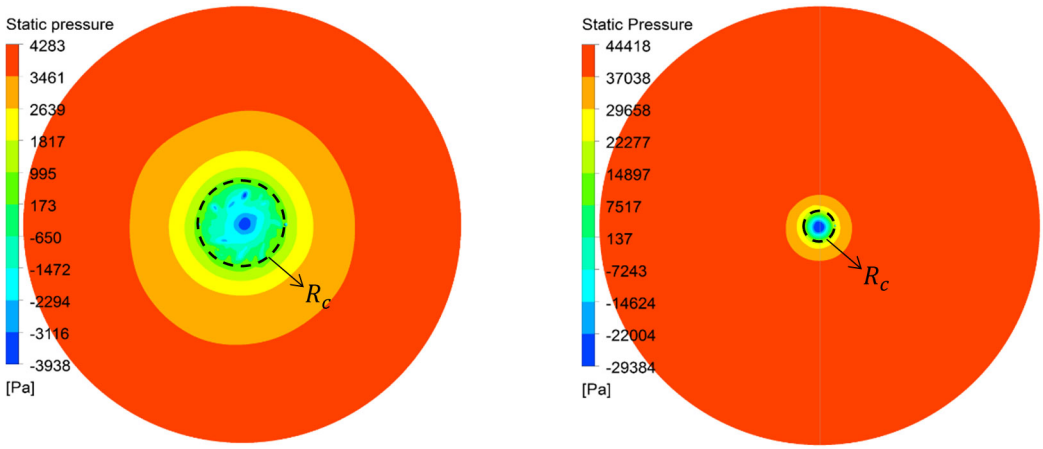

(a) (b)

Figure 17. Instantaneous contour plot of static pressure on the horizontal plane at the elevation of 25 m: (a) Case 1: Double-celled; (b) Case 2: Single-celled.

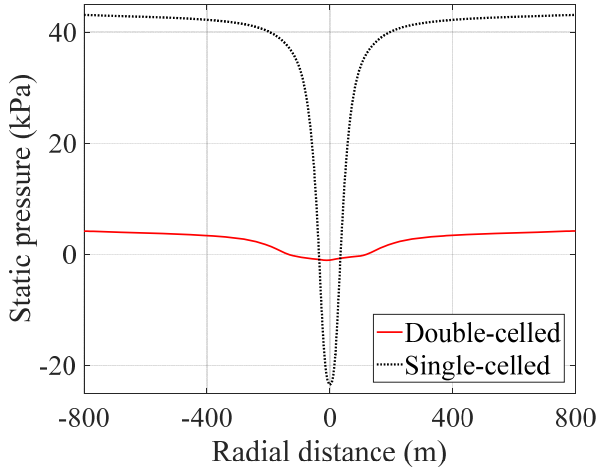

Figure 18. Static pressure profile as a function of radial distance.

5. COMPARISON ON TORNADO-INDUCED WIND EFFECTS ON THE DOME STRUCTURE

In this section, tornado-induced wind effects are compared between Cases 3 and 4 when the dome structure is present in the wind field. The wind effects presented here include the wind pressure on the dome surface (hereafter "surface pressure") and total forces and moments acting on the entire dome.

5.1. SURFACE PRESSURE

Surface pressure induced by the double-celled tornado (Case 3) at six representative time instants during the last 48 s of simulation (while the dome moves from the right side to the left side of tornado center, see Figure 3) are presented in Figure 19. In general, all surface pressure is positive when the dome is far away from tornado center (Figure 19(a)), while negative surface pressure is gradually developed when the dome approaches the tornado center. From Figure 19(b), when the dome is closer to the tornado center, since it is on the right side of the tornado center, the wind blows towards the southeast corner of the dome, at which the surface pressure is positive. As shown in Figure 19(c), when the dome center moves to R_c (Here, R_c is 170 m, which is at the height of the dome apex, 25 m, and is determined from Case 1 when the dome structure is not present, see Figure 11(b)), the wind blows from due south and the surface pressure near the south edge of the dome is positive. From Figure 19(d), when the dome center is exactly at the tornado center, relatively uniform negative pressure is distributed across the whole surface. The negative pressure is contributed from the large atmospheric pressure drop within the tornado core (see Figure 18). When the dome moves to the left side of the

tornado center (Figures 19(e)-(f)), large positive pressure is found at the northwest corner of the dome, which is the windward direction.

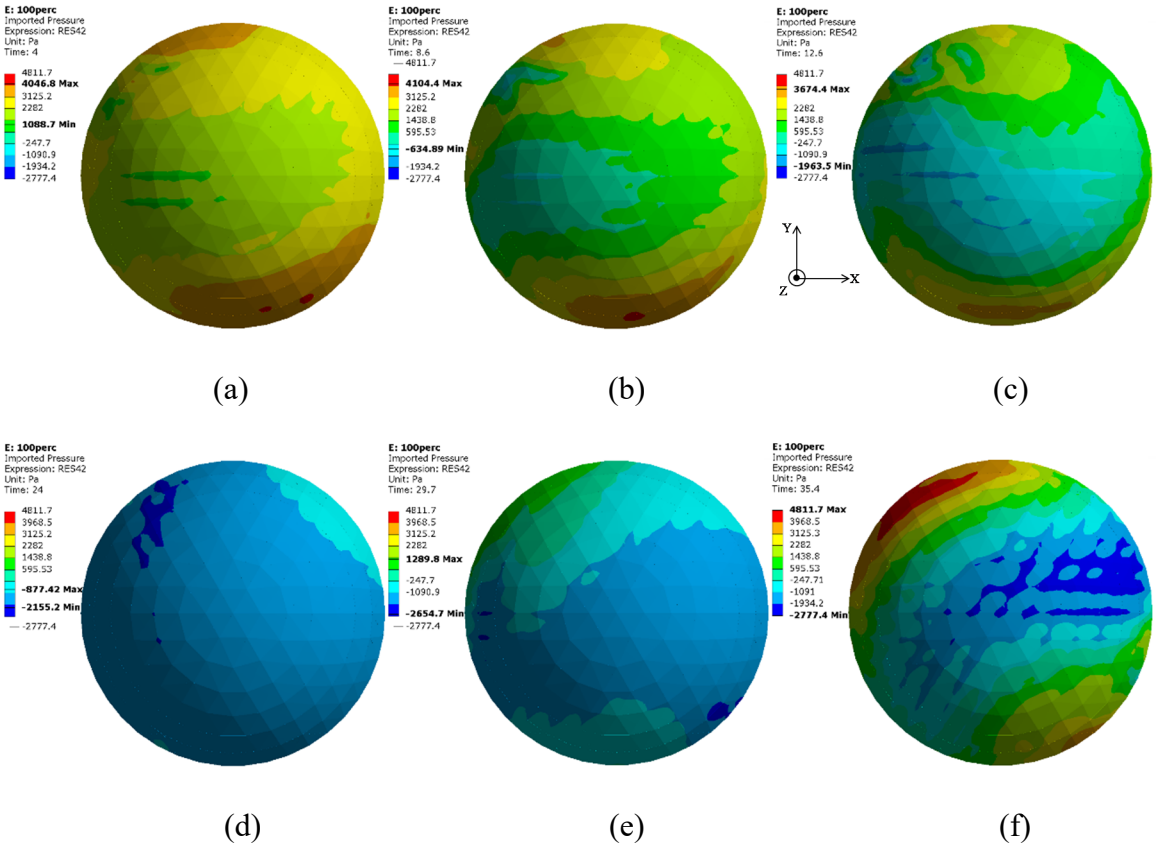

Figure 19. Surface pressure for the double-celled tornado (Case 3): (a) 4 s (300 m away from tornado center); (b) 8.6 s (231 m away from tornado center); (c) 12.6 s (171 m away from tornado center); (d) 24 s (0 m away from tornado center); (e) 29.7 s (-85.5 m away from tornado center); (f) 35.4 s (-171 m away from tornado center).

Figure 20 shows the surface pressure induced by the single-celled tornado (Case 4). The general trend is similar to that induced by the double-celled tornado, that is, all surface pressure is positive when the dome is far away from the tornado center, while negative surface pressure is developed when the dome gets closer to the tornado center. In this case, R_c is 34 m at the elevation of 25 m (Figure 11(b)).

By comparing Figures 19(a) and 20(a), when the dome center is 300 m away from the tornado center, the distribution of positive surface pressure induced by the single-celled tornado is more uniform than that induced by the double-celled tornado. This is because the tornado core of the single-celled tornado is much smaller, and the negative pressure at tornado center exerts less influence on the airflow at the 300-m radius. Therefore, the pressure gradient at the 300-m radius in the single-celled tornado is much smaller (see Figures 21(a) and 22(a)), and thus induces less uneven distribution of surface pressure.

When the dome is at the tornado center, the distribution of surface pressure induced by the double-celled tornado (Figure 19(d)) is more uniform than that induced by the single-celled tornado (Figure 20(d)). This is due to the influence of the relative size of the tornado core and the dome structure. The core diameter of the double-celled tornado is 340 m at the elevation of 25 m, which is 4.5 times the base diameter of the dome structure (75 m). The similar ratio for the single-celled tornado is around 0.9. This indicates that the size of the dome structure is much less than the core of the double-celled tornado, which means the dome structure is completely immersed in the lower pressure region. Therefore, the distribution of surface pressure is much uniform under the double-celled tornado.

It is also interesting to notice that a spot of localized peak negative pressure occurs in Figures 20(c)-(e), and it is indicated by the dark blue color in each subfigure. The tornado core of the single-celled tornado is affected by the dome structure more significantly than the tornado core of the double-celled tornado, which can be observed clearly from Figures 21-22.

As presented in Figure 21, for the double-celled tornado, the pressure distribution within the tornado core is scattered, on which the influence of the dome structure is not noticeable. As presented in Figure 22, for the single-celled tornado, when the dome structure is far away from the tornado center, the pressure is distributed in concentric circles and centered at the core. When the dome moves close to the core, the pattern of concentric circles is disturbed by the dome structure and the localized peak negative pressure is observed, i.e., Figures 22(c)-(d). The localized peak negative pressure in Figures 22(c)-(d) corresponds with the spot of localized peak negative pressure on the dome surface in Figures 20(c)-(d).

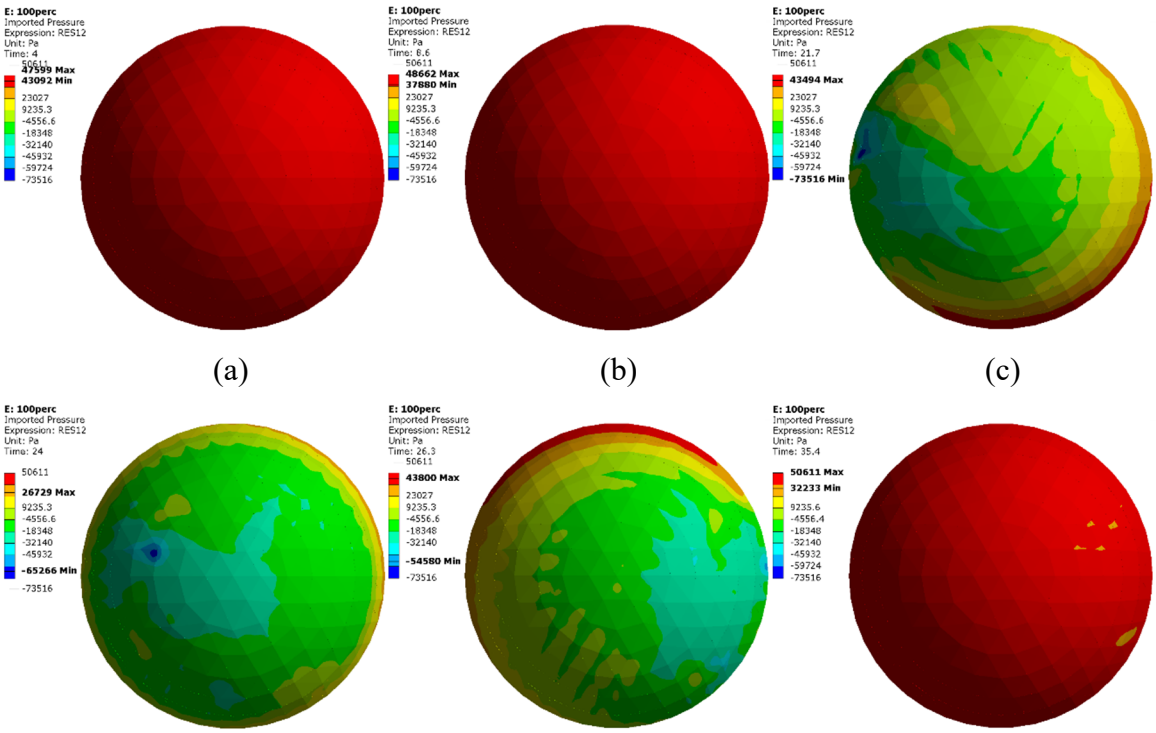

Figure 20. Surface pressure for the single-celled tornado (Case 4): (a) 4 s (300 m away from tornado center); (b) 8.6 s (231 m away from tornado center); (c) 21.7 s (34.5 m away from tornado center); (d) 24 s (0 m away from tornado center); (e) 26.3 s (-34.5 m away from tornado center); (f) 35.4 s (-171 m away from tornado center).

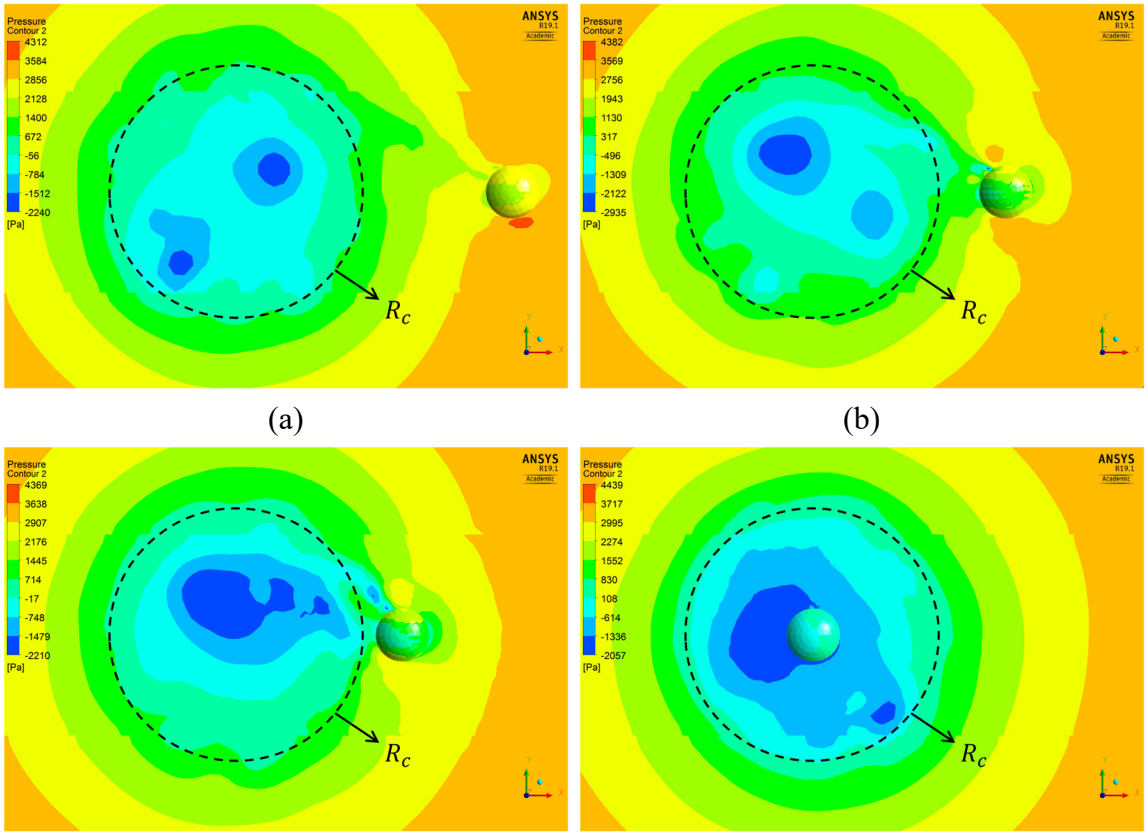

Figure 21. Instantaneous contour plot of static pressure on a 12.5-m-high horizontal plane of the wind field and on the dome surface induced by the double-celled tornado (Case 3) (Note: R_c= 138 m at the elevation of 12.5 m at 300 s; the static pressure contour of the dome surface is superimposed on that of the horizontal plane): (a) Dome center is 300 m away from tornado center; (b) Dome center is 210 m away from tornado center; (c) Dome center is 180 m away from tornado center; (d) Dome center is at tornado center.

To characterize the dynamic characteristics of the surface pressure, the time history of surface pressure at a representative location of the dome (the dome apex) is extracted from these two cases, and the Fourier transform (FT) and the short-time Fourier transform (STFT) of the time histories are carried out, as shown in Figures 23-24. From Figures 23(a) and 24(a), the surface pressure is positive when the dome is far away from the tornado center, and it then decreases and becomes negative when the dome approaches the tornado center, which is due to the large atmospheric pressure drop at the

tornado center (Figure 18). Figures 23(b) and 24(b) show that FT of the surface pressure time histories and the frequency components lower than 0.15 Hz dominate the spectrum, which are relatively low. To obtain the frequency variation over time, Figures 23(c) and 24(c) present STFT of the surface pressure time histories. From the time-frequency scalogram, the surface pressure varies more rapidly when the dome center moves into the tornado core, especially around R_c, which can be indicated by the presence of the higher frequency components at R_c (up to 3.75 Hz for the double-celled tornado and 2.5 Hz for the single-celled tornado). Overall, the dominant frequency components of the surface pressure are below 0.5 Hz over the entire duration.

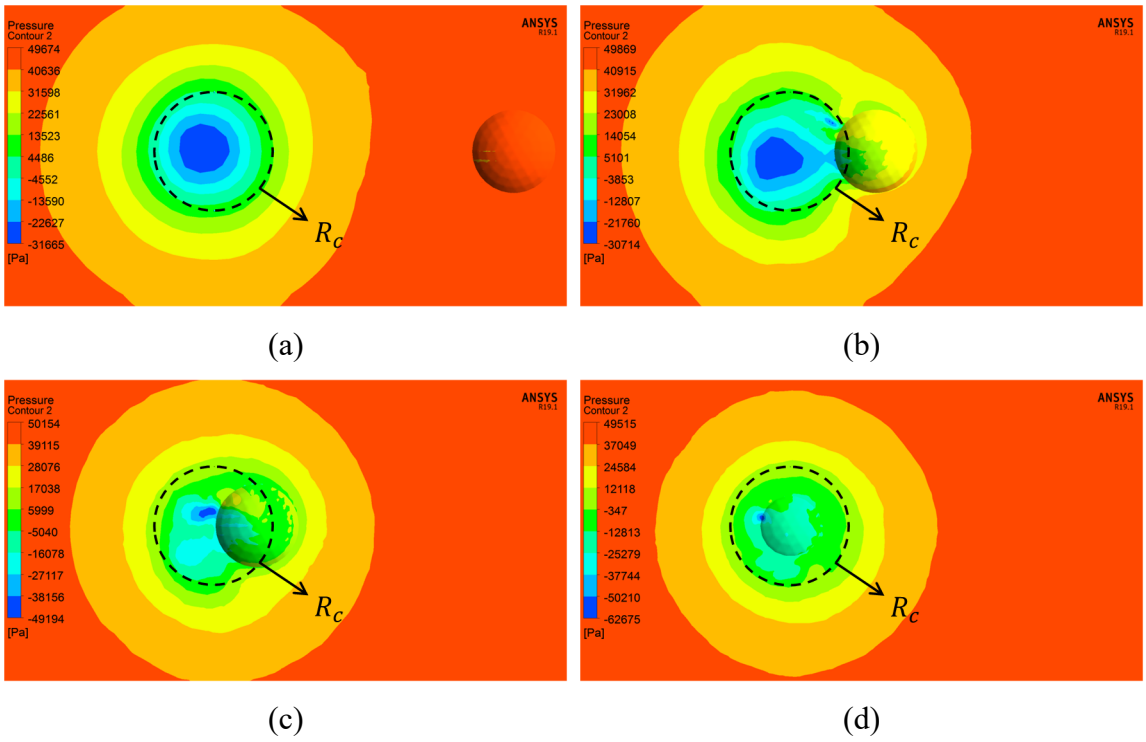

Figure 22. Instantaneous contour plot of static pressure on a 12.5-m-high horizontal plane (except as otherwise specified) of the wind field and on the dome surface induced by the single-celled tornado (Case 4) (Note: R_c= 41.5 m at the elevation of 12.5 m at 300 s): (a) 210 m away from tornado center; (b) 60 m away from tornado center; (c) 30 m away from tornado center; (d) At tornado center at the elevation of 19 m.

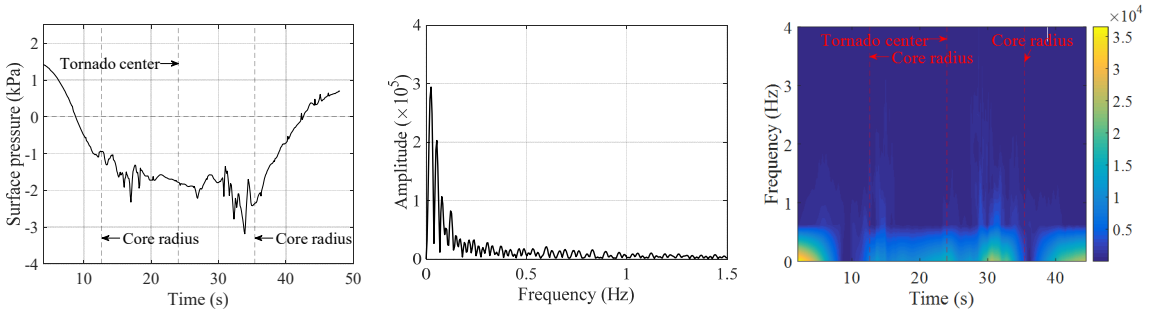

(a) (b) (c)

Figure 23. Time history of the surface pressure at the dome apex induced by the double-celled tornado (Case 3): (a) Time history; (b) Fourier transform; (c) Short-time Fourier transform.

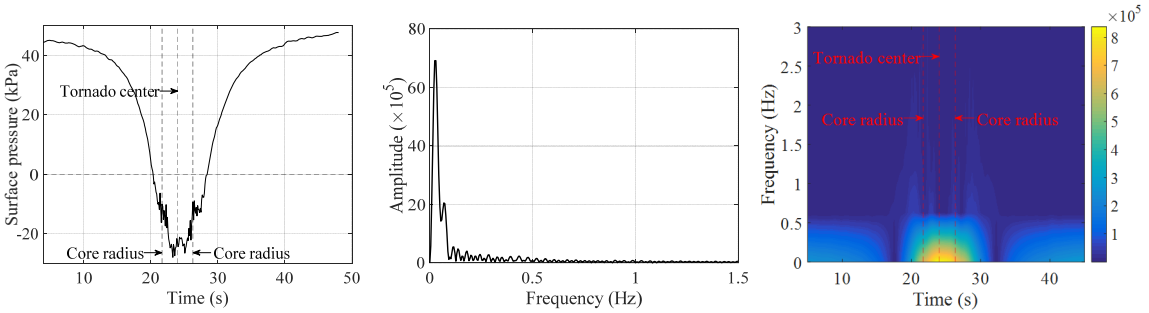

(a) (b) (c)

Figure 24. Time history of the surface pressure at the dome apex induced by the single-celled tornado (Case 4): (a) Time history; (b) Fourier transform; (c) Short-time Fourier transform.

5.2. FORCE AND MOMENT COEFFICIENTS

The wind force and moment are used to quantify the total wind effects of the tornado on the entire dome structure, which are determined by integrating the surface pressure. Forces and moments of both cases are presented in Figures 25 and 27, respectively. The associated force and moment coefficients are calculated based on Equations (6)-(7) and presented in Figures 26 and 28.

$$C_{F_i} = \frac{F_i}{\frac{1}{2}\rho V_{t,max}^2 A} \quad (6)$$

$$C_{M_i} = \frac{M_i}{\frac{1}{2}\rho V_{t,max}^2 AH} \quad (7)$$

where F_i and M_i are the force and moment applied on the dome structure in the i $(x, y \; or \; z)$ direction, respectively; ρ is the density of air (1.225 kg/m^3); A is the projected area of the dome structure on a plane normal to the translating direction (1355 m^2); H is the height of the dome structure (25 m); in each case, the reference velocity is taken as the maximum V_t at the elevation of 25 m in its own wind field, expressed as $V_{t,max}$ (73 m/s for the double-celled tornado and 176 m/s for the single-celled tornado, see Figure 11(b)).

From Figure 25, when the tornado translates over the dome, the suction force (F_z) is the most significant among the three forces for both cases. This is why the roof is often seen to be torn off during tornado incidents. F_z first increases and reaches its maximum value at the tornado center, and then decreases. The magnitude of F_z of the single-celled tornado is much larger than that of the double-celled tornado.

For the single-celled tornado, F_x reaches its peak values when the dome moves to tornado R_c. F_x changes its direction approximately when the dome center passes the tornado center. Since this direction change of the wind force happens very quickly in tornadic wind fields (at the tornado center), within the range of a couple of seconds, it may cause dynamic responses of the structure. It is the same case for F_y induced by the single-celled tornado. However, for the double-celled tornado, the magnitudes of F_x and F_y are much smaller than F_z, and their developments with time are more fluctuating. This is due to the scattered distribution of static pressure (Figure 17(a)) within the larger

tornado core of the double-celled tornado. The findings about the force induced by the single-celled tornado are consistent with laboratory tornado simulations conducted by Haan et al. [31] and Hu et al. [32].

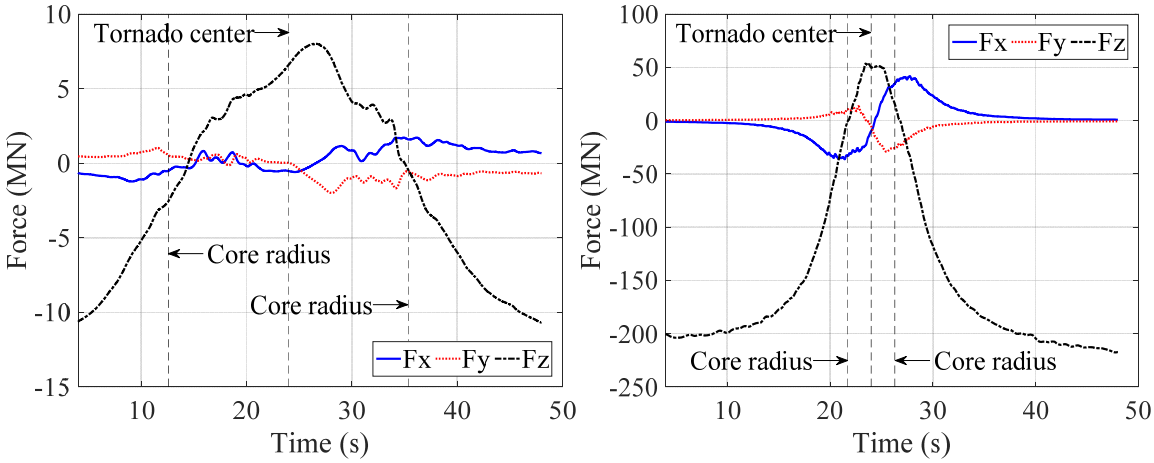

Figure 25. Forces acting on the dome structure: (a) Case 3; (b) Case 4.

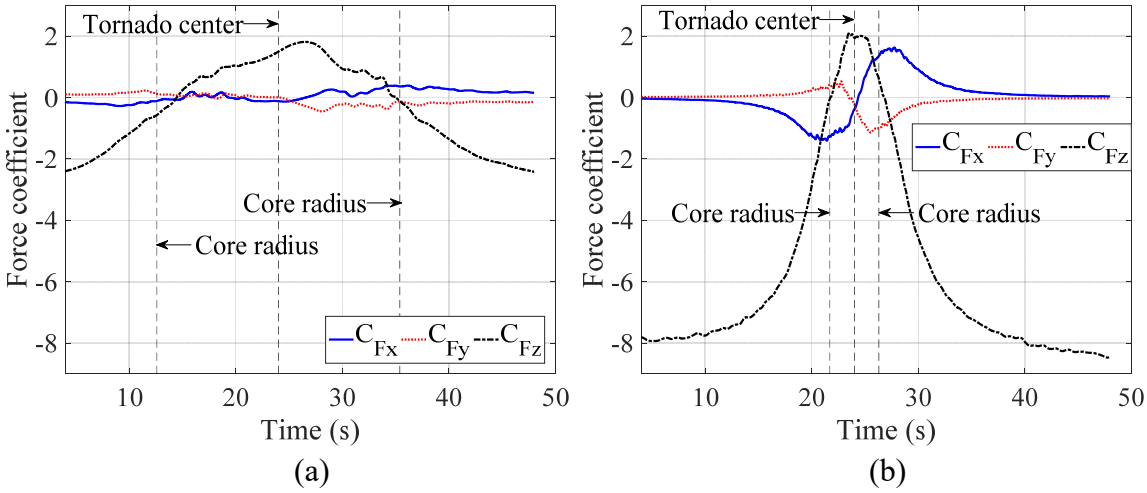

Figure 26. Force coefficients: (a) Case 3; (b) Case 4.

Figure 27 presents the moments acting on the entire dome structure for Cases 3 and 4. For both cases, the rotational moment (M_z) about the Z axis is very small, this is

due to the fact that the geometry of the dome structure is symmetric and that the distribution of surface pressure is approximately symmetric, e.g., the surface pressure is symmetric about the X axis in Figure 19(c). From Figures 27-28, the development of moments induced by the double-celled tornado is more fluctuating than that induced by the single-celled tornado. The moments (Figure 27) induced by the double-celled tornado are much smaller than those induced by the single-celled tornado. It is the same case for the moment coefficients (Figure 28). For the single-celled tornado, the moment about the Y axis (M_y) is much greater than those about the other two axes, and it reaches its peak values when the dome center is about at the edge of R_c. This is because F_x is much greater. That is to say, the effect of the tornado sucking the dome towards its center is much stronger. The trends of the moments induced by the single-celled tornado are consistent with those obtained from laboratory tornado simulations conducted by Haan et al. [31] and Hu et al. [32]. This suggests that the wind loading induced by the double-celled tornado is more dynamic than that induced by the single-celled tornado.

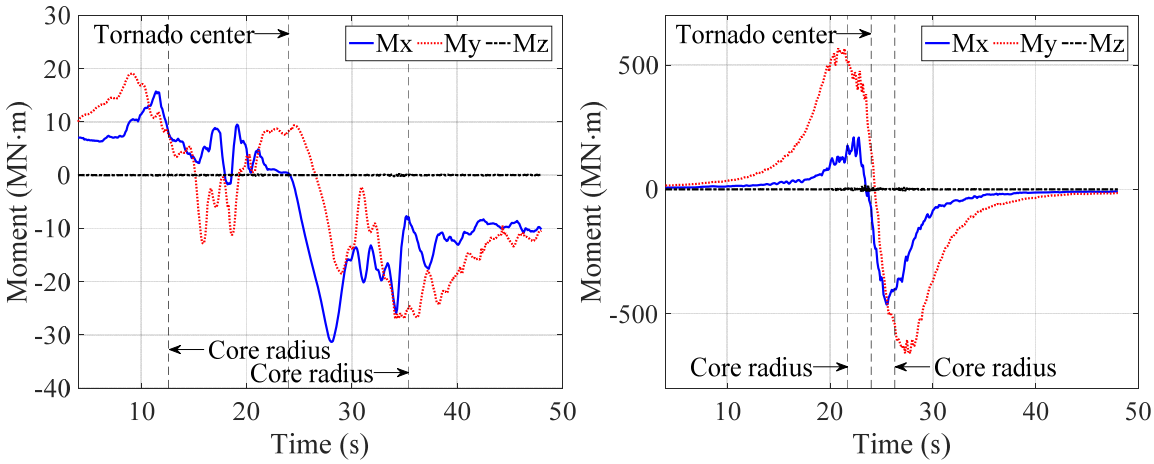

Figure 27. Moments acting on the dome structure: (a) Case 3; (b) Case 4.

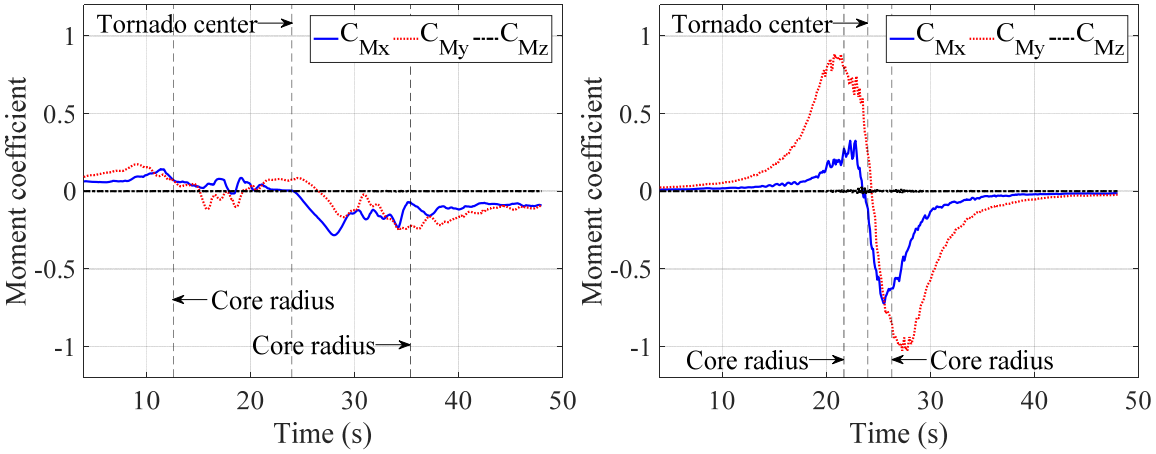

Figure 28. Moment coefficients: (a) Case 3; (b) Case 4.

6. CONCLUSIONS

In this study, the differences between single- and double-celled tornadoes have been systematically investigated using CFD simulations, in respect to both the wind characteristics of tornadic wind fields and the induced wind effects on civil structures. The following conclusions can be drawn:

- The tangential velocity profile and the flow structure on the vertical plane extracted from the simulated tornadic wind field agree well with those extracted from the radar-measured data during Spencer Tornado, which demonstrates the appropriate setup for the CFD simulations.
- A double-celled tornado is formed with a high swirl ratio, while a single-celled tornado is formed with a low swirl ratio; a touching-down downdraft is observed in the central region of the double-celled tornado, while no downdraft is observed in the single-celled tornado; the core radius of the

single-celled tornado is much smaller compared to that of the double-celled tornado while its maximum tangential velocity is much larger, when the velocity input at the velocity inlet is the same; the pressure profile of the single-celled tornado have a narrow, single peak with a higher pressure gradient, but the corresponding profile for the double-celled tornado has a wide, flat distribution.

- Due to the central downdraft, the turbulence intensity of the double-celled tornado is much higher than that of the single-celled tornado in the core region, to be specific, in the region within half of the core radius. Also, the turbulence intensity of the axial velocity is the most significant among all the three velocity components.
- The force and moment induced by the double-celled tornado is more fluctuating and random than those induced by the single-celled tornado, which is caused by the presence of the central downdraft. This suggests that the wind loading induced by the double-celled tornado is more dynamic than that induced by the single-celled tornado.
- The two drag forces (F_x and F_y) under the single-celled tornado follow a typical trend: 1) they reach their peak values when the dome center moves to the tornado core radius; 2) they change their direction approximately when the dome center passes the tornado center; and 3) F_x is much greater than F_y, indicating that the effect of the tornado sucking the dome towards its center is much stronger. However, the corresponding variations under the double-celled tornado tend to be more random, and the effect of sucking the civil structure

towards the tornado center is not obvious. Similar observations can be found from the two overturning moments (M_x and M_y).

ACKNOWLEDGEMENTS

This work was supported by National Science Foundation, the Hazard Mitigation and Structural Engineering program, through the project of "Damage and Instability Detection of Civil Large-scale Space Structures under Operational and Multi-hazard Environments" [award number 1455709]. The authors also want to thank Mr. Jianxun Zhao, a Ph.D. student in the Department of Mechanical Engineering, for his valuable input on efficient CFD simulation setup.

REFERENCES

Fujita, T.T. (1976), "Recent concept of tornado winds", Proceedings of the 2nd USA–Japan Research Seminar on Wind Effects on Structures, University of Tokyo, Tokyo, Japan.

Simmons, K.M. and Sutter, D. (2005), "WSR-88D radar, Tornado warnings, and tornado casualties", Weather and Forecasting, 20(3), 301-310.

Rankine, W.J.M. (1858), "Manual of applied mechanics", C. Griffen Co., London, England.

Deppermann, C.E. (1947), "Notes on the origin and structure of Philippine typhoons", Bulletin of the American Meteorological Society, 28, 399-404.

Burgers, J.M. (1948), "A mathematical model illustrating the theory of turbulence", Advances in Applied Mechanics, 1, 171-199.

Rott, N. (1958), "On the viscous core of a line vortex", Zeitschrift für angewandte Mathematik und Physik ZAMP, 9(5-6), 543-553.

Sullivan, R. (1959), “A Two-cell Vortex Solution of the Navier-Stokes Equations”, Journal of Aerospace Sciences, 26, 767-768.

Vatistas, G.H. (1998), “New Model for Intense Self-Similar Vortices”, Journal of Propulsion and Power, 14(4), 462-469.

Wood V.T. and Brown R.A. (2011), “Simulated tornadic vortex signatures of tornado-like vortices having one-and two-celled structures”, Journal of Applied Meteorology and Climatology, 50(11), 2338-42.

Manikis, F.I. (2015), “New solutions for two-cell vortices”, Thesis, Concordia University, Montreal, Quebec, Canada.

Ward, N.B. (1972), “The exploration of certain features of tornado dynamics using a laboratory model”, Journal of the Atmospheric Sciences, 29(6), 1194-1204.

Church, C.R., Snow, J.T. and Agee, E.M. (1977), “Tornado vortex simulation at Purdue University”, Bulletin of the American Meteorological Society, 58(9), 900-908.

Church, C.R., Snow, J.T., Baker, G.L. and Agee, E.M. (1979), “Characteristics of tornado-like vortices as a function of swirl ratio: A laboratory investigation”, Journal of the Atmospheric Sciences, 36(9), 1755-1776.

Diamond, C.J. and Wilkins, E.M. (1984), “Translation effects on simulated tornadoes”, Journal of the atmospheric sciences, 41(17), 2574-2580.

Leslie, F.W. (1977), “Surface roughness effects on suction vortex formation: A laboratory simulation”, Journal of the Atmospheric Sciences, 34(7), 1022-1027.

Tari, P.H., Gurka, R. and Hangan, H. (2010), “Experimental investigation of tornado-like vortex dynamics with swirl ratio: The mean and turbulent flow fields”, Journal of Wind Engineering and Industrial Aerodynamics, 98(12), 936-944.

Wang, H., James, D., Letchford, C., Peterson R. and Snow, J. (2001), “Development of a Prototype Tornado Simulator for the Assessment of Fluid-Structure Interaction”, Proceedings of the 1st Americas Conference on Wind Engineering, June 4-6, Clemson Uni., SC.

Haan, F.L., Sarkar, P.P. and Gallus, W.A. (2008), “Design, construction and performance of a large tornado simulator for wind engineering applications”, Engineering Structures, 30(4), 1146-1159.

Hangan, H. (2014), “The wind engineering energy and environment (WindEEE) dome at western university, Canada”, Wind Engineers, JAWE, 39(4), 350-351.

Haan, F.L., Sarkar, P.P., Kopp, G.A. and Stedman, D.A. (2017), "Critical wind speeds for tornado-induced vehicle movements", Journal of Wind Engineering and Industrial Aerodynamics, 168, 1-8.

Razavi, A. and Sarkar, P.P. (2018), "Laboratory investigation of the effects of translation on the near-ground tornado flow field", Wind and Structures, 26(3), 179-190.

Razavi, A. and Sarkar, P.P. (2018), "Laboratory study of topographic effects on the near-surface tornado flow field", Boundary-Layer Meteorology, 1-24.

Refan, M., Hangan, H. and Wurman, J. (2014), "Reproducing tornados in laboratory using proper scaling", Journal of Wind Engineering and Industrial Aerodynamics. 135, 136-148.

Tang, Z., Zuo, D., James, D., Eguchi, Y. and Hattori, Y. (2018), "Effects of aspect ratio on laboratory simulation of tornado-like vortices", Wind and Structures, 27(2), 111-121.

Tang, Z., Feng, C., Wu, L., Zuo, D. and James, D.L. (2018), "Characteristics of tornado-like vortices simulated in a large-scale Ward-type simulator", Boundary-Layer Meteorology, 166(2), 327-350.

Ishihara, T., Oh, S. and Tokuyama, Y. (2011), "Numerical study on flow fields of tornado-like vortices using the LES turbulence model", Journal of Wind Engineering and Industrial Aerodynamics, 99(4), 239-248.

Ishihara, T. and Liu, Z. (2014), "Numerical study on dynamics of a tornado-like vortex with touching down by using the LES turbulent model," Wind and Structures, 19(1), 89-111.

Kuai, L., Haan, F.L., Gallus, W.A. and Sarkar, P.P. (2008), "CFD simulations of the flow field of a laboratory-simulated tornado for parameter sensitivity studies and comparison with field measurements", Wind and Structures, 11(2), 75-96.

Natarajan, D. (2011), "Numerical simulation of tornado-like vortices", Ph.D. Dissertation, the University of Western Ontario, London, Ontario, Canada.

Yuan, F., Yan, G., Honerkamp, R. and Isaac, K.M. (2017), "Numerical Simulation of Laboratory Tornado Simulator that can Produce Translating Tornadoes", Journal of Wind Engineering and Industrial Aerodynamics. Under review.

Haan, F.L., Balaramudu, V. K. and Sarkar, P.P. (2009), "Tornado-induced wind loads on a low-rise building", Journal of Structural Engineering, 136(1), 106-116.

Hu, H., Yang, Z., Sarkar, P. and Haan, F. (2011), "Characterization of the wind loads and flow fields around a gable-roof building model in tornado-like winds", Experiments in Fluids, 51(3), 835-851.

Mishra, A.R., James, D.L. and Letchford, C.W. (2008), "Physical simulation of a single-celled tornado-like vortex, Part B: Wind loading on a cubical model", Journal of Wind Engineering and Industrial Aerodynamics, 96(8), 1258-1273.

Natarajan, D. and Hangan, H. (2012), "Large eddy simulations of translation and surface roughness effects on tornado-like vortices", Journal of Wind Engineering and Industrial Aerodynamics, 104, 577-584.

Rajasekharan, S.G., Matsui, M. and Tamura, Y. (2013), "Characteristics of internal pressures and net local roof wind forces on a building exposed to a tornado-like vortex", Journal of Wind Engineering and Industrial Aerodynamics, 112, 52-57.

Selvam, R.P. and Millett, P.C. (2003), "Computer modeling of tornado forces on a cubic building using large eddy simulation," J. Ark. Acad. Sci, 57, 140-146.

Feng, C. and Chen, X. (2018), "Characterization of translating tornado-induced pressures and responses of a low-rise building frame based on measurement data", Engineering Structures, 174, 495-508.

Sengupta, A., Haan, F. L., Sarkar, P. P. and Balaramudu, V. (2008), "Transient loads on buildings in microburst and tornado winds", Journal of Wind Engineering and Industrial Aerodynamics, 96(10), 2173-2187.

Selvam, R.P. and Millett, P.C. (2005), "Large eddy simulation of the tornado-structure interaction to determine structural loadings", Wind and Structures, 8(1), 49-60.

Razavi, A. and Sarkar, P.P. (2018c), "Tornado-induced wind loads on a low-rise building: Influence of swirl ratio, translation speed and building parameters", Engineering Structures, 167, 1-12.

Kosiba, K. and Wurman, J. (2010), "The three-dimensional axisymmetric wind field structure of the Spencer, South Dakota, 1998 tornado", Journal of the Atmospheric Sciences, 67(9), 3074-3083.

Refan, M., Hangan, H., Wurman, J. and Kosiba, K. (2017). "Doppler radar-derived wind field of five tornado events with application to engineering simulations", Engineering Structures, 148, 509-521.

Li, T., Yan, G., Yuan, F. and Chen, G. (2018), "Dynamic structural responses of long-span dome structures induced by tornadoes", Journal of Wind Engineering and Industrial Aerodynamics (under review).

Pointwise. (2018), V18.0 Release 3, Pointwise, Inc., Fort Worth, TX, USA.

Wurman, J. and Alexander, C.R. (2005), "The 30 May 1998 Spencer, South Dakota, storm. Part II: Comparison of observed damage and radar-derived winds in the tornadoes", Monthly weather review, 133(1), 97-119.

Refan, M. (2014), "Physical Simulation of Tornado-Like Vortices", Ph.D. Thesis, the University of Western Ontario, London, Ontario, Canada.

Hangan, H. and Kim, J.D. (2008), "Swirl ratio effects on tornado vortices in relation to the Fujita scale", Wind and Structures, 11(4), 291-302.

Davies-Jones, R., Trapp, R.J. and Bluestein, H.B. (2001), "Tornadoes and tornadic storms", Proceedings of Severe convective storms. American Meteorological Society, Boston, MA, 167-221.

Fiedler, B.H. and Rotunno, R. (1986), "A theory for the maximum wind speeds in tornado-like vortices", Journal of the Atmospheric Sciences, 43(21), 2328-2340.

Tamura, Y. and Kareem, A. ed. (2015), Advanced Structural Wind Engineering, Springer, Japan.

Snow, J.T., Church, C.R. and Barnhart, B.J. (1980), "An investigation of the surface pressure fields beneath simulated tornado cyclones", Journal of the Atmospheric Sciences, 37(5), 1013-1026.

III. DYNAMIC STRUCTURAL RESPONSES OF LONG-SPAN DOME STRUCTURES INDUCED BY TORNADOES

Tiantian Li, Guirong Yan, Fangping Yuan and Genda Chen

ABSTRACT

Long-span dome structures are widely used for public assembly venues because of their large column-free space and efficient use of materials. When occupied by hundreds or even thousands of people, it would be devastating if they fail or collapse, which unfortunately happen frequently during extreme events, especially under tornadic winds. Although static effects of tornadoes on civil structures have been extensively studied, their dynamic impact has not been sufficiently investigated. In this study, non-stationary characteristics of tornadoes and their dynamic impact on a long-span dome structure are systematically investigated. In particular, the time-variant wind pressure on the dome surface induced by translating tornadoes with different intensities is characterized through Computational Fluid Dynamics simulations. The obtained wind pressure on the dome surface is then mapped onto the finite element model of the dome structure, and transient time-history analyses are conducted to characterize the tornado-induced dynamic responses. It is observed that non-stationary wind pressure and the induced dynamic structural responses are significant, when core radius of the tornado approaches the dome. Wind flow of EF4 and EF5 tornadoes is found to be more turbulent than EF2 and EF3 tornadoes, and hence larger and more rapid fluctuations of dynamic responses.

1. INTRODUCTION

A tornado is a rotating column of air extending from a cumulonimbus cloud to the ground. It is claimed to be one of the most violent natural hazards. They result in incredible amounts of property damage and significant numbers of fatalities each year. The devastation from recent tornadoes (e.g., the Joplin, MO tornado of May 22, 2011; the Tuscaloosa, AL tornado of April 27, 2011; and the Moore, OK tornado of May 20, 2013) left no doubt as to the vulnerability of the central United States to tornadoes and prompted an urgent need in studying tornadoes in all aspects from different research fields.

To investigate flow characteristics of tornado vortices, tornadic wind flow has been modeled using analytical modeling, experimental simulation, and numerical simulation. Several simplified analytical models have been developed. Rankine vortex model, a simple one-dimensional analytical model, only used tangential velocity to represent the flow; more advanced analytical models, e.g. modified Rankin vortex (Deppermann, 1947) and Burgers-Rott vortex (Burgers, 1948; Rott, 1958), were developed later to better capture the characteristics of tornadoes. Based on the laboratory simulations conducted through Ward-type tornado simulator (Ward, 1972) and its updated ones (Church et al., 1977; Leslie, 1977; Church et al., 1979; Diamond and Wilkins, 1984; Wang et al., 2001; Tari et al., 2010), it was found that the tornadic wind flow characteristics and vortex configurations were governed by the following three non-dimensional parameters, swirl ratio, radial Reynolds number and aspect ratio. The recently developed laboratory tornado simulators in North America are located at Iowa

State University (Haan et al., 2008), Texas Tech University (Mishra et al., 2008a) and Western University (Hangan, 2014). Tests were conducted through these facilities to characterize the generated wind flow (Refan et al., 2014; Haan et al., 2017; Razavi and Sarkar, 2018a, 2018b; Tang et al., 2018a, 2018b), among which Refan et al. (2014) investigated the relationship between the swirl ratio and the velocity-based EF-scale so that the simulated and real tornadoes can be correlated. It was concluded that EF0-EF3 tornadoes in nature can be represented by the tornado vortices generated in the facility at Western University using proper scaling. Numerical simulations of tornadic wind flow have been mainly focused on the tornado vortices generated in laboratory tornado simulators. Ward-type laboratory tornado simulator, tornado simulators at Iowa State University and Western University, and the Atmospheric Vortex Engine were modeled by Computational Fluid Dynamics (CFD) simulations and the air flow through these tornado simulators was investigated (Kuai et al., 2008; Ishihara et al., 2011; Natarajan, 2011; Yuan et al., 2017). Three-dimensional numerical simulations of tornado-like vortices were performed by Hangan and Kim (2008) and compared with the full-scale radar data from the Spencer, SD tornado of May 30, 1998, and it was concluded that the results of swirl ratio of 2 compared well with the full-scale data.

The above research efforts were aimed at comprehensive understanding of the tornado vortex itself, which also built a solid foundation for examination of tornado-induced wind loads on civil structures. Extensive studies have been reported with respect to tornado-induced wind loads (Haan et al., 2008; Haan et al., 2010; Hu et al., 2011; Ishihara et al., 2011; Kuai et al., 2008; Mishra et al., 2008a, 2008b; Natarajan and Hangan, 2012; Rajasekharan et al., 2013; Sabareesh et al., 2013), together with the static

impact of tornadoes (mean aerodynamic loading) on civil structures (Selvam and Millett, 2003). However, the research on the non-stationary characteristics of tornadoes and their dynamic impact on civil structures has been lacking. The recent anemometer-measured wind speeds inside a tornado demonstrated the non-stationary characteristics of tornadoes (Wurman et al., 2013), resulting in a dynamic effect on civil structures. The dynamic effect can cause a structure to oscillate severely, as observed on the Great Plains Life building during the Lubbock, TX tornado of May 11, 1970 (Chang, 1971). Chang suggested that structures should be designed for non-stationary wind loads, which may vary from 20% to 70% more than the mean wind pressure (Chang, 1966). Tornado-induced wind loads applied on a tall building was studied with an analytical model of tornado (Wen, 1975). In this model, the velocity profiles of three components (tangential, radial, and vertical) were defined as a function of radial distance within and above the boundary layer of the tornado. It was found that very large inertial forces in the tangential and radial directions were produced by the tornadic winds, which indicated the velocity change in the tornado vortex boundary layer and the large pressure gradient. It was concluded that the inertial forces should be considered in structural analysis. Otherwise the wind-induced structural responses would be underestimated. Transient wind loads on a cubic building under a translating tornado was simulated in a laboratory simulator (Sengupta et al., 2008). In their study, tornadoes with two different tornado vortex radii and two different tornado translation speeds were simulated. Measured transient wind loads were compared to the stationary case where the tornado vortex does not translate. It was found that the wind loads on the cubic building induced by tornadoes of F2 or higher intensity are 50% more than that induced by the associated stationary case. In addition,

wind loads on a cubic building induced by a translating tornado were investigated through CFD simulations (Selvam and Millett, 2005). Turbulence was modeled using large eddy simulation. From the numerical results, 45% more forces on the walls and 100% more forces on the roof were caused by the translating tornado than straight-line winds. The magnitude and direction of these forces change quickly when the tornado core was in the vicinity of the building. Strasser et al. (2016) proposed the concept of dynamic load factor to assess the dynamic amplification of tornadic wind loads on civil structures. In that study, two-dimensional loading of a rigid, circular cylinder under an impinging vortex was simulated, and the tangential velocity profile was compared with the tangential velocity profiles extracted from full-scale radar-measured data. It was concluded that potential dynamic load amplification should be considered for flexible structures, since they may experience significant dynamic loading from tornadic wind loads.

Based on the understanding of the non-stationary characteristics of the tornadic wind loads, attempts have been made to investigate dynamic responses on civil structures via structural analyses (Dutta et al., 2002; Ahmad et al., 2014). Planar frame buildings and a pitched portal shed were analyzed under an empirical tornado model. In this empirical model, both radial and vertical velocities were approximated as half of tangential velocity. The finite element (FE) analyses showed that dynamic displacement responses caused by tornadic winds were fifty times the response under the basic wind speed (straight-line winds) as per IS code (IS875 Part 3, 1987); and stiffer or smaller buildings may be affected mostly by a faster tornado, while more flexible or taller ones may be affected mostly by a slower tornado.

Previous research either investigated the wind characteristics of tornadic wind fields or the induced wind effects by CFD simulations, or investigated structural responses using FE analyses. Seldom research has combined these two together. Dr. Elawady and Dr. El Damatty have applied similar approach to investigate tornado and downburst effects on lattice towers and transmission lines, considering potential positions and movements of the downbursts to find the worst loading situation (Elawady et al., 2017; El Damatty and Elawady, 2018; Hamada and El Damatty, 2016). However, they only used CFD simulations to model the tornadoes and downbursts, and loading on civil structures was determined by code neglecting transient aerodynamics. To capture real dynamic responses of civil structures, it is necessary to consider the transient aerodynamics of tornado-induced wind loads on the structures. Therefore, in this study, CFD simulations are not only used to simulate the tornadic wind field, but also used to determine tornado-induced wind loads on civil structures by including the civil structure in the computational domain of the CFD simulation. FE analyses are then combined with CFD simulations for the first time to systematically investigate the tornado-induced dynamic impact on civil structures.

The remainder of this paper is organized as follows. First, a long-span civil structure of interest, a dome structure, will be described. Second, tornadoes with different intensities translating over the dome structure will be modeled using CFD simulations based on a real-world tornado (the Spencer, SD tornado of May 30, 1998), and then the tornado-induced wind pressure on the dome structure will be determined. Third, dynamic characteristics (natural frequencies and mode shapes) of the dome structure itself will be studied through a modal analysis. Finally, the obtained tornado-induced wind pressure

from CFD simulations will be mapped onto the finite element model (FEM) of the dome structure, and dynamic time-history analyses of the structure will be conducted to investigate its dynamic responses.

2. DOME STRUCTURE

Due to their large column-free space and efficient use of materials, long-span dome structures have been widely used for public assembly venues, such as sport stadiums, auditoriums and shopping malls. Since this type of structure is often crowded by hundreds or even thousands of people, their collapse or failure would be devastating. This type of structure is potentially subjected to significant wind loads because of large surface areas. The wind loads on dome structures induced by tornadoes have not been sufficiently explored, except the study conducted by Yousef and Selvam (2016a, 2016b, 2017) and Yousef et al. (2018), which investigated the tornadic wind loads induced by different sizes of tornadoes on the same structure and the influence of the ratio of tangential velocity to translating speed on wind force coefficients, and the previous studies by the present authors (Zhao et al., 2016a; Zhao et al., 2016b; Zu et al., 2016). Thus far, no structural responses of dome structures induced by tornadoes have been studied. To systematically investigate the dynamic structural responses of dome structures under tornadic winds, a Kiewitt-type K6-7 single-layer spherical dome structure (Figure 1) is considered here.

This dome structure spans 75 m (L) and rises 25 m (f). It consists of 462 tubular beam members, which form a frame, and 294 shells, which cover the frame. The diameter

and thickness of the radial and latitudinal beam members are 152 mm and 5 mm, respectively; and those of the diagonal beam members are 140 mm and 4.5 mm, respectively. The thickness of all shells is 15 mm. All beam members and shells are assumed to be made of A36 steel. The density of the A36 steel is $7850\ \mathrm{kg/m^3}$, and its Young's modulus and Poisson's ratio are 200 GPa and 0.3, respectively. The structure is assumed to be fixed at the bottom joints with restraints in all three translational degrees of freedom (DOFs) and all three rotational DOFs.

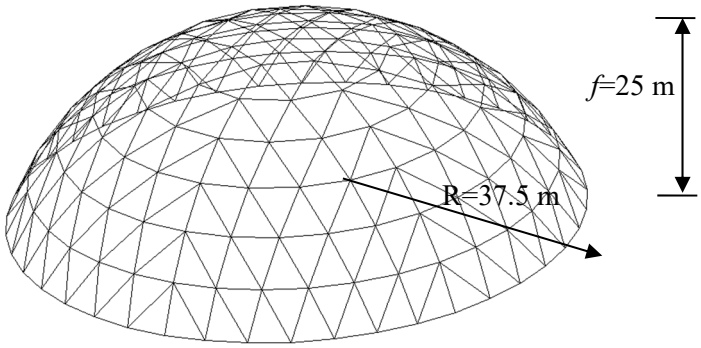

Figure 1. Spherical dome structure.

3. SIMULATION OF TORNADIC WIND FIELD

3.1. TORNADOES SIMULATED IN THIS STUDY

Simulation of the tornadic wind field is based on a real-world F4 tornado, the Spencer, SD tornado of May 30, 1998 (hereafter "Spencer Tornado"). Kosiba and Wurman (2010) reported that the maximum tangential velocity of Spencer Tornado ranges from 60 to 80 m/s, and the core radius fluctuates around 200 m during their 8-min observation period at the elevation of 40 m. The swirl ratio of this tornado exceeds 1.

This tornado will be taken as the baseline and parameters will be adjusted to generate tornadoes with different intensities. The CFD simulation software, ANSYS FLUENT, is employed to simulate the tornadic wind fields.

3.2. COMPUTATIONAL DOMAIN

To simulate the swirling wind flow, a computational domain consisting of two cylinders is applied, as shown in Figure 2. The bottom cylinder is 100 m high and resembles the inflow zone. The top cylinder is 1,000 m high and resembles the convection zone. Thus, the total height of the computational domain is 1,100 m. The radii of the two cylinders are both 800 m. An inflow with tangential and radial velocity components enters the bottom cylindrical domain and exits from the circle on the top surface of the top cylinder. The radius of the top outflow circle is 340 m. The boundary condition on the inflow surface is velocity-inlet and that on the outflow circle is pressure-outlet. The rest top and side boundary surfaces are defined as symmetry. The bottom boundary surface is a no-slip wall when a stationary tornado is simulated and a moving wall when a translating tornado is simulated.

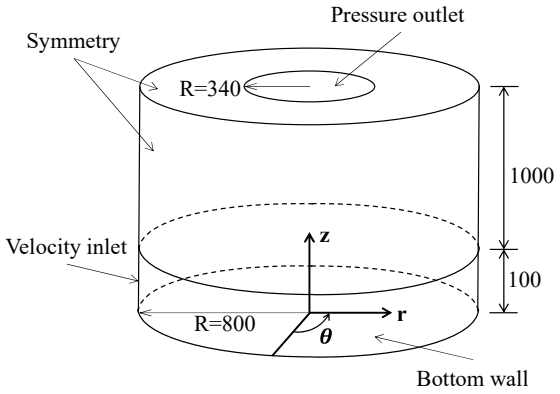

Figure 2. Computational domain of the simulated tornadic wind field (unit: m).

3.3. BOUNDARY CONDITION AT VELOCITY INLET

The radar-measured data only at a location 800 m away from the tornado center through the height of 320 m are used to do data regression to get the tangential velocity profile and radial velocity profile at the velocity inlet. The obtained regression equations of tangential velocity V_t and radial velocity V_r along the height are expressed as

$$V_t = 20.61\left(\frac{z}{20}\right)^{0.1774} \tag{1}$$

$$V_r = \begin{cases} -31.14\left(\frac{z}{20}\right)^{0.169}, & z < 20 \text{ m} \\ 45.14\left(\frac{z}{20}\right)^{0.1826} - 76.48, & z \geq 20 \text{ m} \end{cases} \tag{2}$$

where z is the height above the ground.

The velocity profiles in Equations (1) and (2) are graphed in Figure 3, together with full-scale radar data. It is seen that the radar-measured data are slightly scattered around the regression lines, indicating that the regression lines fit the radar-measured data very well. Therefore, the obtained velocity profiles are used as the input at the velocity inlet.

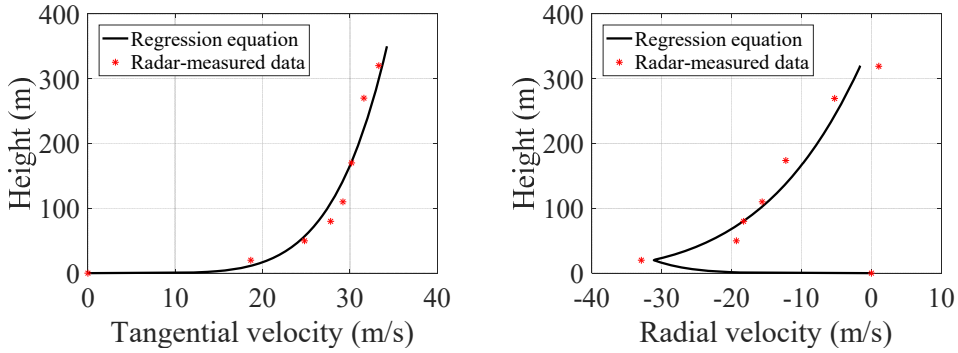

Figure 3. Comparison between regression equation and radar-measured data of velocity profiles: (a) tangential; (b) radial.

3.4. SIMULATED CASES

First, the case where the dome structure is not present is simulated to verify the applied CFD simulation strategies, which is described in Section 4. Then, the dome structure is included in the computational domain to quantify tornadic wind pressure on the dome surface. The obtained wind effects on the dome structure are compared to previous findings (although it is rare), which is described in Section 6. The velocity profiles expressed in Equations (1) and (2) represent EF3 tornado based on Enhanced Fujita scale (McDonald et al., 2010). In order to simulate tornadoes with different intensities, the velocity profiles are scaled by 150%, 130%, and 87% to simulate EF5, EF4 and EF2 tornadoes, respectively.

3.5. SIMULATION OF TORNADO TRANSLATION

Since a real-world tornado always translates, the whole process of a tornado translating over civil structures is simulated. To simulate the translation of a tornado, rather than having the tornado move, the dome structure is made to move in the opposite direction to the direction of tornado translating. As shown in Figure 4, the dome structure is originally located at 360 m on the x axis (t = 0 s). It translates along the negative X direction at a speed of 15 m/s, which is the translating speed of Spencer Tornado based on the field measurement data (Wurman and Alexander, 2005). When t = 24 s, it reaches the tornado center. The calculation terminates when the dome structure moves to -360 m on the x axis (t = 48 s). In the CFD simulation, the dynamic mesh technique is applied to simulate that the dome structure travels inside the computational domain. Besides, to simulate the relative motion between the ground plane and the tornado, a moving wall

boundary condition is applied on the ground plane with the speed of 15 m/s in the negative X direction.

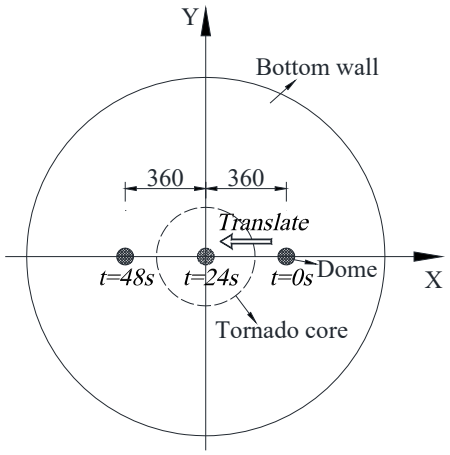

Figure 4. Schematic diagram of the simulation of tornado translation (unit: m).

3.6. MESH STRATEGY AND DYNAMIC MESH ZONES

Pointwise is chosen for preprocessing of the geometric model of the computational domain. Hybrid meshes including hexahedra, tetrahedra, pyramids and prisms are generated. The grids of the *x*-*z* plane where *y*=0 is shown in Figure 5(a). For the near-ground wind field (the bottom cylinder in Figure 5(a)), fine mesh is applied, i.e., the longest edge of all cells is 9 m. For higher levels (the top cylinder in Figure 5(a)), coarse mesh is applied, i.e., the longest edge of all cells is 34 m. By combining fine and coarse mesh, accurate solution and computational efficiency can be achieved at the same time. Similar strategy has been employed by Gallus et al. (2006).

Inflation grid sizing is applied to the ground surface and the dome surface. Since the variations in the wind profile near the ground (boundary layer) need to be accurately captured, a higher number of cells in the direction normal to the wall are necessary.

Therefore, cells with high aspect ratios are stacked in the direction normal to the wall, that is, the inflation technique. More details about the mesh arrangement are described as below.

The cuboid that contains the dome structure is meshed into unstructured tetrahedral grids, as shown in Figure 5(b). The remaining zones are meshed into structured hexahedral grids. Regarding the inflation grid sizing on the ground and dome surfaces, the height of the first layer is 0.002 m (the aspect ratio is 9/0.002=4,500) and the corresponding Y+ value is 250 using the flat-plate boundary layer theory. The growth rate is 1.2 and a total of 36 layers is used. A plan view of the meshed top cylinder is shown in Figure 5(c). To create structured grids for the top cylinder, a smooth structured O-H topology (Pointwise, 2016) with the floating boundary condition in the grid solver is used. Figure 5(d) shows the layout of the pressure outlet (inner circle) in order to use O-H topology. Figure 5(e) presents a plan view of the meshed bottom cylinder at the elevation of 25 m. The truncated semicircle is split into four regions in order to create structured grids (Figure 5(f)). It is worth mentioning that the split point should be outside the path of the tornado translation in order to avoid potential numerical errors caused by the dynamic mesh.

During the translating motion, the cuboid that contains the dome structure moves as a rigid body at the speed of 15 m/s in the negative X direction. The top cylinder is defined as stationary. Also, the two truncated semi-cylinders of the bottom cylinder are defined as stationary. The remaining parts of the bottom cylinder excluding the cuboid that contains the dome are defined as dynamic mesh zones (Figure 5(f)), in which the layering technique is applied.

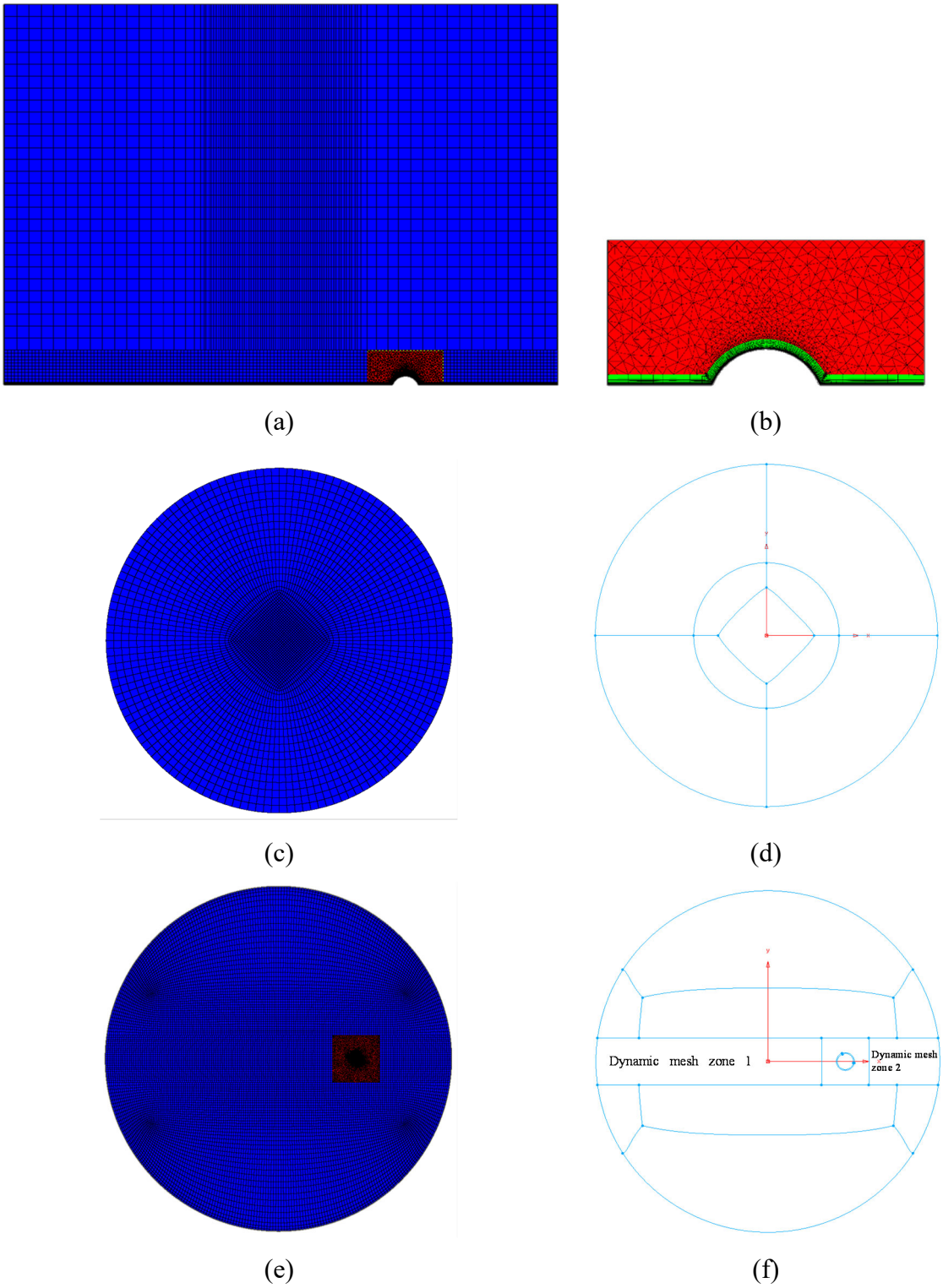

Figure 5. Hybrid meshes of the computational domain: (a) x-z plane where y=0; (b) cuboid that contains the dome structure; (c) plan view of the meshed top cylinder; (d) layout of the top cylinder before mesh; (e) plan view of the meshed bottom cylinder; (f) layout of the bottom cylinder before mesh.

3.7. SIMULATION SETUP

The large eddy simulation (LES) with a Smagorinsky-Lilly subgrid-scale model is adopted for turbulence modeling, and thus filtered time-dependent Navier-Stokes equations are the governing equations of the tornadic wind flow. LES is a time-dependent approach, and it can provide detailed information about the wind flow. The governing equations are solved by the segregated implicit solver with the SIMPLEC (Semi-Implicit Method for Pressure Linked Equation-Consistent) method.

The simulation is first run for 300 s for the stationary case when the dome structure is not moving; and then it is run for another 48 s for the translating case when the dome structure is moving. The time step of the simulation is 0.01 s. During the translating motion, the dynamic mesh is turned on. The double-precision solver is chosen due to the following three reasons: 1) the aspect ratio of the cell is large, especially in the inflation layers; 2) pressure level varies greatly in certain locations, such as the large atmospheric pressure drop at the tornado center; 3) the adoption of the dynamic mesh achieving the tornado translation.

The main computational resource is a research platform with 2 processors (Intel(R) Xeon(R) CPU E5-2699 v3 @ 2.30 GHz, 18 cores per processor) and 192 GB RAM. The high performance computing, the Forge that is operated by the authors' university, is used as a secondary computational resource. It includes 4 compute nodes with each node containing dual 16 core Haswell CPUs with 256 GB RAM. In general, 10-15 days are needed to finish one simulation, depending on different intensities of the tornado and the number of parallel simulations running on the same machine at the same time.

4. VERIFICATION OF THE APPLIED CFD SIMULATION STRATEGIES FOR EF3 TORNADO

In order to verify the applied CFD simulation strategies, the numerical model when the dome structure is not present is first calculated. Since the velocity input for the simulated EF3 tornado is directly obtained from Spencer Tornado, only numerical results from this tornado intensity are compared to radar-measured data during Spencer Tornado.

Figure 6 presents V_t profile of the simulated cases (EF2-EF5 tornadoes) as a function of radial distance at the elevation of 80 m. The radial distance of 0 m indicates the tornado center. The core radius is defined as the location where the maximum V_t is reached. From Figure 6, the core radii of the simulated EF2-EF5 tornadoes are 223m, 232 m, 244 m, and 218 m, respectively, and the corresponding maximum V_t are 59 m/s, 64 m/s, 82 m/s, and 104 m/s, respectively. The V_t profile at the elevation of 80 m extracted from the Radar-measured data (Gallus et al., 2004) is also included in Figure 6 for comparison. The simulated EF3 tornado is in general agreement with the radar-measured data with the error of 5.5% for core radius and of 1.3% for tangential velocity.

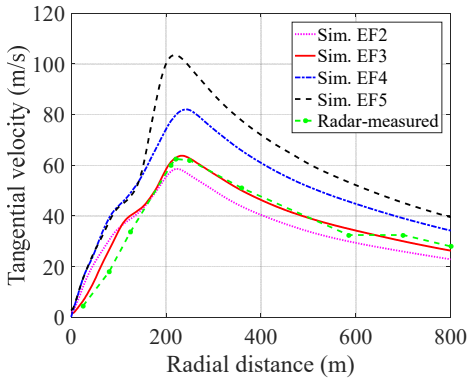

Figure 6. Comparison of numerically-simulated and radar-measured tangential velocity profile as a function of radial distance.

The axial, radial, and tangential velocity profiles as a function of height at the radius of 300 m are shown in Figure 7. In general, axial, radial, and tangential velocities increase with the increase of tornado intensity, and tangential velocity is the largest in magnitude. From Figure 7(a), the maximum axial velocity is located at 200-250 m. Above 500 m, axial velocity is close to zero for all cases. In Figure 7(b), negative radial velocity represents inflow. The strongest inflow is located near the ground, which is consistent with the numerical studies by Lewellen et al. (1997) and the experimental studies by Refan and Hangan (2018), as well as radar-measured data by Gallus et al. (2004). With the increase of the height, the inflow weakens and the flow direction changes to an outflow. For the elevations above 450m, the flow changes back to an inflow and the magnitude is much smaller. For EF3 tornado, the depth of the inflow layer is around 120 m, which is very close to the radar-measured data. This demonstrates the appropriate setup for the height of velocity inlet of the tornadic computational domain. From Figure 7(c), the maximum tangential velocity is located between 100 m and 150 m for all simulated tornadoes.

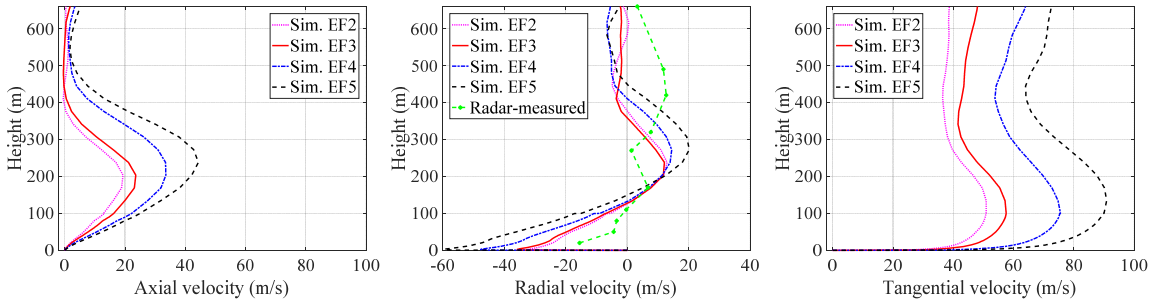

Figure 7. Numerically-simulated velocity profile as a function of height: (a) axial; (b) radial; (c) tangential.

Figure 8 shows the time variations for the axial, radial, and tangential velocity components at a point close to core radius at the elevation of 25m during the last 30 s. The figure exhibits significant fluctuations of the velocity components, demonstrating the rapid change of wind speed of tornadoes. Standard deviations are used to quantify the amount of variations of these sets of data values, which are 4.7, 10.2, and 7.7 for axial, radial, and tangential velocity component, respectively. The variation in radial velocity component is the largest.

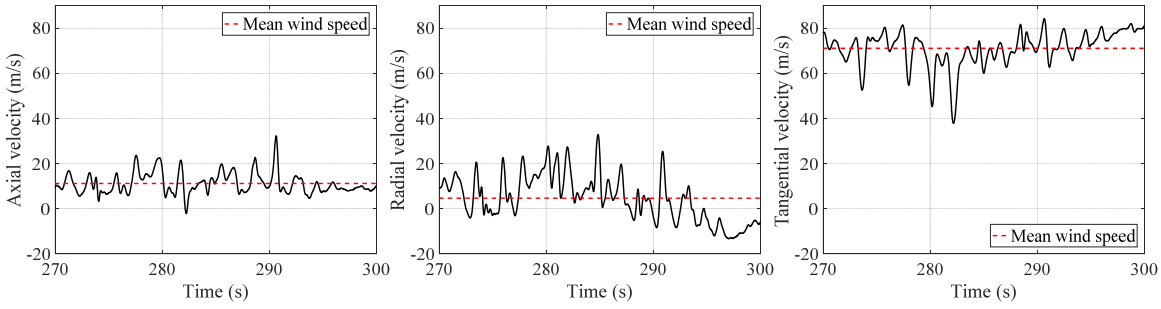

(a) (b) (c)

Figure 8. Time history of the velocity components at a point in space: (a) axial; (b) radial; (c) tangential.

The distribution of the static pressure along radial distance at the elevation of 80 m is shown in Figure 9. A significant pressure drop is found at the tornado core for all cases. To be specific, pressure drop is 3.5 kPa, 5.4 kPa, 9.5 kPa, and 10.7 kPa for EF2-EF5 tornadoes, respectively, if the pressure at the outer wall is taken as the reference pressure.

The radial Reynolds number (R_{e_r}) and the swirl ratio (S) control the structure of the tornadic flow (Church et al., 1979). Radial Reynolds number is essentially a measure

of the relative amount of the flow updraft strength to flow viscosity, reflecting the degree of flow turbulence, and it is defined as the ratio of volume flow rate to viscosity

$$\mathrm{R}_{e_r} = \frac{Q'}{2\pi\nu} = \frac{Q}{2\pi\nu h} \tag{3}$$

where Q' represents the volume flow rate per unit axial length of inflow height and Qrepresents the total volume flow rate through the system. Herein, $Q = 1.15 \times 10^7\ \mathrm{m}^3/s$; ν denotes kinematic viscosity ($1.53 \times 10^{-5}\ \mathrm{m}^2/s$), and h denotes the height of the velocity inlet (100 m). R_{e_r} of the EF3 tornado simulated here is 1.2×10^9, which falls into the estimated range of actual tornado cyclone flows, 10^9-10^{11} (Church et al., 1979).

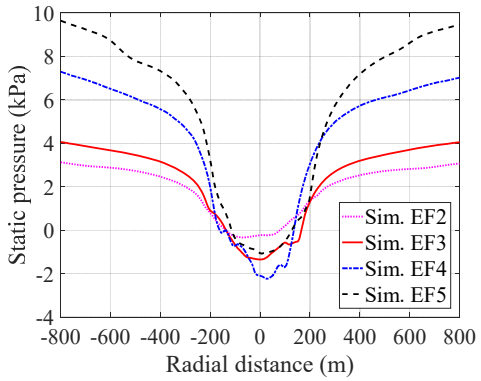

Figure 9. Static pressure profile as a function of radial distance.

Swirl ratio (S) is essentially a measure of the relative amount of angular to radial momentum in the vortex, reflecting the amount of rotational energy in the vortex relative to the convective energy in the vortex (Haan et al., 2008). S at a certain height is defined as

$$\mathrm{S} = \frac{\pi {r_o}^2 V_{t,max}}{Q} \tag{4}$$

where r_o is the core radius at that specific height, and $V_{t,max}$ is the corresponding maximum tangential velocity (the tangential velocity at the core radius) at that height. S of the EF3 tornado at seven representative heights are presented in Figure 10. S is larger than 1 from the dome apex (25 m) to 200 m, which is consistent with the radar observation that the S of Spencer Tornado exceeds 1 (Kosiba and Wurman, 2010).

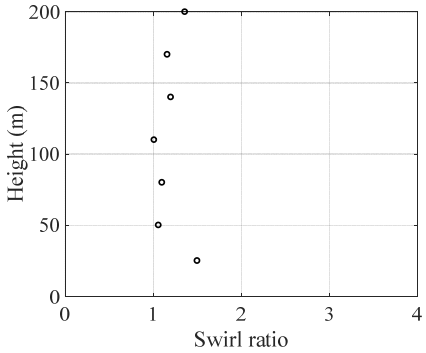

Figure 10. Swirl ratio at representative heights for EF3 tornado.

5. MODAL ANALYSIS RESULTS

Besides external dynamic loads, the dynamic responses of a structure also depend on its own dynamic characteristics, such as natural frequencies and mode shapes as well as damping. Therefore, a modal analysis is conducted to characterize the dynamic properties of the dome structure.

5.1. FINITE ELEMENT MODEL

A FEM of the dome structure is developed in ANSYS. The dimensions and the material properties of the dome structure have been specified in Section 2 and Figure 1. The developed FEM is shown in Figure 11. Beam188, which is a two-node linear beam

element, is used to model the beam members, and Shell181, which is a linear triangle or quadrilateral element, is used to model shells. Each edge of the shell is connected to the adjacent beam member by rigid connections along the length. In general, each beam member and the edge of shell is discretized into 10 elements, and in total, 28,139 nodes and 28,336 elements are generated. The bottom joints of the dome structure are assumed to be fixed. In this analysis, elastic material model is used for the steel, and the standard earth gravity and the external loads (tornadic wind pressure) are omitted.

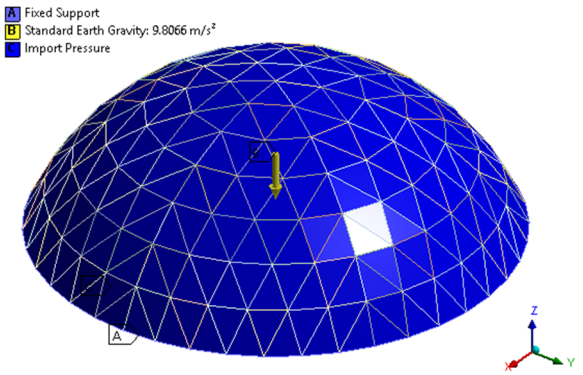

Figure 11. FEM of the dome structure.

5.2. NATURAL FREQUENCIES AND MODE SHAPES

Ten representative natural frequencies of the dome structure are listed in Table 1 and four representative mode shapes are presented in Figure 12. From Table 1, it can be seen that natural frequencies of this type of structure are very close to one another. The first natural frequency is 3.9485 Hz, and the deflection in the associated mode shape is confined to a 1/8 portion of the entire dome and it is out of the membrane plane. By comparing the obtained mode shapes, the higher the mode, the more the area on the surface is excited. In general, these mode shapes are local, as they are out of the

membrane plane and thus the stiffness of the shells (instead of the beam frame) dominates the modal analysis, and the shells are not good at transferring loading to a far location.

Table 1. Natural frequencies of the dome structure (with the beam frame and shell).

Mode No.	1	2	3	4	5	6	7	8	9	100
Natural frequency (Hz)	3.9485	3.9488	3.9510	3.9522	3.9550	3.9557	4.0875	4.0898	4.0921	5.4463

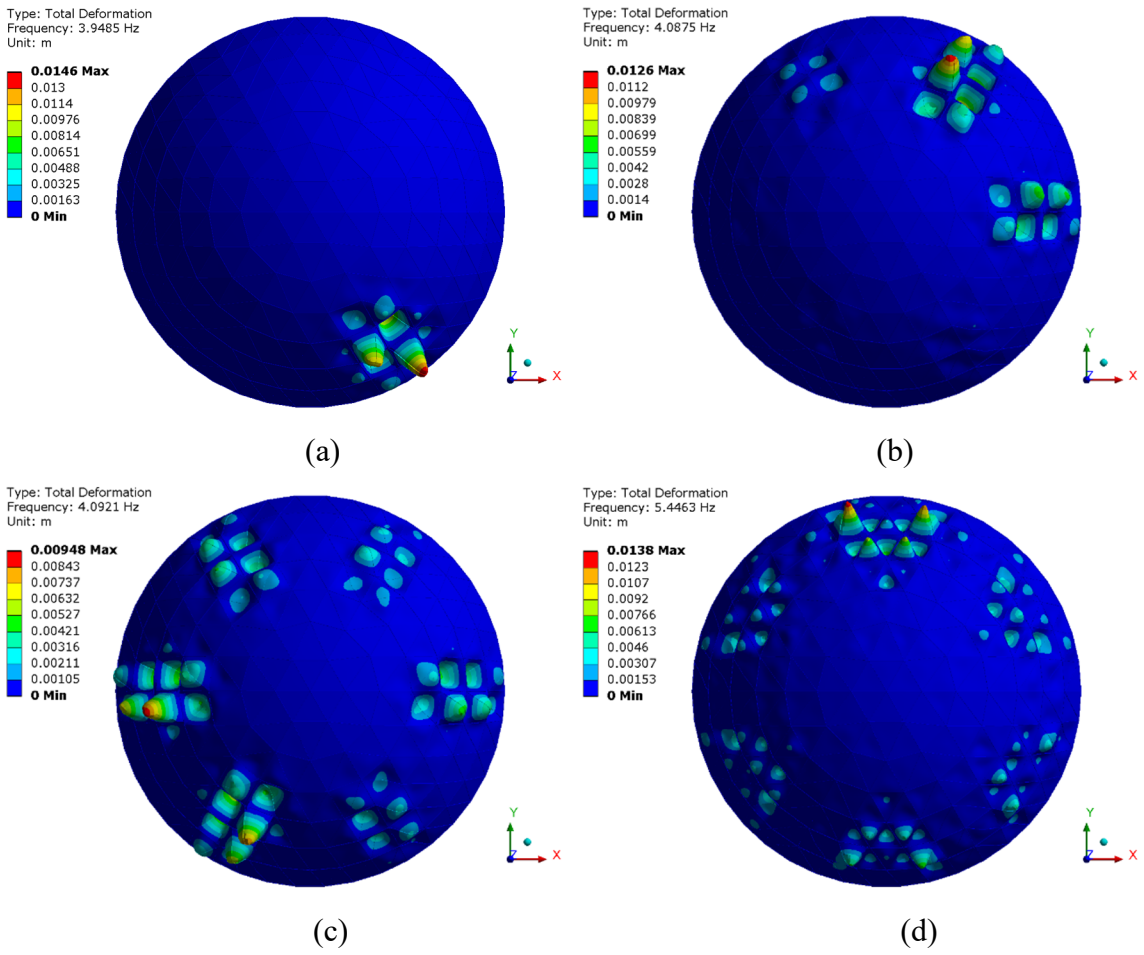

Figure 12. Representative mode shapes of the dome structure with the beam frame and shell: (a) 1st mode; (b) 7th mode; (c) 9th mode; (d) 100th mode.

6. WIND EFFECTS INDUCED BY TORNADO

To investigate the dynamic responses of the dome structure induced by tornadoes, the dome structure is placed in the computational domain (the tornadic wind field) to obtain tornado-induced wind pressure on the dome surface at each time instant. The dome structure in the tornadic wind field is assumed to be rigid, i.e., not deformable. In addition, aerodynamic damping is not considered since the dome structure is assumed to be rigid so that aerodynamic instability or negative aerodynamic damping is less likely to occur. Then the obtained wind pressure is imported onto the FEM of the dome structure through the transient load mapping technique (ANSYS, 2013), and a nonlinear transient FE analysis is conducted to obtain structural responses at each time instant. All geometric (large strain/deformation) and material nonlinearity are considered. Material nonlinearity is modeled by adopting a bilinear elastic-plastic constitutive model for the steel, with a yield strength of 250 MPa and post-yield stiffness ratio of 0.03 (tangent modulus of 6 GPa). Rayleigh damping is added to the FEM of the dome structure. The stiffness coefficient α is 0.000586 and the mass coefficient β is 0.671. This section will present the wind direction at the dome apex and the wind pressure on dome surface during the tornado passes the dome structure. Section 7 will present the structural responses in terms of displacement responses, acceleration responses and stress during the whole process.

6.1. WIND DIRECTION OF THE FLOW FIELD

Figure 13 displays the streamline of the resultant wind velocity when the dome structure is located on the right side of the tornado center in EF3 tornado. The wind flow

is swirling and rotating counterclockwise. At this moment, the wind blows towards the southeast corner of the dome structure, which is the windward direction. Similarly, when the dome structure moves to the left side of the tornado center, its northwest corner is the windward direction. The above information will explain where the positive pressure occurs on the dome surface. Figure 13 shows that wind direction in tornadic wind field changes very quickly.

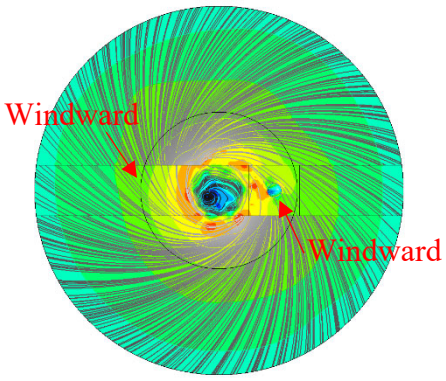

Figure 13. Streamline of the resultant wind velocity (for EF 3 tornado).

6.2. WIND PRESSURE ON DOME SURFACE

The wind pressure induced on the dome surface (hereafter "surface pressure") at six representative time instants during the last 48 s (while the dome moves from the right side to the left side of tornado center, see Figure 4) are presented in Figure 14. In general, all surface pressure is positive when the dome is far away from tornado center, while negative surface pressure is gradually developed when the dome approaches the tornado center. From Figures 14(a) and (b), when the dome is on the right side of the tornado center, the wind blows towards the southeast corner of the dome, at which the surface pressure is positive. As shown in Figure 14(c), when the dome moves to core radius (165

m is the core radius at the height of dome apex, 25 m), the wind blows from due south and the surface pressure near the south edge of the dome is positive. From Figure 14(d), when the dome center is exactly at the tornado center, relatively uniform negative pressure is distributed across the whole surface. The negative pressure is contributed from the large atmospheric pressure drop within the tornado core (see Figure 9). When the dome moves to the left side of the tornado center (Figures 14(e) and (f)), large positive pressure is found at the northwest corner of the dome, which is the windward direction. It is also observed that the maximum positive pressure appears on the part of the dome structure that is closer to the ground (e.g., red color in Figures 14(a), (b) and (f)) and that the maximum negative pressure in magnitude appears approximately at the top of the dome structure (e.g., blue color in Figures 14(c) and (f)). This is consistent with previous findings reported by Yousef et al. (2018). The overall forces and moments acting on the dome structure are estimated by integrating the surface pressure and compared to previous numerical and experimental data. They are not presented here due to the length of the content. More details can be found in Li et al. (2019).

During the dome moves, the time histories of maximum and minimum surface pressure for EF2-EF5 tornadoes are presented in Figure 15. It should be noted that the maximum/minimum surface pressure at different time instants may not be associated with the same location of the dome. In Figure 15, the first dashed line is associated with the time instant when the dome center moves to the core radius of the tornado, approaching the tornado; the second dashed line is for the time instant when the dome center moves to the tornado center; and the third dashed line is for the time instant when the dome center moves to the core radius, leaving the tornado. From Figure 15(a), the

maximum surface pressure experiences a large drop within the core. This is caused by the large atmospheric pressure drop inside the tornado core (see Figure 9). The maximum surface pressure reaches its valley when the dome center is at the tornado center. The lowest values of the maximum surface pressure of EF2 and EF5 tornadoes are around 0, but those of EF3 and EF4 tornadoes are below 0. This indicates that the dome structure subjects to negative pressure when it is at the tornado center, which is consistent with the contour plot in Figure 14(d). Such low negative pressure causes large suction force on the dome. In respect to the minimum surface pressure, the trend is similar for EF2-3 tornadoes and their magnitudes remain relatively constant within core radius. However, for EF4-5 tornadoes, sudden drops happen at core radius and close to tornado center.

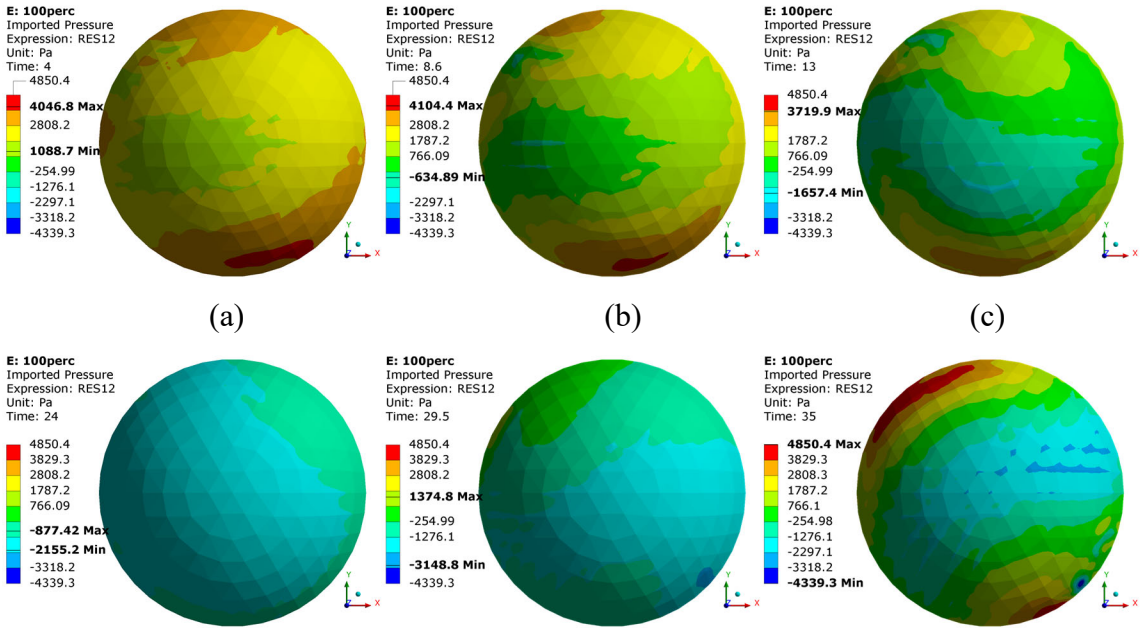

Figure 14. Surface pressure for EF3 tornado: (a) 4 s (300 m away from tornado center); (b) 8.6 s (231 m away from tornado center); (c) 13 s (165 m away from tornado center); (d) 24 s (0 m away from tornado center); (e) 29.5 s (-82.5 m away from tornado center); (f) 35 s (-165 m away from tornado center).

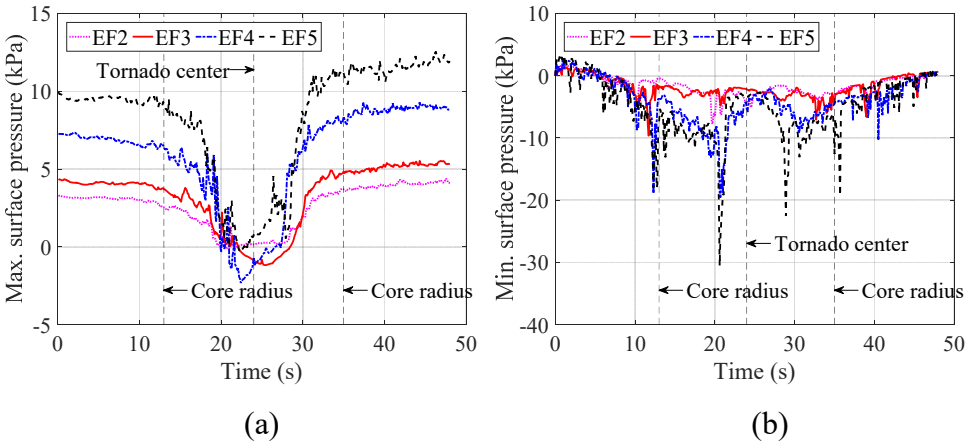

Figure 15. Time history of tornado-induced surface pressure: (a) Maximum; (b) Minimum.

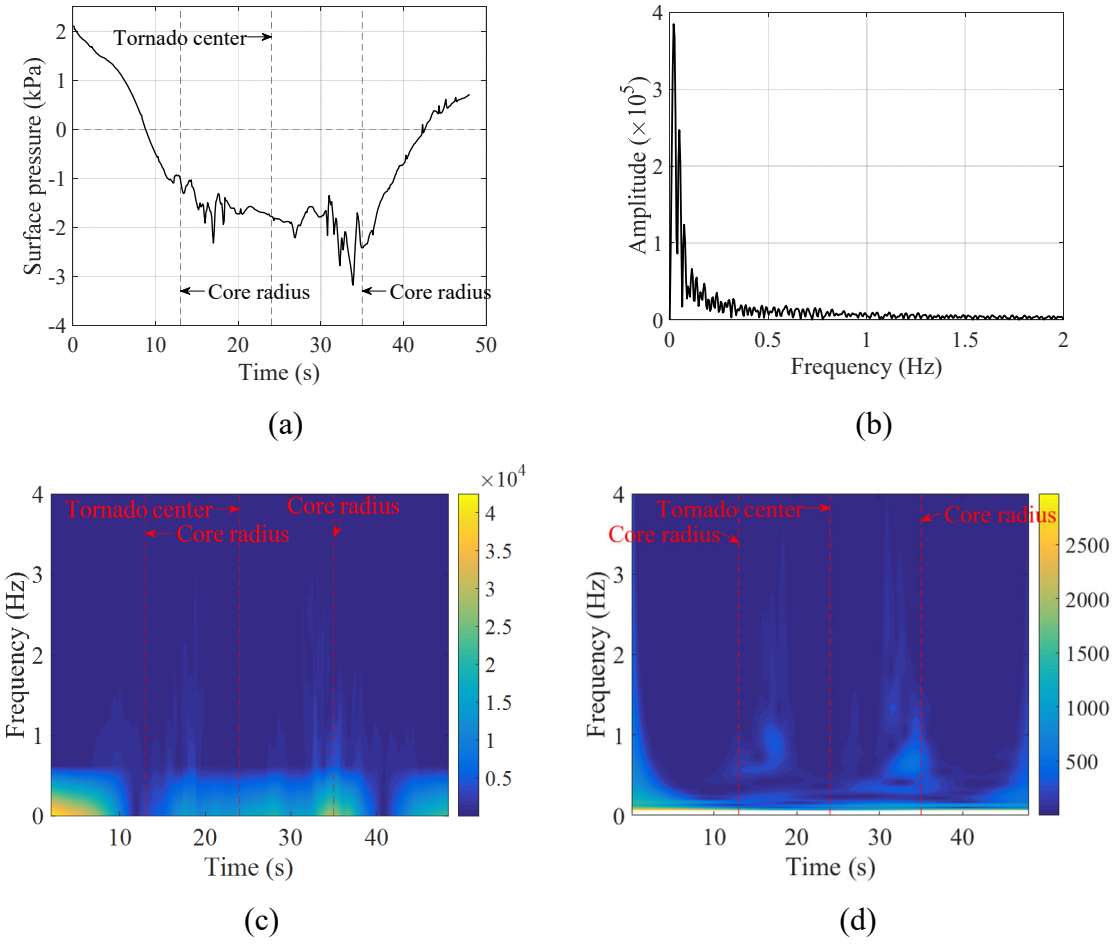

Figure 16. Surface pressure at the dome apex: (a) Time history; (b) Fourier transform; (c) Short-time Fourier transform; (d) Wavelet transform.

To characterize the dynamic characteristics of the wind pressure on the dome structure, the time history of surface pressure at a representative location of the dome (the dome apex) is extracted from EF3 tornado, and the Fourier transform, the short-time Fourier transform (STFT), and wavelet transform of the time history are carried out, as shown in Figure 16. From Figure 16(a), the surface pressure is positive when the dome is far away from tornado center, and it then decreases and becomes negative when the dome approaches tornado center, which is again due to the large atmospheric pressure drop at tornado center (Figure 9). The wind pressure drops and reaches as low as -3.2 kPa, while the dome center approaches the core radius the second time, which may be attributed from both the large atmospheric pressure drop and the wake effect. Figure 16(b) shows the Fourier transform of the surface pressure time history, where three major peaks are found at 0.02 Hz, 0.05 Hz, and 0.07 Hz, respectively. It indicates that the main frequency spectrum of the surface pressure is in the range of 0-0.30 Hz, which is relatively low. To obtain the frequency variation over time, Figure 16(c) presents the STFT of this surface pressure. The selected window length is 1.6 s for optimal time-frequency representation. From the time-frequency scalogram, the surface pressure varies more rapidly when the dome center moves into the tornado core, especially around core radius, which can be indicated by the presence of the higher frequency components at core radius (up to 3.15 Hz), although the magnitude of the related higher frequency components is low. The time-frequency scalogram is also obtained from wavelet transform and shown in Figure 16(d). The Morlet mother wavelet is used in this analysis, and the center frequency is 1 Hz (2π rad/s) to guarantee the best time resolution. Similar observations are found compared to STFT. Overall, the dominant frequency components of the surface pressure

are below 1 Hz over the entire time duration, which is much less than the first natural frequency of the dome structure (3.95 Hz). Therefore, resonant response is not expected. In fact, the largest deformation from the nonlinear, transient analysis is only 0.41 m, verifying that resonant vibration did not occur.

7. TORNADO-INDUCED STRUCTURAL RESPONSES

7.1. DISPLACEMENT RESPONSES

For the EF3 tornado, the deformation profiles of the entire structure at the six representative time instants are illustrated in Figure 17. From Figure 17(a), the dome structure deforms inward symmetrically, as the surface pressure is all positive and relatively uniform when the dome structure is far away from the tornado center (see Figure 14(a)). The maximum deformation is 0.123 m at this time instant. Figure 17(b) presents the deformation when the dome structure moves closer to the tornado center. Although negative surface pressure is developed, it only covers a small area, and thus the dome still deforms inward. The maximum deformation reduces to 0.11 m. As shown in Figure 17(c), when the dome center passes the core radius the first time, the deformation becomes smaller, since the change in pressure direction from being positive to negative causes some deformation to cancel out. From Figure 17(d), when the dome center is at the tornado center, outward deformation occurs on the dome surface due to the negative pressure caused by the atmospheric pressure drop (see Figure 9). However, the deformation is small (0.0127m), which is because the displacement caused by positive surface pressure at the previous time instants is balanced out by the displacement caused

by the negative pressure at this time instant. That is to say, even though the atmospheric pressure drop is present and large negative pressure is developed when the dome center moves to the tornado center, the displacement on the structure at this stage does not reach its worst scenario. From Figure 17(e), when the dome center passes half of the core radius the second time, most of the dome surface still deforms outward, since negative surface pressure still remains dominant. When the dome center passes the core radius the second time (see Figure 17(f)), the deformation profile is similar to Figure 17(c) when it passes the core radius the first time.

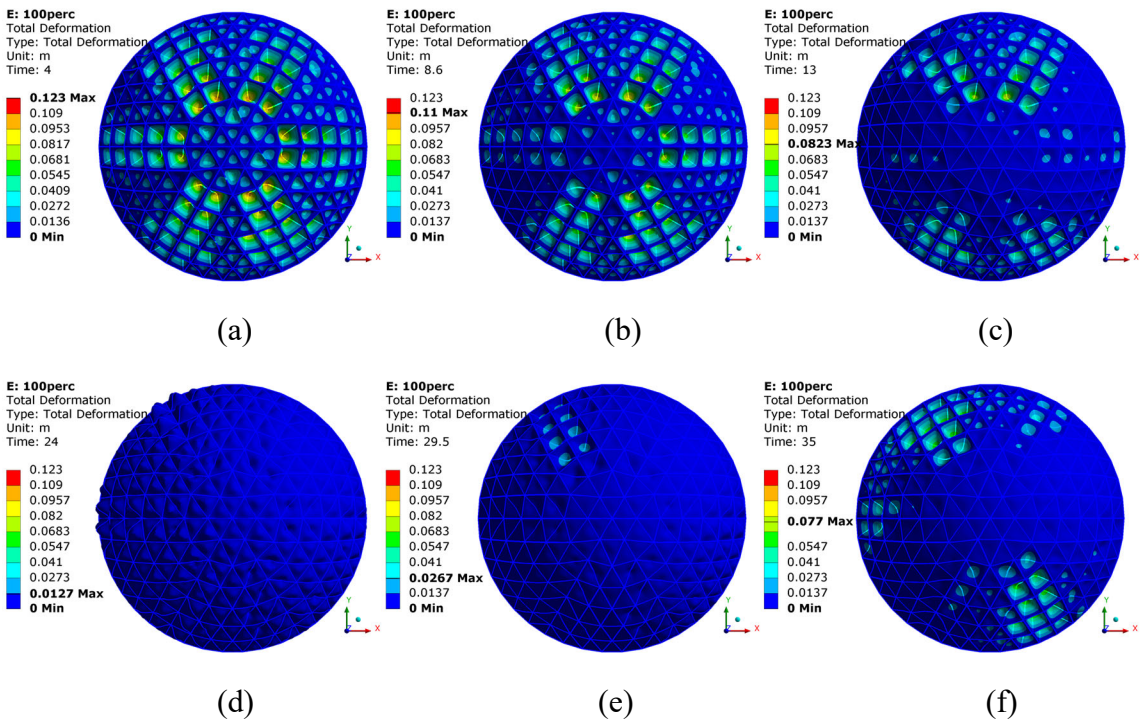

Figure 17. Deformation profile of the entire structure for EF3 tornado: (a) 4 s (300 m away from tornado center); (b) 8.6 s (231 m away from tornado center); (c) 13 s (165 m away from tornado center); (d) 24 s (0 m away from tornado center); (e) 29.5 s (-82.5 m away from tornado center); (f) 35 s (-165 m away from tornado center). Note: larger scale is used to display the deformation of (d) and (e) other than true scale for better representation, while the range of the color bar is kept the same for all figures.

Figure 18 presents the deformation profile of the beam frame for EF3 tornado, and they experience almost the same maximum displacement as the entire structure. This is because surface pressure is transferred to the beam frame via shells, and the deformation of the shells leads to that of the beam frame, resulting in the compatibility of deformation.

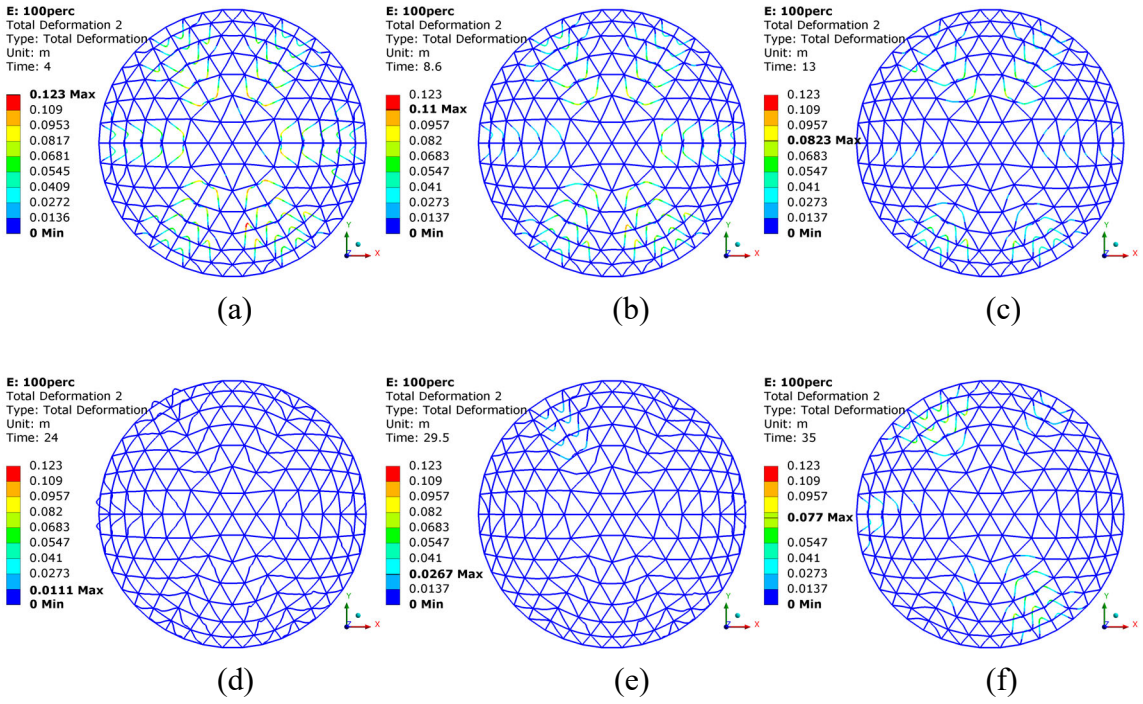

Figure 18. Deformation profile of the beam frame for EF3 tornado: (a) 4 s (300 m away from tornado center); (b) 8.6 s (231 m away from tornado center); (c) 13 s (165 m away from tornado center); (d) 24 s (0 m away from tornado center); (e) 29.5 s (-82.5 m away from tornado center); (f) 35 s (-165 m away from tornado center). Note: larger scale is used to display the deformation of (d) and (e) other than true scale for better representation, while the range of the color bar is kept the same for all figures.

The time history of maximum resultant displacement obtained from the beam frame is presented in Figure 19. During the first four seconds, the effect of the sudden application of surface pressure on structural responses applies, which is outside the scope

of this study. Therefore, the raised cosine filtering is applied to the first four seconds of data to mitigate the transient effects. The general trend of the maximum resultant displacement agrees with the variation of the surface pressure (Figure 15), suggesting that local deformation may be controlled by local surface pressure. More specifically, when the dome structure is away from tornado center, maximum surface pressure controls (Figure 15(a)) since the dome structure deforms inward. Similarly, when the dome structure is in and around tornado core, the deformation of the dome structure is controlled by the minimum surface pressure (Figure 15(b)). The maximum displacement of EF5 tornado is 17%, 61%, and 73% higher than that of EF4, EF3, and EF2 tornadoes, respectively. When the dome center is around tornado center, the displacement is much smaller, which verifies the aforementioned statement that the previous displacement due to positive surface pressure is balanced out by the displacement due to negative wind pressure when tornado center is reached.

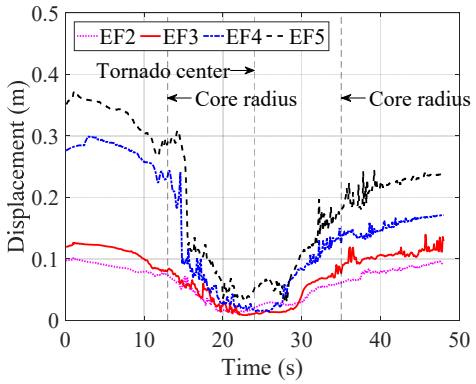

Figure 19. Time history of maximum resultant displacement on the beam frame.

Figure 20 presents the time histories of displacement components in three directions at the dome apex for the four simulated tornadoes. The same trend is observed

in all four cases, but the fluctuations in three displacement components under EF4 and EF5 tornadoes are greater. For example, standard deviations of D_z for EF4 and EF5 tornadoes are 0.0045, and 0.0170, which are much higher than those for EF2 and EF3 tornadoes (0.0015 and 0.0018). In general, the tornado does not induce significant displacements in the horizontal directions, but it induces a significant displacement in the vertical direction, which is consistent with the fact that the induced total force in the vertical direction (F_z) is much higher than the two total forces in the horizontal direction (F_x and F_y). In addition, from the structural perspective, the dome structure is strong in the plane due to the membrane stress and relatively weak out of the plane.

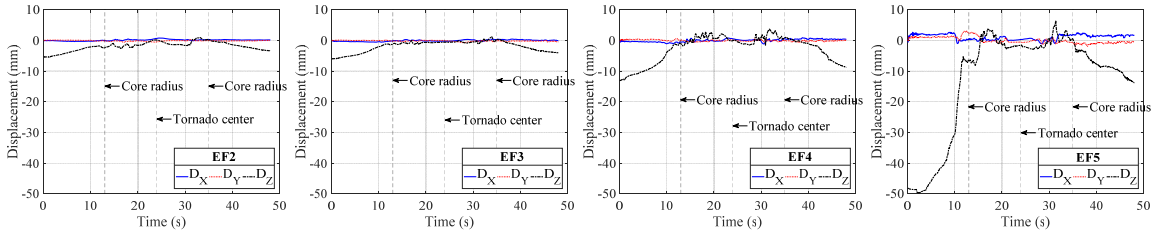

(a) (b) (c) (d)

Figure 20. Time history of displacement components in three directions at the dome apex: (a) EF2; (b) EF3; (c) EF4; (d) EF5.

7.2. ACCELERATION RESPONSES

The time histories of acceleration components in three directions at the dome apex under all four simulated tornadoes are presented in Figure 21. Acceleration responses under EF2 and EF3 tornadoes are much smaller compared to that under EF4 and EF5 tornadoes. For EF4 and EF5 tornadoes, very large fluctuations of acceleration are found when the dome center is around core radius, indicating the non-stationary characteristics

of surface pressure. When the dome center is at the tornado center, the acceleration dies out, which is consistent with the change trend of displacement in Figure 19.

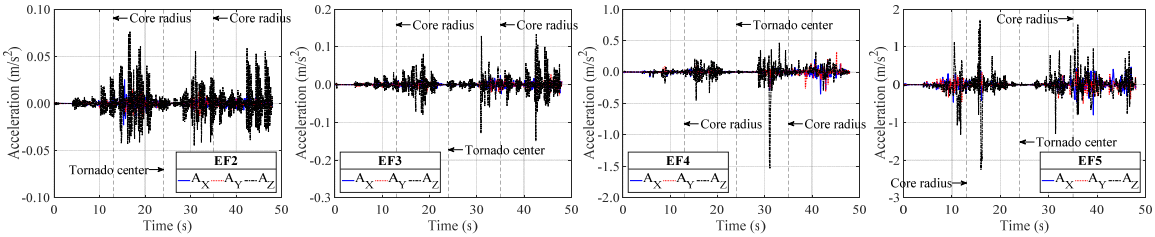

(a) (b) (c) (d)

Figure 21. Time history of acceleration components in three directions at the dome apex: (a) EF2; (b) EF3; (c) EF4; (d) EF5.

Figure 22 presents the time histories of acceleration responses at other four representative locations on the dome surface, where are indicated by the red dots. If the locations are on the left side of the dome (Figures 22(a) and (c)), large acceleration responses occur when the dome is around the core radius the first time. At this moment, the dome is on the right side of the tornado center, and the red dot in each figure is on the leeward side of the dome. If the location is not only on the left side of the dome but also close to the dome edge (see Figure 22(c)), the acceleration becomes significant even earlier.

On the contrary, when the locations are on the right side of the dome (Figures 22(b) and (d)), large acceleration responses occur when the dome is around the core radius the second time. At this moment, the dome is on the right side of the tornado center, and the red dot in each figure is again on the leeward side of the dome. This suggests that the wind flow on the leeward side is more turbulent, leading to higher acceleration responses.

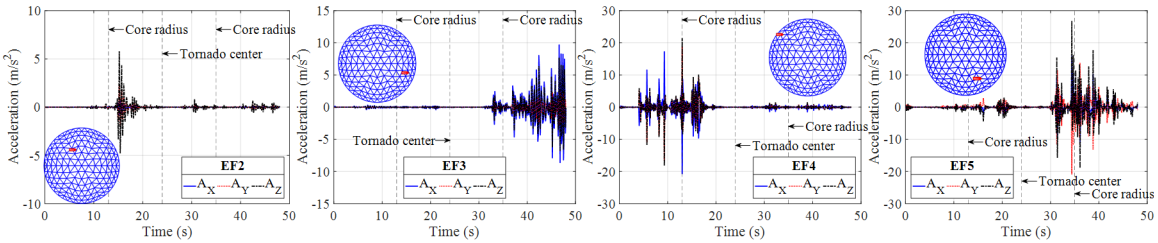

(a) (b) (c) (d)

Figure 22. Time history of acceleration components in three directions at other representative locations: (a) EF2; (b) EF3; (c) EF4; (d) EF5.

7.3. INDUCED STRESS ON SHELLS AND BEAM MEMBERS

The von-Mises stress on shells under EF3 tornado are presented in Figure 23. Since the beam frame is much stronger than the shells, the deformation of the shells is firmly restricted by the beam members, resulting in stress concentration along the beam members. Moreover, the stress distribution agrees with the structural deformation, as large deformation is normally induced by large stress before yielding.

The time histories of maximum von-Mises stresses on the shells under all simulated tornadoes are presented in Figure 24. No yielding occurs on shells under EF2-EF4 tornadoes. Moreover, a similar trend of their stress variation is observed, i.e. stress decreases when the dome center is close to the core radius the first time, remains stable around tornado center, and increases as the dome center moves further away from tornado center. This trend is consistent with the time history of maximum resultant displacement in Figure 19, implying that large deformation is caused by large stress. However, for EF5 tornado, the shell yields at the very beginning due to the abrupt application of surface pressure, but it then returns to the elastic state. When the dome passes core radius the first time, yielding happens again. When the dome is around tornado center, the stress decreases to 225 MPa due to the fact that the previous positive

pressure cancels out some of the developed negative pressure. Then, the stress increases again and vibrates around the yielding point (250 MPa). The second yielding (around the core radius the first time) of the shells under the EF5 tornado justifies the fluctuations of the acceleration in Figure 22(d) between 10 s to 20 s, since the stiffness of the structure becomes smaller after yielding occurs.

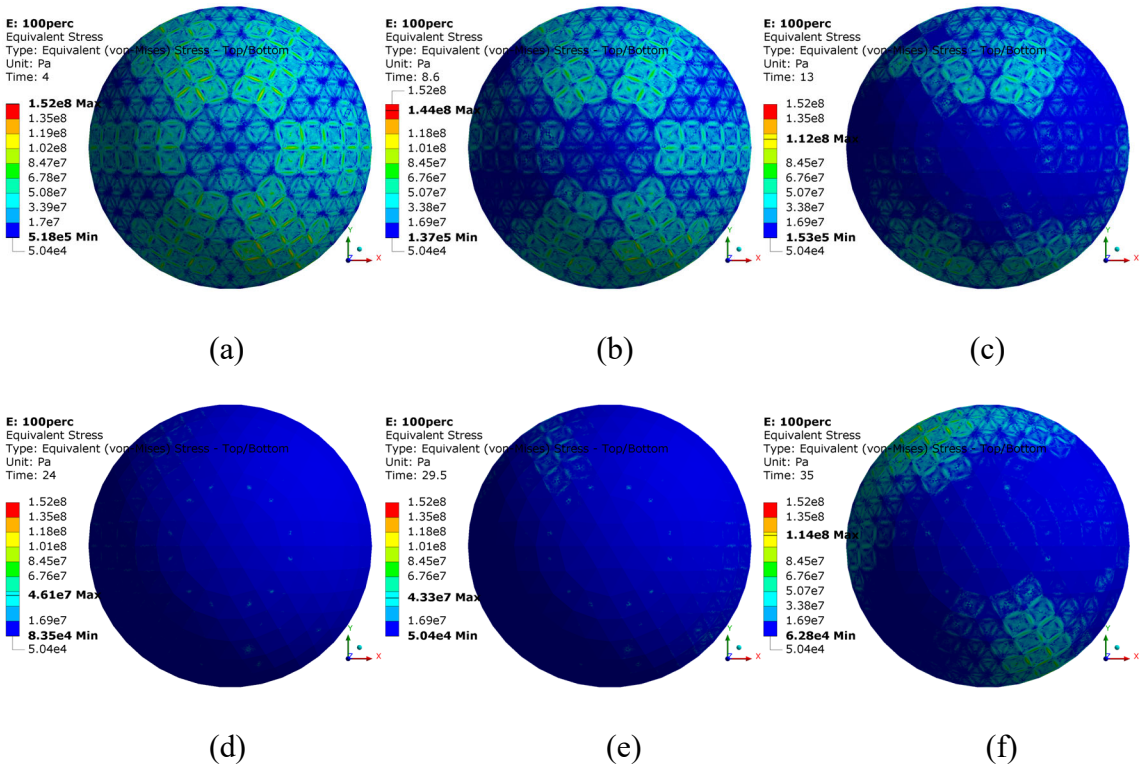

Figure 23. Contours of von-Mises stress for shells for EF3 tornado: (a) 4 s (300 m away from tornado center); (b) 8.6 s (231 m away from tornado center); (c) 13 s (165 m away from tornado center); (d) 24 s (0 m away from tornado center); (e) 29.5 s (-82.5 m away from tornado center); (f) 35 s (-165 m away from tornado center).

The combined stress is adopted to describe behavior of the beam members. The combined stress consists of the stress component (σ_{dir}) due to axial load and a bending-

stress component (σ_y^T, σ_y^B, σ_z^T or σ_z^B) due to bending moment, which are expressed in Equations (5)-(9).

$$\sigma_{dir} = F_x/A \tag{5}$$

$$\sigma_y^T = -M_z \times y_{max}/I_{zz} \tag{6}$$

$$\sigma_y^B = -M_z \times y_{min}/I_{zz} \tag{7}$$

$$\sigma_z^T = M_y \times z_{max}/I_{yy} \tag{8}$$

$$\sigma_z^B = M_y \times z_{min}/I_{yy} \tag{9}$$

where F_x is the axial load; A is the cross-sectional area of the beam member; M_y and M_z are the bending moments; y_{max}, y_{min}, z_{max} and z_{min} are the maximum and minimum y, z coordinates in the cross-section measured from the centroid; and I_{yy} and I_{zz} are the moments of inertia of the cross section. The superscripts of T and B denote the top and bottom of the cross-section.

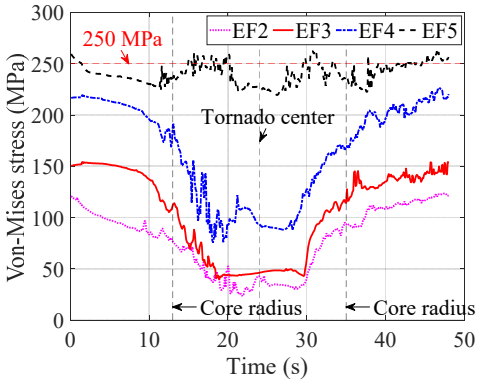

Figure 24. Time history of maximum von-Mises stress of the shells.

The minimum combined stress is defined as the minimum value of the combination of axial-stress and bending-stress components. For instance, the minimum

combined stress equals σ_{dir} plus the minimum value of σ_y^T, σ_y^B, σ_z^T and σ_z^B. The same rule applies to the maximum combined stress. The minimum and maximum combined stress of the beam frame are shown in Figures 25 and 26. Similar trend is observed for each time instant disregarding the combination types.

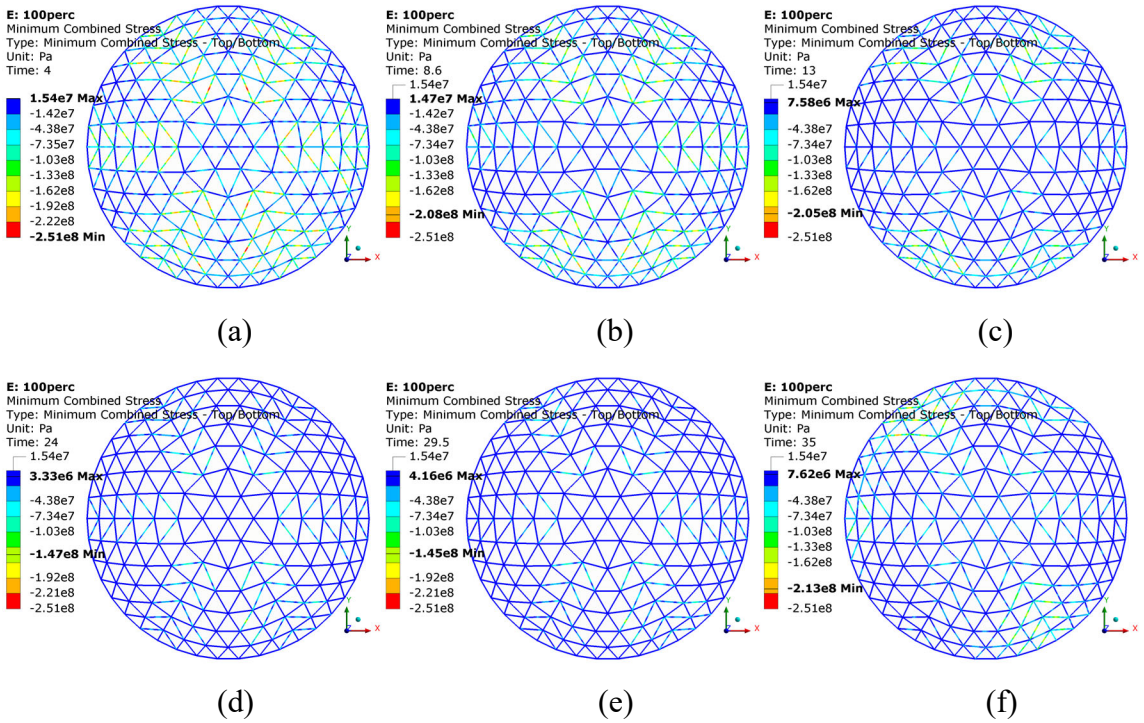

Figure 25. Contours of minimum combined stress of the beam frame for EF3 tornado: (a) 4 s (300 m away from tornado center); (b) 8.6 s (231 m away from tornado center); (c) 13 s (165 m away from tornado center); (d) 24 s (0 m away from tornado center); (e) 29.5 s (-82.5 m away from tornado center); (f) 35 s (-165 m away from tornado center).

To be more specific, the time histories of maximum and minimum values of the two combined stresses for the beam frame are presented in Figure 27. For EF2 and EF3 tornadoes, the combined stress reaches the yielding point very late, i.e. after the dome passes the core radius the second time. For EF4 and EF5 tornadoes, the beam frame

yields at the very beginning that is followed by a sudden increase (or drop) when the dome approaches the core radius the first time and then it remains stable.

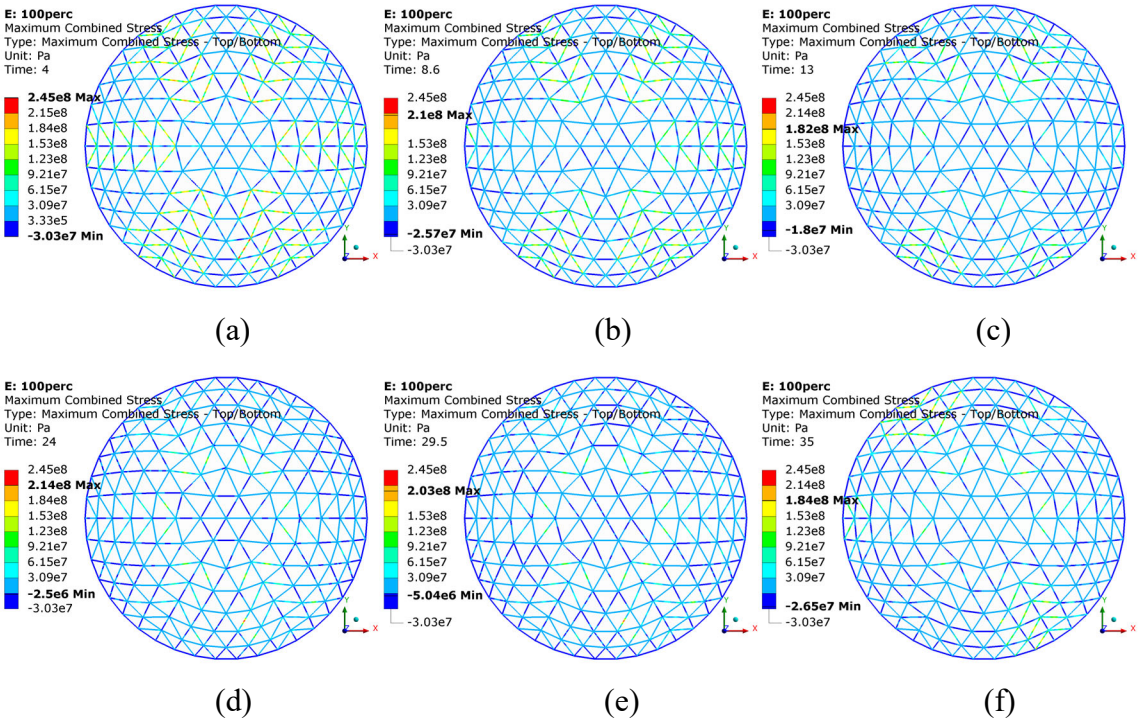

Figure 26. Contours of maximum combined stress of the beam frame for EF3 tornado: (a) 4 s (300 m away from tornado center); (b) 8.6 s (231 m away from tornado center); (c) 13 s (165 m away from tornado center); (d) 24 s (0 m away from tornado center); (e) 29.5 s (-82.5 m away from tornado center); (f) 35 s (-165 m away from tornado center).

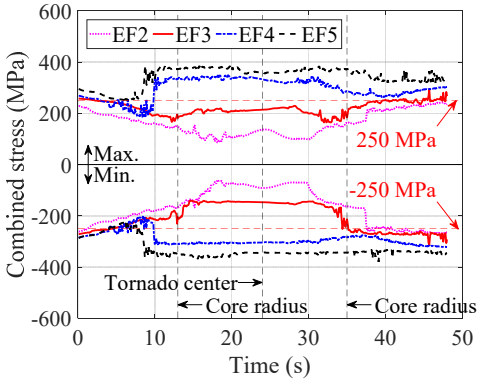

Figure 27. Time history of maximum and minimum values of the two combined stresses of the beam frame.

Figure 28 shows the time history of the two combined stresses at the dome apex under all four simulated tornadoes, together with the time history of the von-Mises stress at the location very close to the dome apex. The maximum and minimum values of the combined stress are almost symmetric about the *x*-axis, and their trends are similar under all four simulated tornadoes, i.e., the peak values occur when the dome structure is around core radius. In all cases, von-Mises stress is much smaller than the magnitude of the two combined stresses, which implies that the shells are thick enough to transfer surface pressure to the beam frame. In addition, both the combined stresses on the beam frame and von-Mises stress on the shells for EF4 and EF5 tornadoes experience more prominent variation over time than those for EF2 and EF3 tornadoes. This is because the dome becomes flexible and vibrates more severely due to the early yielding of the beam frame under EF4 and EF5 tornadoes.

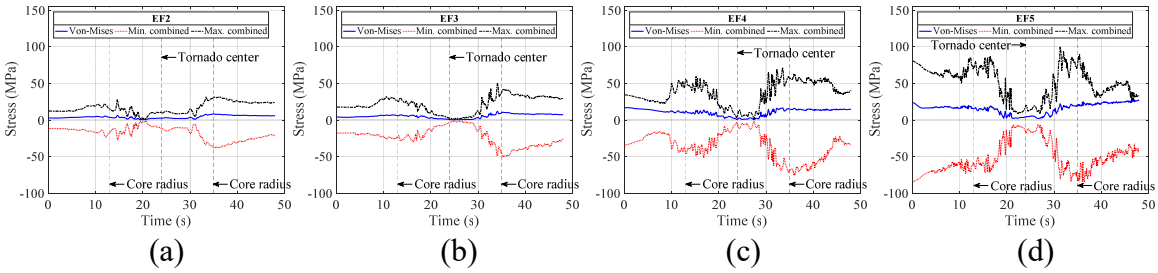

Figure 28. Time history of combined and von-Mises stresses at dome apex: (a) EF2; (b) EF3; (c) EF4; (d) EF5.

The time histories of the combined and von-Mises stresses at other representative locations are presented in Figure 29. The yellow dots on the dome structure denote the locations where von-Mises stresses are obtained, while the red ones denote the locations where combined stresses are obtained. For EF2 tornado, yielding is not observed for

these two specific locations. For EF3 tornado, the combined stress on the specified beam frame reaches the yielding stress when the dome moves further away from the core radius. In regard to EF4 and EF5 tornadoes, the yielding of the specified beam frame occurs when the dome passes core radius the first time. Among the specified locations of shells, only the one under EF5 tornado yields, which also contributes to severe fluctuations of the combined stress when the dome is at core radius the second time.

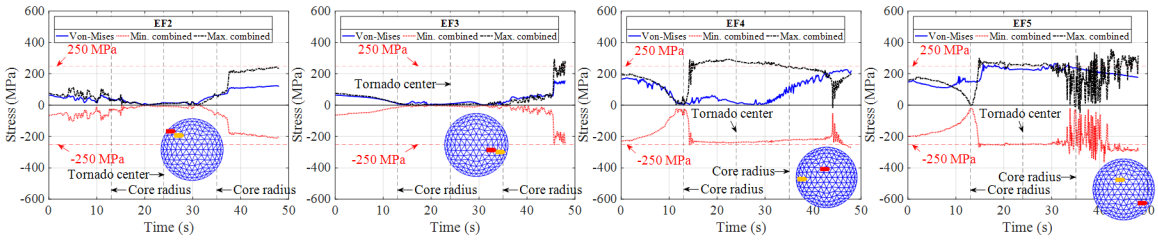

(a) (b) (c) (d)

Figure 29. Time history of combined and von-Mises stresses at other representative locations: (a) EF2; (b) EF3; (c) EF4; (d) EF5.

8. CONCLUSIONS

A transient time-history analysis of a long-span dome structure is performed to systematically investigate its dynamic responses induced by a translating tornado. The surface pressure caused by translating tornadoes with different intensities is determined by CFD simulations. The following conclusions can be drawn:

- The tangential velocity profile extracted from the simulated tornadic wind field agrees well with that extracted from the radar-measured data during

Spencer Tornado, which demonstrates the appropriate setup for the CFD simulations.

- Surface pressure becomes non-stationary when the dome center approaches the core radius of the tornado. At the same time, the dome structure experiences high vibration (high acceleration responses) on the leeward side, where the flow separation and/or potential flow reversal increases the non-stationary characteristics of surface pressure.
- The non-stationary characteristics of tornadic wind pressure is mainly caused by the change in wind angle of attack acting on the dome structure during the tornado translates.
- When the dome approaches the tornado center, existing structural deformation caused by positive surface pressure is cancelled out by some of the negative surface pressure. Therefore, the maximum deformation of the dome structure becomes very small. Although large negative pressure is developed because of atmospheric pressure drop when the tornado center is reached, structural deformation does not reach the worst scenario.
- Wind flow of EF4 and EF5 tornadoes are more turbulent than that of EF2 and EF3 tornadoes, and thus higher dynamic responses are experienced.

Based on the fact that the dynamic responses induced by tornadoes are significant, design of large-span dome structures should consider both static and dynamic impacts of tornadic winds, as the acceleration-related inertial force can be significant. In the future, an equivalent straight-line wind field will be developed. By comparing the dynamic

responses induced by tornadic winds and the equivalent straight-line winds, the gust-effect factor, G, in the pressure calculation equation will be determined.

ACKNOWLEDGEMENTS

This work was supported by National Science Foundation, the Hazard Mitigation and Structural Engineering program, through the project of "Damage and Instability Detection of Civil Large-scale Space Structures under Operational and Multi-hazard Environments" [award number 1455709].

REFERENCES

Ahmad, S., Ansari, E., & Gupta, H. (2014). Dynamic response of plane frame buildings subjected to tornado loads. Journal of Mechanical and Civil Engineering, 2320-334X, 63-69.

ANSYS (2013). Release 15.0. Help system. One-Way Fluid-Structure-Interaction enhanced by ACT, ANSYS, Inc.

Burgers, J. M. (1948). A mathematical model illustrating the theory of turbulence. Advances in Applied Mechanics, 1, 171-199.

Chang, C. C. (1966). First real man made tornado is generated in laboratory cage by space scientists at the catholic University of America. News item of PI of CUA.

Chang, C. C. (1971). What we learned from the tornado of Lubbock, Texas, USA, May 11, 1970. In Proceedings of the Third International Conference on Wind Effects on Buildings and Structures, 471-480.

Church, C. R., Snow, J. T., & Agee, E. M. (1977). Tornado vortex simulation at Purdue University. Bulletin of the American Meteorological Society, 58(9), 900-908.

Church, C., Snow, J. T., Baker, G. L., & Agee, E. M. (1979). Characteristics of tornado-like vortices as a function of swirl ratio: A laboratory investigation. Journal of the Atmospheric Sciences, 36(9), 1755-1776.

Deppermann, C. E. (1947). Notes on the origin and structure of Philippine typhoons. Bulletin of the American Meteorological Society, 28, 399-404.

Diamond, C. J., & Wilkins, E. M. (1984). Translation effects on simulated tornadoes. Journal of the atmospheric sciences, 41(17), 2574-2580.

Dutta, P. K., Ghosh, A. K., & Agarwal, B. L. (2002). Dynamic response of structures subjected to tornado loads by FEM. Journal of Wind Engineering and Industrial Aerodynamics, 90(1), 55-69.

Elawady, A., Aboshosha, H., El Damatty, A., Bitsuamlak, G., Hangan, H. & Elatar, A. (2017). Aero-elastic testing of multi-spanned transmission line subjected to downbursts. Journal of Wind Engineering and Industrial Aerodynamics, 169, 194-216.

El Damatty, A. & Elawady, A. (2018). Critical load cases for lattice transmission line structures subjected to downbursts: Economic implications for design of transmission lines. Engineering structures, 159, 213-226.

Gallus, W. A., Sarkar, P. P., Haan, F. L., Kuai, L., Kardell, R., & Wurman, J. (2004). A translating tornado simulator for engineering tests: Comparison of radar, numerical model, and simulator winds. Preprints, 22nd Conf. Severe Local Storms, Hyannis, MA, American Meteorological Society.

Gallus, W.A., Haan, F.L., Sarkar, P.P., Kuai, L., & Wurman, J. (2006). Comparison of numerical model and laboratory simulator tornado wind fields with radar observations of the Spencer, South Dakota tornado. In Symp. on the Challenges of Severe Convective Storms, 86th AMS Annual Meeting, Atlanta, GA, American Meteorological Society.

Haan, F. L., Sarkar, P. P., & Gallus, W. A. (2008). Design, construction and performance of a large tornado simulator for wind engineering applications. Engineering Structures, 30(4), 1146-1159.

Haan, F. L., Balaramudu, V. K., & Sarkar, P. P. (2010). Tornado-induced wind loads on a low-rise building. Journal of structural engineering, 136(1), 106-116.

Haan, F. L., Sarkar, P. P., Kopp, G. A., & Stedman, D. A. (2017). Critical wind speeds for tornado-induced vehicle movements. Journal of Wind Engineering and Industrial Aerodynamics, 168, 1-8.

Hamada, A. & El Damatty, A. (2016). Behaviour of transmission line conductors under tornado wind. Wind and Structures, An International Journal, 22(3), 369-391.

Hangan, H. (2014). The wind engineering energy and environment (WindEEE) dome at western university, Canada. Wind Engineers, JAWE, 39(4), 350-351.

Hangan, H. & Kim, J.D. (2008). Swirl ratio effects on tornado vortices in relation to the Fujita scale. Wind and Structures, 11(4), 291-302.

Hu, H., Yang, Z., Sarkar, P., & Haan, F. (2011). Characterization of the wind loads and flow fields around a gable-roof building model in tornado-like winds. Experiments in fluids, 51(3), 835-851.

Ishihara, T., Oh, S., & Tokuyama, Y. (2011). Numerical study on flow fields of tornado-like vortices using the LES turbulence model. Journal of Wind Engineering and Industrial Aerodynamics, 99(4), 239-248.

IS875 Part 3 (1987). Code of practice for design loads (other than earthquake) for buildings and structures. Bureau of Indian Standards, New Delhi.

Kosiba, K., & Wurman, J. (2010). The three-dimensional axisymmetric wind field structure of the Spencer, South Dakota, 1998 tornado. Journal of the Atmospheric Sciences, 67(9), 3074-3083.

Kuai, L., Haan Jr, F. L., Gallus, W. A., & Sarkar, P. P. (2008). CFD simulations of the flow field of a laboratory-simulated tornado for parameter sensitivity studies and comparison with field measurements. Wind and Structures, 11(2), 75-96.

Leslie, F. W. (1977). Surface roughness effects on suction vortex formation: A laboratory simulation. Journal of the Atmospheric Sciences, 34(7), 1022-1027.

Lewellen, W. S., Lewellen, D. C., & Sykes, R. I. (1997). Large-eddy simulation of a tornado's interaction with the surface. Journal of the Atmospheric Sciences, 54(5), 581-605.

Li, T., Yan, G. & Han, D. (2019). Investigate the influence of flow structure of a tornado on wind effects. Engineering Structures. (Under review).

McDonald, J.R., Mehta, K.C., Smith, D.A., Womble, J.A. (2010). The enhanced Fujita scale: development and implementation. In proceedings of Forensic Engineering 2009: Pathology of the Built Environment, 719-728.

Mishra, A. R., James, D. L., & Letchford, C. W. (2008a). Physical simulation of a single-celled tornado-like vortex, Part A: Flow field characterization. Journal of Wind Engineering and Industrial Aerodynamics, 96(8), 1243-1257.

Mishra, A. R., James, D. L., & Letchford, C. W. (2008b). Physical simulation of a single-celled tornado-like vortex, Part B: Wind loading on a cubical model. Journal of Wind Engineering and Industrial Aerodynamics, 96(8), 1258-1273.

Natarajan, D. (2011). Numerical simulation of tornado-like vortices. (Doctoral dissertation, The University of Western Ontario).

Natarajan, D., & Hangan, H. (2012). Large eddy simulations of translation and surface roughness effects on tornado-like vortices. Journal of Wind Engineering and Industrial Aerodynamics, 104, 577-584.

Pointwise (2016). Pointwise Tutorial Workbook. Pointwise, Inc, Texas, USA, chapter 9.

Rajasekharan, S. G., Matsui, M., & Tamura, Y. (2013). Characteristics of internal pressures and net local roof wind forces on a building exposed to a tornado-like vortex. Journal of Wind Engineering and Industrial Aerodynamics, 112, 52-57.

Razavi, A., & Sarkar, P. P. (2018a). Laboratory investigation of the effects of translation on the near-ground tornado flow field. Wind and Structures, 26(3), 179-190.

Razavi, A., & Sarkar, P. P. (2018b). Laboratory study of topographic effects on the near-surface tornado flow field. Boundary-Layer Meteorology, 1-24.

Refan, M., Hangan, H., & Wurman, J. (2014). Reproducing tornadoes in laboratory using proper scaling. Journal of Wind Engineering and Industrial Aerodynamics, 135, 136-148.

Refan, M., & Hangan, H. (2018). Near surface experimental exploration of tornado vortices. Journal of Wind Engineering and Industrial Aerodynamics, 175, 120-135.

Rott, N. (1958). On the viscous core of a line vortex. Zeitschrift für angewandte Mathematik und Physik ZAMP, 9(5-6), 543-553.

Sabareesh, G. R., Matsui, M., & Tamura, Y. (2013). Ground roughness effects on internal pressure characteristics for buildings exposed to tornado-like flow. Journal of Wind Engineering and Industrial Aerodynamics, 122, 113-117.

Selvam, R. P., & Millett, P. C. (2003). Computer modeling of tornado forces on a cubic building using large eddy simulation. J. Ark. Acad. Sci, 57, 140-146.

Selvam, R. P., & Millett, P. C. (2005). Large eddy simulation of the tornado-structure interaction to determine structural loadings. Wind and Structures, 8(1), 49-60.

Sengupta, A., Haan, F. L., Sarkar, P. P., & Balaramudu, V. (2008). Transient loads on buildings in microburst and tornado winds. Journal of Wind Engineering and Industrial Aerodynamics, 96(10), 2173-2187.

Strasser, M.N., Yousef, M.A. & Selvam, R.P. (2016). Defining the vortex loading period and application to assess dynamic amplification of tornado-like wind loading. Journal of Fluids and Structures, 63, 188-209.

Tang, Z., Feng, C., Wu, L., Zuo, D., & James, D. L. (2018a). Characteristics of tornado-like vortices simulated in a large-scale Ward-type simulator. Boundary-Layer Meteorology, 166(2), 327-350.

Tang, Z., Zuo, D., James, D., Eguchi, Y., & Hattori, Y. (2018b). Effects of aspect ratio on laboratory simulation of tornado-like vortices. Wind and Structures, 27(2), 111-121.

Tari, P.H., Gurka, R., & Hangan, H. (2010). Experimental investigation of tornado-like vortex dynamics with swirl ratio: the mean and turbulent flow fields. Journal of Wind Engineering and Industrial Aerodynamics, 98(12), 936-944.

Ward, N. B. (1972). The exploration of certain features of tornado dynamics using a laboratory model. Journal of the Atmospheric Sciences, 29(6), 1194-1204.

Wang, H., James, D., Letchford, C., Peterson R., & Snow, J. (2001). Development of a Prototype Tornado Simulator for the Assessment of Fluid-Structure Interaction. In Proceedings of the 1st Americas Conference on Wind Engineering, June 4-6, Clemson Uni., SC.

Wen, Y. K. (1975). Dynamic tornadic wind loads on tall buildings. Journal of the Structural Division, 101(1), 169-185.

Wurman, J., Kosiba, K., & Robinson, P. (2013). In situ, Doppler radar, and video observations of the interior structure of a tornado and the wind-damage relationship. Bulletin of the American Meteorological Society, 94(6), 835-846.

Wurman, J., & Alexander, C. R. (2005). The 30 May 1998 Spencer, South Dakota, storm. Part II: Comparison of observed damage and radar-derived winds in the tornadoes. Monthly weather review, 133(1), 97-119.

Yousef, M. A., & Selvam, P. R. (2016a). Effect of equivalent height, surface area and volume of the dome to prism on tornado forces using CFD. In Proceedings of the 8th International Colloquium on Bluff Body Aerodynamics and Applications.

Yousef, M. A., & Selvam, P. R. (2016b). The influence of tornado's size on forces on dome and regular cubic building using CFD. In Proceedings of the 4th American Association for Wind Engineering Workshop.

Yousef, M. A., & Selvam, P. R. (2017). The influence of tangential to translational velocity ratio on tornado force coefficients on building using CFD. In Proceedings of the 13th Americas Conference on Wind Engineering, May 21-24, Gainesville, Florida, USA.

Yousef, M. A., Selvam, P. R. & Prakash, J. (2018). A comparison of the forces on dome and prism for straight and tornadic wind using CFD model. Wind and Structures, 26(6), 369-382.

Yuan, F., Yan, G., Honerkamp, R., & Isaac, K.M. (2017). Numerical Simulation of Laboratory Tornado Simulator that can Produce Translating Tornadoes. Journal of Wind Engineering and Industrial Aerodynamics. Under review.

Zhao, Y., Yan, G., Zu, J., Yuan, F., & Isaac, K. M. (2016a). Comparison on wind effects of tornadic and straight-line wind fields on spherical dome structures. In Proceedings of the 8th International Colloquium on Bluff Body Aerodynamics and Applications, June 7-11Boston, Massachusetts, USA.

Zhao, Y., Yan, G., & Hua, X. (2016b). Investigation of Wind Effects of Tornadoes on Dome Structures. In Proceedings of the 1st International Symposium on Flutter and its Application, May 15-17, Tokyo, Japan.

Zu, J., Yan, G., & Li, C. (2016). Investigation of wind pressure of translating tornado on spherical dome structures. In Proceedings of the 8th International Colloquium on Bluff Body Aerodynamics and Applications, June 7-11, Boston, Massachusetts, USA.

IV. MODIFYING G TO CONSIDER DYNAMIC IMPACT OF TORNADOES FOR ACHIEVING TORNADO-RESISTANCE DESIGN

Tiantian Li and Guirong Yan

ABSTRACT

In current wind design practice, ASCE 7-16, dynamic impact of wind loads on civil structures is reflected on gust-effect factor, *G*. For straight-line wind field, a single value of 0.85 is used for rigid structures. For tornadic wind field, *G* for rigid structures is simply increased from 0.85 to 0.9. In fact, a tornado is frequently translating while rotating, and the induced wind pressure is non-stationary, which is significantly different from straight-line winds. Therefore, in this study, systematic computational fluid dynamics simulations are conducted to investigate non-stationary characteristics of tornadoes and their dynamic impact on civil structures, and then, *G* is determined based on dynamic structural responses to reflect dynamic impact of tornadoes. The obtained results show that the numerically simulated *G* is about 34% higher than the *G* defined in ASCE 7-16. To achieve sufficient structural capacity against tornado-induced wind loads, fully reflecting dynamic impact of tornadoes, *G* should be increased in ASCE 7-16.

1. INTRODUCTION

In recent years, tornadoes have become a significant cause of injury, death, and property loss in the US. They cause an average of $10B of property loss each year (Lott

et al. 2012). In 2011 alone, the tornado-induced property loss exceeded $20B and 550 people were killed (FEMA 2012). For example, in the May 22, 2011, Joplin, MO Tornado, 161 people were killed, and 83.8% fatalities (135 out of 161) were related to building failure; of these building failure-related fatalities, 54.8% (74 out of 135) occurred in residential buildings (Kuligowski et al. 2014). Therefore, it is imperative to develop science-based building codes in order to provide a better level of occupant protection from tornadoes and to minimize building damage.

Currently, tornadoes are required to be considered only when designing such critical structures as nuclear facilities, storm shelters or tornado safe rooms by following ANS 2.3, ICC 500 and FEMA P-320/FEMA P-361, respectively (ANS 2011, ICC 2014, FEMA 2014, FEMA 2015). “Tornadoes have not been considered in the wind load provisions” for normal civil structures , based on ASCE/SEI 7-16 *Minimum Design Loads for Buildings and Other Structures* (ASCE 2016), which governs the structural design under wind loads. Actually, ASCE 7-16 commentary does provide information and design guidance for design tornadic wind loads, but they are not mandatory. Unfortunately, some parameters in the related equations in ASCE 7-16 to calculate tornadic wind pressure and wind loads are based on improper simplification or assumptions, due to the limited understanding of tornado-structure interaction. For example, when calculating the pressure on each wall/roof of a structure, the commentary simply applies the exterior pressure coefficient (C_p) that is used for straight-line (SL) winds, which ignores the asymmetry of wind effects on the two sidewalls when the tornado core radius passes the structure and ignores the symmetry of wind effects around the structure when the tornado center passes a structure; no matter what is the original

design exposure condition, it specifies “must apply Exposure C or D”, which ignores the influence of the presence of surrounding buildings on tornadic wind fields for the original design Exposure B; and it specifies the gust-effect factor (G) as 0.90, which does not reflect the fact that within such a short time, while the tornado passes a structure, the wind angle of attack keeps changing and the wind speed keeps changing (extremely non-stationary).

The study will thoroughly investigate the tornado dynamics and tornado-structure interaction through systematic CFD simulations, and then modify the associated parameters in ASCE 7-16 tornadic wind loading calculation. The focus is to investigate dynamic wind effects induced by the non-stationary characteristics of tornadoes and to reflect this on G. The proposed research will increase fundamental knowledge on the tornado-structure interaction and tornadic wind effects and help to properly determine design tornadic wind loads, which can be used for tornado-resistance design of new buildings and reinforcement of existing buildings. This will contribute to the NIST’s mission of improving building codes and standards against tornadoes and the specific mission of Disaster Resilience Programs (NIST 2014). The remainder of the study is organized as below. Current wind design practice against tornadoes will first be reviewed on related equations for calculating tornadic wind pressure and on the determination of G. Next, a solution will be proposed intending to address the current issue with G. Then, CFD simulations of tornadic wind field and equivalent straight-line wind field will be conducted and compared, in order to investigate the non-stationary characteristics of tornadic wind field and dynamic impact on civil structures. Based on the dynamic structural responses, G will be calculated to reflect the dynamic impact of tornadoes on

the structure and compared to the *G* defined in ASCE 7-16. Finally, conclusions will be drawn.

2. REVIEW ON CURRENT WIND DESIGN PRACTICE AGAINST TORNADOES

2.1. RELATED EQUATIONS FOR CALCULATING TORNADIC WIND PRESSURE

According to ASCE 7-16, "tornadoes have not been considered in the wind load provisions". However, the ASCE 7-16 commentary (Section C26.14) does provide information and design guidance to enable design for reduced property damage or increased occupant protection (not mandatory). This suggests that structural engineering researchers and practitioners have started to re-envision the design for tornadoes in codes and standards (Prevatt et al. 2012), which may be due to the significant fatalities and property loss during recent tornadoes, such as the 2011 Joplin, MO Tornado (Kuligowski et al. 2014), 2013 El Reno, OK tornado and 2013 Moore, OK Tornado (Kuligowski et al. 2013). Unfortunately, some parameters in the related equations for calculating tornadic wind pressure and wind loads in ASCE 7-16 are based on improper simplification or assumptions due to the limited understanding of tornado-structure interaction, which is resulted from a lack of field pressure/velocity measurements and related research. This section will justify why the specification on *G* is improper.

In Section C26.14 of the ASCE 7-16 commentary, two wind pressure computation methods are provided. They are the Extended Method and the Simplified Method. The Extended Method applies the following equations to calculate the velocity

pressure (q) and the wind pressure on structural surface (designated as "surface pressure" in the following, p)

$$q = 0.00256 K_d K_z K_{zt} K_e V^2 \quad (1)$$

$$p = qGC_p - q_i(GC_{pi}) \quad (2)$$

where the design basic wind speed here, V, is taken either as the maximum wind speed for the target design EF scale or from the wind speed map of ICC 500 (ICC 2014), FEMA P-320 (FEMA 2014) or FEMA P-361 (FEMA 2015). Refer to ASCE 7-16 (Chapter 26, Section 26.10; Chapter 27, Section 27.3.1) for the meaning of other parameters. The expressions of Equations (1) and (2) are exactly the same as those for the SL winds (based on the assumption of the atmospheric boundary layer) as outlined in Chapter 27 of ASCE 7-16. The difference lies in that some parameters in these equations are determined in a different way to account for tornadic wind effects.

The Simplified Method combines the changed parameters of the Extended Method into one single multiplier and is intended to provide a simple method to account for various tornado-related design considerations. It claims "two approaches achieve the same results" in ASCE 7-16 Commentary C26.14.4. Therefore, current study only focuses on the Extended Method, more specifically, the specification on *G*.

2.2. THE DETERMINATION OF GUST-EFFECT FACTOR (G)

This section provides some background discussion of *G* and how it is defined in ASCE 7-16 to develop a better understanding of *G* modifier. *G* is used to examine dynamic loading effects on civil structures caused by gustiness in wind. To be specific, it accounts for the loading effects in the along-wind direction due to wind turbulence-

structure interaction and for along-wind loading effects due to dynamic amplification of civil structures. It does not include allowance for across-wind loading effects, vortex shedding, and instability due to galloping or flutter, or dynamic torsional effects.

In ASCE 7-16, *G* is defined separately for SL wind field and tornadic wind field. For SL wind field, different *G* is used for rigid buildings (fundamental natural frequency is greater than or equal to 1 Hz) and flexible buildings. For rigid buildings, either a single, conservative *G* of 0.85 is used or a more accurate *G* is calculated by Equations (3)-(6).

$$G = 0.925\left(\frac{1+0.7g_Q I_{\overline{z}} Q}{1+0.7g_v I_{\overline{z}}}\right) \tag{3}$$

$$I_{\overline{z}} = c\left(\frac{10}{\overline{z}}\right)^{1/6} \tag{4}$$

$$Q = \sqrt{\frac{1}{1+0.63\left(\frac{B+h}{L_{\overline{z}}}\right)^{0.63}}} \tag{5}$$

$$L_{\overline{z}} = \ell\left(\frac{\overline{z}}{10}\right)^{\overline{\varepsilon}} \tag{6}$$

where $I_{\overline{z}}$ is turbulence intensity at height $\overline{z}$; $\overline{z}$ is the equivalent height of the building or structure defined as 0.6*h*; c is 0.30, 0.20, and 0.15 for Exposure B, C, and D, respectively; g_Q and g_v are 3.4; Q is the background component of wind fluctuating response; *B* is horizontal dimension of building measured normal to wind direction, in m; *h* is mean roof height of a building or height of other structure, in m; $L_{\overline{z}}$ is integral length scale of turbulence at height $\overline{z}$; ℓ is 97.54 m, 152.40 m, and 198.12 m for Exposure B, C, and D, respectively; $\overline{\varepsilon}$ is 1/3, 1/5, and 1/8 for Exposure B, C, and D, respectively.

The constant 0.925 is introduced to adjust the design loads in the updated code consistent with the former version (ASCE 1995, Zhou et al. 2002). In current study, the

first natural frequency of the civil structure of interest is 3.9 Hz, which is larger than 1 Hz. Therefore, it belongs to the category of rigid buildings. Then, *G* modifier will be proposed primarily based on rigid buildings. For flexible buildings, *G* can be calculated by Equation (7).

$$G_f = 0.925\left(\frac{1+1.7I_{\bar{z}}\sqrt{g_Q^2Q^2+g_R^2R^2}}{1+1.7g_vI_{\bar{z}}}\right) \quad (7)$$

where g_R is resonant peak factor, and *R* is the resonant component of wind fluctuating response. Since *G* of the flexible structures is not the focus of current study, it is not described in detail here for the sake of brevity. More details about Equation (7) can be found in Section 26.11.5 of ASCE 7-16.

For tornadic wind field, *G* is increased from 0.85 to 0.90 for rigid structures by not considering the 0.925 calibration factor. That is, *G*=0.85/0.925=0.92 (rounding down to 0.9). In fact, a tornado translates while rotating. Assume a tornado passes by a civil structure within 10~15 seconds. Within such a short time, the wind angle of attack keeps changing and the wind speed attacking the structure keeps changing, as the tangential velocity varies along the radius. Even without taking turbulence into account, the tornado-induced wind pressure is non-stationary. Previous research results have shown that when a tornado core passes a structure, the surface pressure fluctuates significantly and the vibration (acceleration) on the civil structure is severe (Li et al. 2018a). Therefore, the dynamic impact of tornadoes should be included in the wind load calculation. This justifies the significance of present study that reflect non-stationary characteristics of tornadoes on *G*.

3. PROPOSED SOLUTION

The improper specification of G is due to limited understanding on the tornado-structure interaction. Field velocity and pressure measurements are valuable to obtain the actual wind effects. However, in spite of recent measurement and reconnaissance efforts, the data on tornadic wind speeds and loading conditions is still limited. This is because tornadoes are violent, short-lived with an average warning lead time of only 10-15 minutes and their tracks are unpredictable (Savory et al. 2001, Simmons and Sutter 2005). Although testing in laboratory tornado simulators has brought about interesting results, experimental testing has its own limitations, such as high cost and reduced scaling. Especially, it is prohibitively expensive and time-consuming to systematically investigate a number of cases. One promising area to ameliorate these difficulties is CFD simulations (Natarajan 2011, Liu and Ishihara 2012, Selvam and Millett 2003).

CFD offers particular advantages compared with field measurements and reduced-scale wind tunnel measurements by providing detailed information on the relevant flow variables in the whole computational domain, under well-controlled conditions and without similarity constraints. That is, inflow and boundary conditions, surface roughness, and even air density and temperature can be easily changed; and full intensity and scale of real-world tornadoes can be replicated by CFD simulations if sufficient computational resources are available. By applying CFD simulations, the real-world tornado events and their wind effects on civil structures can be potentially reproduced, and the high cost associated with repeated lab experiments and adjustments can be potentially avoided. Indeed, CFD simulations are also time-consuming. Thanks to

the high-performance computational resources available at MS&T and other organizations (e.g., TACC), systematic case studies can be conducted in parallel with sufficient computational resources.

Considering that CFD simulations still demand validation (Blocken 2014), the CFD models will be first validated using the available field-measured data (although it is rare). Then, based on the validated CFD simulation strategies, systematic CFD simulations will be carried out to thoroughly investigate tornado dynamics and tornado-structure interaction and apply the research findings to modify *G* in the related equations used in ASCE 7-16 tornadic wind loading calculation.

4. SIMULATION OF WIND FIELDS

4.1. SIMULATION OF TORNADIC WIND FIELD

4.1.1. CFD Simulation Model. A civil structure is placed in the wind field to investigate induced wind effects acting on the civil structure. It is assumed to be rigid in the wind field, i.e., non-deformable. The civil structure of interest is a Kiewitt-type K6-7 single-layer spherical dome structure, as shown in Figure 1. Its base diameter is 75 m and its height is 25 m. 462 tubular beam members form a frame for the dome structure, and 294 shells cover the frame.

Simulation of the tornadic wind field is based on a real-world F4 tornado, the Spencer, SD tornado of May 30, 1998 (hereafter “Spencer Tornado”). To simulate the swirling tornadic wind flow, a cylindrical computational domain is created, as shown in Figure 2(a). It consists of two cylinders. The bottom cylinder is 100 m high, resembling

the inflow zone. The top cylinder is 1,000 m high, resembling the convection zone. The radii of the two cylinders are both 800 m. The boundary conditions include velocity inlet, pressure outlet, symmetry for the top and side boundary surfaces, and no-slip wall for the ground and the surface of the dome structure. The radius of the pressure outlet is 340 m.

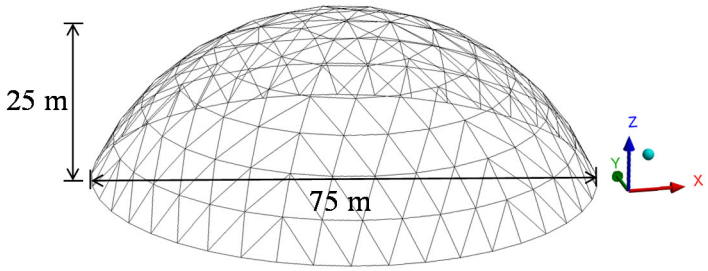

Figure 1. Spherical dome structure.

To simulate tornado translating over the dome structure, the bottom cylinder is divided into 5 regions, as shown in Figure 2(a). The middle three regions (3, 4, and 5) are served as the tornado translating path. Detailed illustration about tornado translating is shown in Figure 2(b). The dome structure is made to move in the opposite direction to the direction of tornado translating in order to establish relative movement. As shown in Figure 2(b), the dome structure starts at 360 m on the X axis (t = 0 s), translates along the negative X direction, and stops at -360 m on the X axis (t = 48 s). Its translating speed is 15 m/s, which is the translating speed of Spencer Tornado based on the field measurement data (Wurman and Alexander 2005). In the CFD simulation, the dynamic mesh technique is applied to simulate that the dome structure travels inside the computational domain. Besides, to simulate the relative motion between the ground plane

and the tornado, the no-slip wall applied on the ground in the stationary case is changed into moving wall in the tornado translating case.

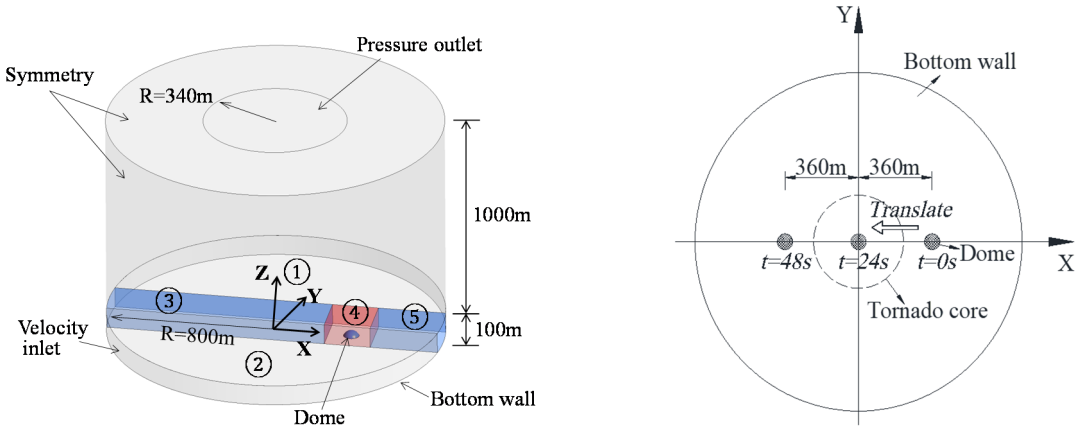

(a) (b)

Figure 2. (a) Computational domain of the simulated tornadic wind field; (b) Schematic diagram of the simulation of tornado translation.

Hybrid mesh is applied to the computational domain, as shown in Figure 3. Region 4 (Figure 2(a)) is meshed into unstructured grids, while the remaining parts are meshed into structured mesh. The inflation grid sizing is applied to the ground surface and the dome surface. The height of the first layer is 0.002 m and the corresponding Y+ value is 250 using flat-plate boundary layer theory. The growth rate is 1.2 and a total of 36 layers is used. Fine mesh is applied to the bottom cylinder and coarse mesh is applied to the top cylinder. In total, 1,843,280 cells are generated.

The large eddy simulation (LES) is adopted in the CFD simulation. Large scales of the turbulent flow field are resolved directly, and the non-resolvable small scales are considered by a subgrid-scale model, i.e., dynamic Smagorinsky-Lilly model. Filtered time-dependent Navier-Stokes equations are solved by the segregated implicit solver with

the SIMPLEC (Semi-Implicit Method for Pressure Linked Equation-Consistent) method. The simulation is first run for 300 s for the stationary case (with the dome not moving) and then another 48 s for the translating case (with the dome moving). The time step of the simulation is 0.01 s. During the translating motion, the dynamic mesh is turned on. More details about the CFD model can be found in Li et al. (2018a).

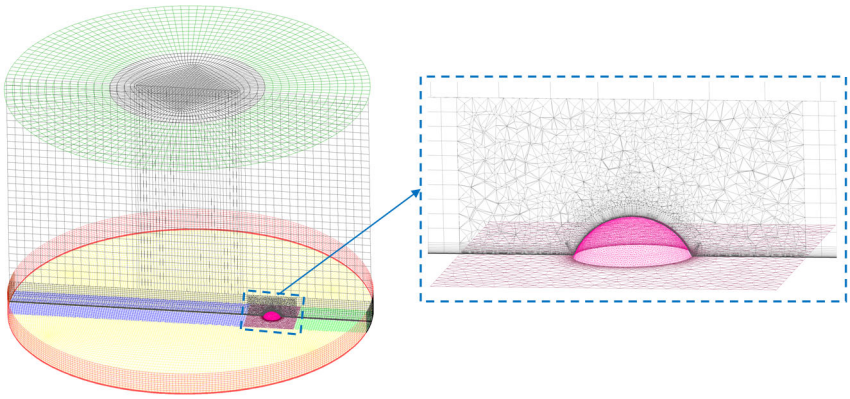

Figure 3. Mesh strategies of the computational domain (tornadic wind field).

4.1.2. Velocity Input at the Velocity Inlet. An inflow with tangential and radial velocity components, as expressed in Equations (3)-(4), enters the velocity inlet and exits from the pressure outlet. They are determined based on radar-measured data at a location 800 m away from the tornado center through the height of 320 m. More details about the determination of velocity input can be found in Li et al. (2018a).

$$V_t = 20.61\left(\frac{z}{20}\right)^{0.1774} \tag{3}$$

$$V_r = \begin{cases} -31.14\left(\frac{z}{20}\right)^{0.169}, & z < 20 \text{ m} \\ 45.14\left(\frac{z}{20}\right)^{0.1826} - 76.48, & z \geq 20 \text{ m} \end{cases} \tag{4}$$

where z is the height above the ground.

Figure 4 shows the time- and space-averaged profile as a function of radial distance at the elevation of 25 m. Tornado center is located at the radial distance of 0 m. Core radius of the simulated tornado is 170 m and the corresponding maximum tangential velocity is 73 m/s.

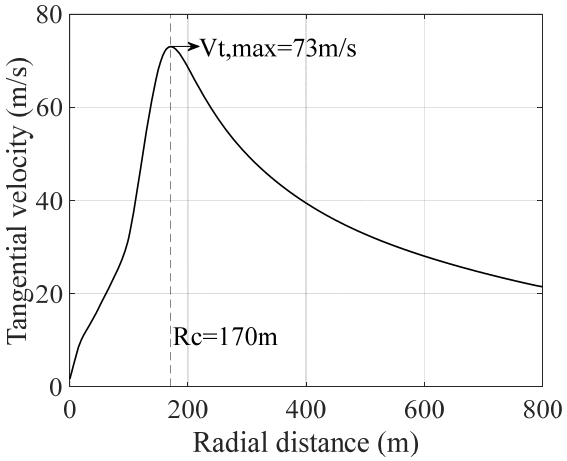

Figure 4. The averaged tangential velocity profile along radial distance at the elevation of 25 m.

4.2. SIMULATION OF EQUIVALENT STRAIGHT-LINE WIND FIELD

4.2.1. CFD Simulation Model. To simulate the equivalent SL wind field, a rectangular computational domain is established as shown in Figure 5. The origin of the coordinate system is at the center of the dome structure. The domain is 30H in streamline direction (X axis), 16H in spanwise direction (Y axis), and 8H in wall-normal direction (Z axis), where H is the height of the dome apex (25 m). The blockage rate of the dome structure in the wind field is 1.7% based on the projected area of the dome structure (1355 m^2) and the cross-sectional area of the computational domain. The dome structure is enclosed by an inner box to generate finer mesh around it. The dimensions of the inner

box is 6H×6H×2H. The boundary conditions include velocity inlet, pressure outlet, no-slip wall for ground and the dome surface, and symmetric boundary for the top and side walls. The center of the dome structure is 10H from the inlet plane and 20H from the outlet plane.

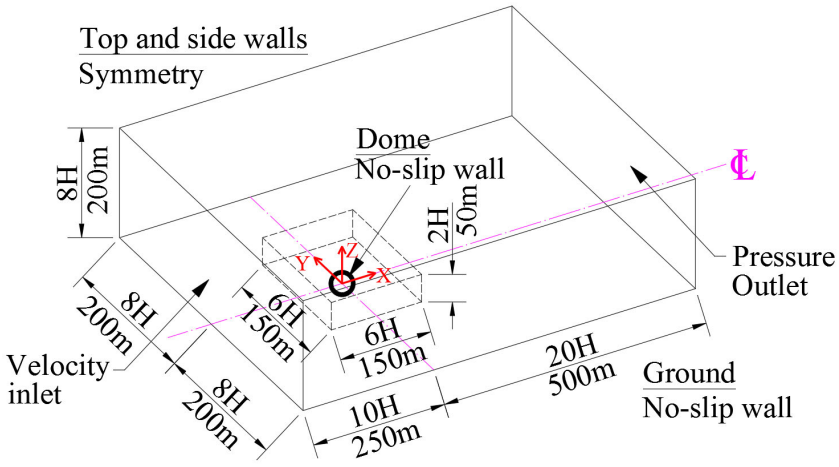

Figure 5. Computational domain and boundary conditions of the equivalent straight-line wind field.

Hybrid mesh is applied to the computational domain, as shown in Figure 6. Unstructured mesh is applied to the dome surface and the inner box. Structured mesh is applied to the rest parts. The same inflation grid is applied to the ground and the dome surface as in the tornadic wind field, that is, the thickness of the first layer is 0.002 m, the growth rate is 1.2, and a total of 36 layers is applied. Finer mesh is generated within the inner box than the remaining parts. In total, 1,685,652 cells are generated. The simulation setup is similar to that of the tornadic wind field. LES and dynamic Smagorinsky-Lilly model are used to model turbulence. The simulation is run for 75 s. The time step of the simulation is 0.001 s.

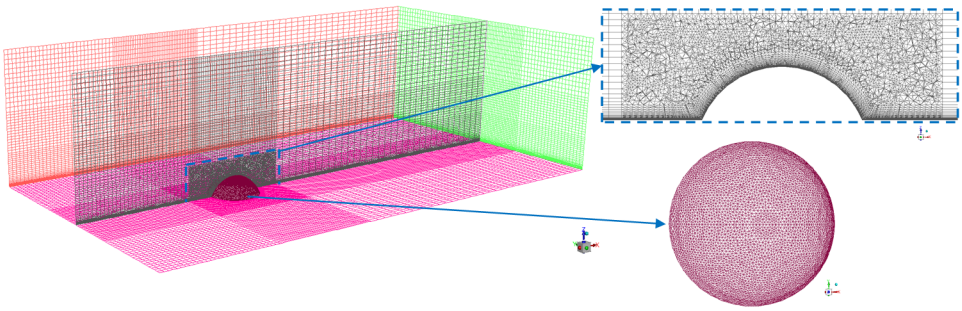

Figure 6. Mesh strategies of the computational domain (straight-line wind field).

4.2.2. Velocity Input at the Velocity Inlet. Velocity input at the velocity inlet follows the power law, which is shown in Equation (5) (Simiu and Scanlan, 1986).

$$\bar{V}(z) = \bar{V}(z_{ref}) \times (\frac{z}{z_{ref}})^{1/\alpha} \quad (5)$$

where z is the vertical distance above the ground; z_{ref} denotes reference height, which is taken as the height of the dome apex (25 m); $\bar{V}(z_{ref})$ denotes velocity at z_{ref}, which is taken as the time- and space-averaged maximum tangential velocity (73 m/s) at the dome apex in the tornadic wind field; α is a function of roughness terrain, which is taken as 9.5 based on ASCE 7-16 Table 26.11-1 for Exposure C (open terrain). Therefore, Equation (1) is expressed as:

$$V = 73 \times (\frac{z}{25})^{1/9.5} \quad (6)$$

5. COMPARISON BETWEEN TORNADIC WINDS AND STRAIGHT-LINE WINDS

5.1. WIND PRESSURE ON THE DOME SURFACE

The peak wind pressure on the dome surface (hereafter “surface pressure”) induced by SL winds and tornadic winds are presented in Figure 7. For tornadic winds, a

large drop is observed around tornado center (time=24 s), especially for peak positive pressure. The large drop is caused by the atmospheric pressure drop within the tornado core. The peak positive pressure induced by tornadic winds is 5.53 kPa, and the peak negative pressure is -9.63 kPa. For SL winds, time variation of induced surface pressure is relatively stable. The peak positive pressure induced by SL winds is 2.55 kPa, and the peak negative pressure is -3.61 kPa. In summary, there are two main differences between surface pressure induced by tornadic winds and SL winds: 1) A large drop is observed in time variation of tornado-induced surface pressure, which is not found under SL winds; 2) The magnitude of peak pressure induced by tornadic winds is higher than that induced by SL winds, i.e., peak positive pressure of tornadic winds is 1.17 times more than that of SL winds and peak negative pressure of tornadic winds is 1.67 times more than that of SL winds.

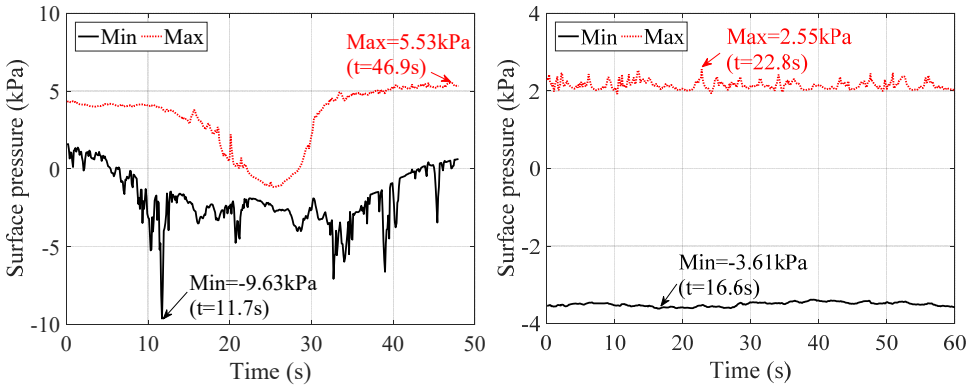

(a) (b)

Figure 7. Peak surface pressure at each time instant induced by: (a) Tornadic winds; (b) Straight-line winds.

Figures 8 and 9 present the distributions of surface pressure induced by the tornadic winds and SL winds at three time instants, respectively. For tornadic winds, the

three time instants are selected as at core radius (170 m, see Figure 4), at tornado center and at 360 m away from tornado center. For SL winds, the three time instants are selected as at 3 s, at 30 s, and at 60 s. The comparison between Figures 8 and 9 reveals that the wind angle of attack keeps changing and the surface pressure keeps changing for tornadic winds while corresponding variations are subtle for SL winds.

To be specific, when the dome structure is at core radius (Figure 8(a)), the wind blows from due south and the surface pressure near the south edge of the dome is positive. When the dome moves to the left side of the tornado center (Figures 8(c)), the windward direction changes to the northwest corner of the dome, and thus large positive pressure is found at that location. On the other hand, for SL winds, the general trend of the surface pressure distribution is unchanged, that is, the wind always blows from due west, and positive pressure is generated near the west edge of the dome and negative pressure around the dome apex. The locations of peak positive and negative pressure are almost the same for the three time instants.

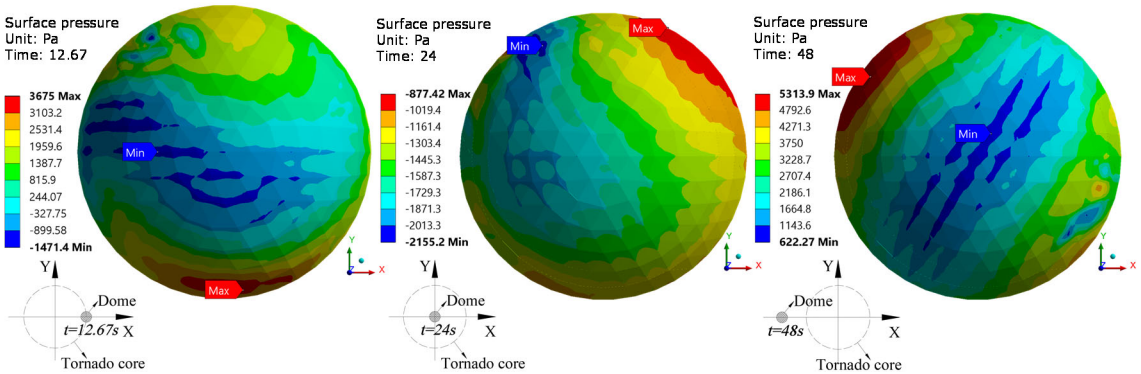

(a) (b) (c)

Figure 8. Wind pressure on the dome surface induced by tornadic winds: (a) At core radius; (b) At tornado center; (c) At 360 m away from tornado center.

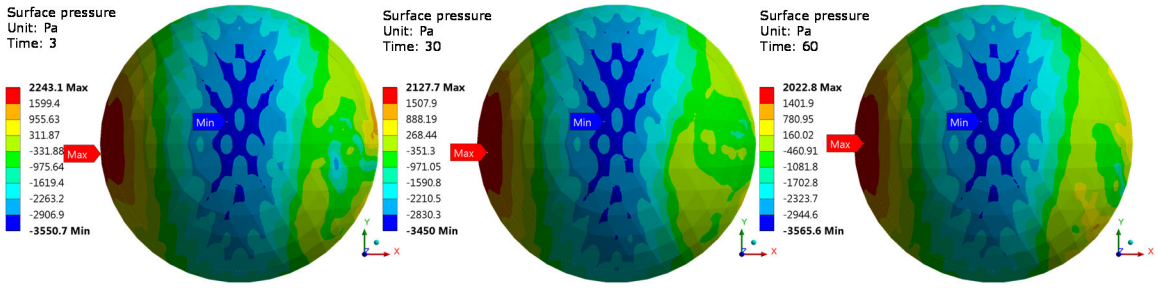

(a) (b) (c)

Figure 9. Wind pressure on the dome surface induced by straight-line winds: (a) At 3 s; (b) At 30 s; (c) At 60 s.

To identify the fluctuation patterns, time histories of surface pressure at three points are presented in Figure 10 for tornadic winds and in Figure 11 for SL winds. The red dots represent the locations of the three points. The time variations of the three points under tornadic winds (Figure 10) generally follow the same tendency, experiencing a large drop around tornado center. Such tendency is consistent with the time variation of peak surface pressure in Figure 7(a). The magtigude of pressure variation for the three points is similar.

For SL winds (Figure 11), the time variations of the three points are more steady. The magnitude of pressure variation for point 1 (close to dome edge) is much larger than that for points 2 and 3. It indicates that the airflow on the windward side is more turbulent than that around the dome apex. This is because the airflow breaks into two regions at the stagnation point. At the corner in front of the dome, flow reversal or vortices occurs.

5.2. DYNAMIC RESPONSES OF THE DOME STRUCTURE

Time histories of surface pressure induced by tornadic and SL winds obtained from CFD simulations are imported onto the finite element model (FEM) of the dome

structure in Computational Structural Dynamics (CSD) simulations, determining dynamic structural responses. The FEM of the dome structure is shown in Figure 12. The beam members are modeled by Beam 188 and the shells are modeled by Shell 181. The bottom joints of the dome structure are assumed to be fixed. The first natural frequency of the dome structure is 3.9 Hz based on the model analysis. More details about the setup of the FEM and modal analysis can be found in Li et al. (2018a).

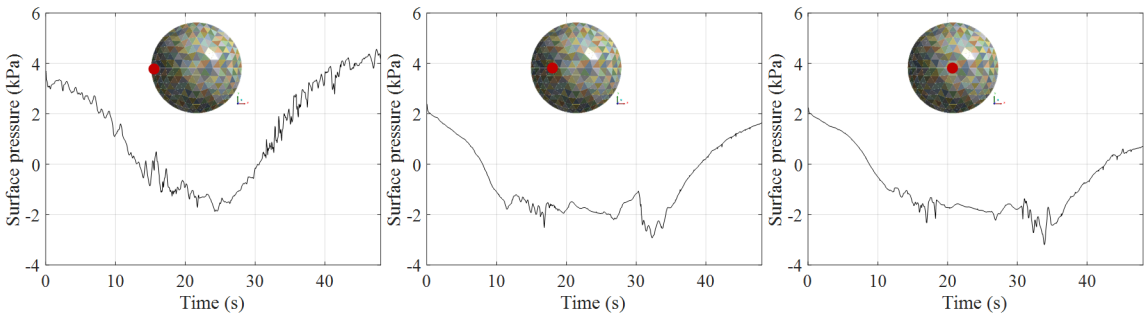

Figure 10. Time history of surface pressure induced by tornadic winds: (a) At point 1; (b) At point 2; (c) At point 3.

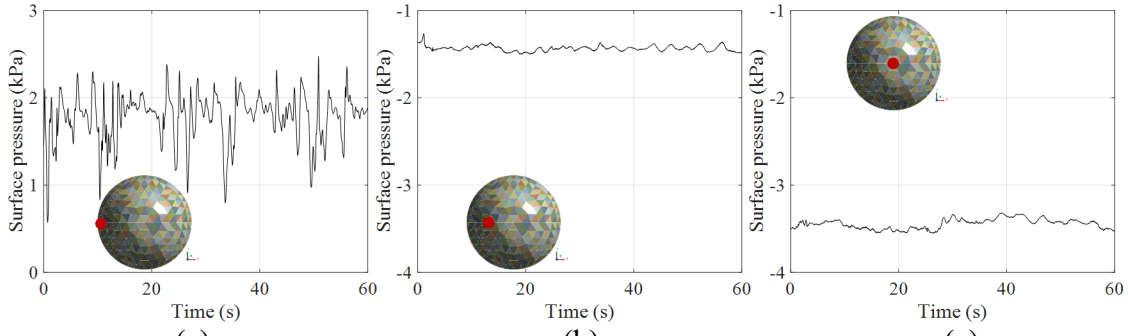

Figure 11. Time history of surface pressure induced by SL winds: (a) At point 1; (b) At point 2; (c) At point 3.

Figure 13 presents the maximum displacement of the dome structure at each time instant induced by tornadic and SL winds. With respect to tornadic winds (Figure 13(a)),

the time variation of maximum displacement is consistent with the trend of peak surface pressure in Figure 7(a). Relatively larger displacement occurs when the dome structure is far away from the tornado center, where the dome structue is undertaken by pure positive pressure. Around the tornado center, the dome structure is sorely covered by negative pressure resulted from the atmosphereic pressure drop, but the induced structural displacement is very small. This is because the displacement caused by the negative pressure at this time instant is balanced out by the displacement caused by positive pressure at previous time instants. Overall, the peak tornado-induced structural displacement is 0.153 m occurred at 47.4 s. Figure 14(a) presents the deformation profile of the dome structure at this time instant, mainly exhibiting inward deformation.

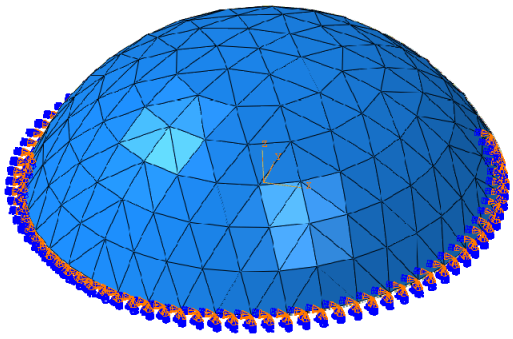

Figure 12. FEM of the dome structure in CSD simulations.

With respect to SL winds, the development of maximum displacement over time is more steady, slightly vibrating around the mean value of 0.0512 m. The overall peak structual displacment induced by SL winds is 0.0617 m. The deformation profile of the entire dome structure at this time instant is presented in Figure 14(b). Inward deformation is formed on the leeward side and outward deformation is formed around the dome apex,

which is consistent with the tendency of surface pressure distribution under SL winds (Figure 9).

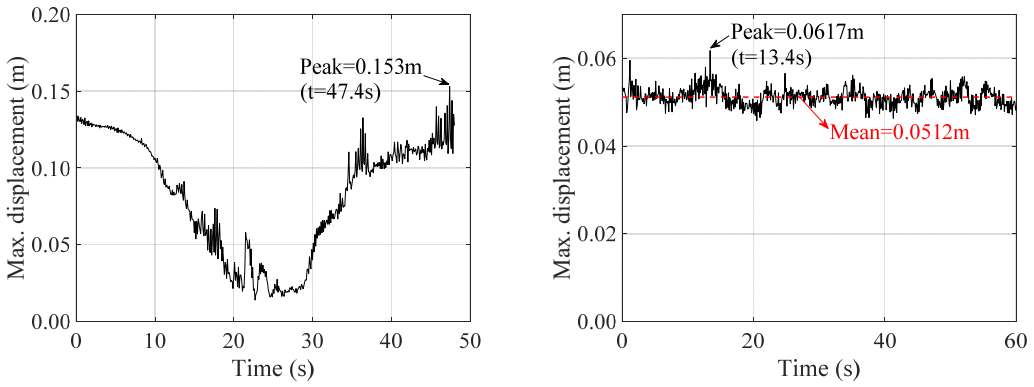

(a) (b)

Figure 13. Maximum displacement of the dome structure at each time instant induced by: (a) Tornadic winds; (b) Straight-line winds.

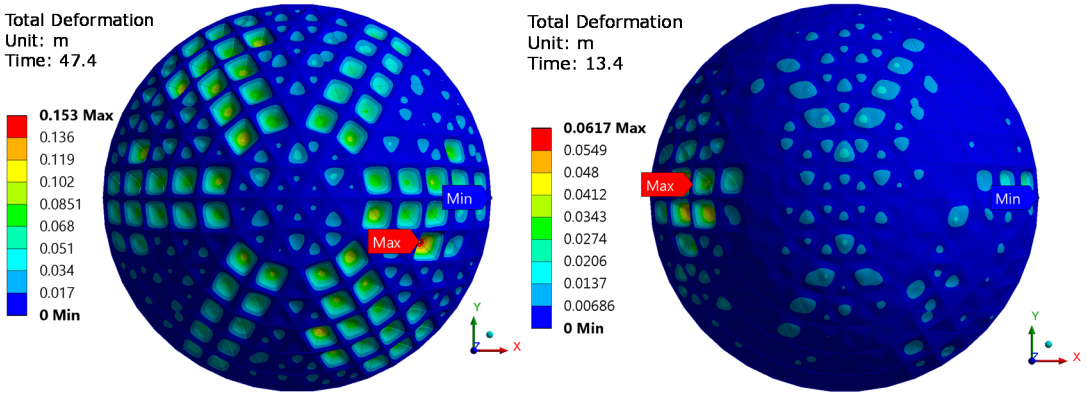

(a) (b)

Figure 14. Deformation profile of the dome structure induced by: (a) Tornadic winds; (b) Straight-line winds.

Time histories of structural displacement at three representative points of the dome structure are presented in Figure 15 for tornadic winds and in Figure 16 for SL winds. The red dots represent the locations of the three points.

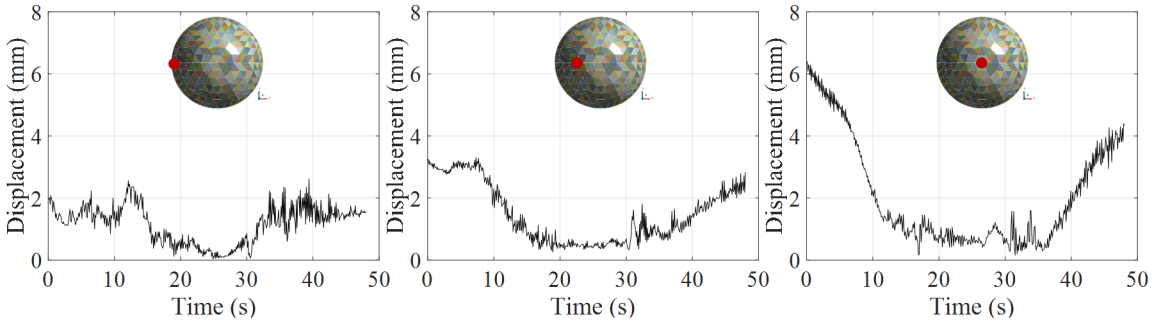

Figure 15. Time history of displacement induced by tornadic winds: (a) At point 1; (b) At point 2; (c) At point 3.

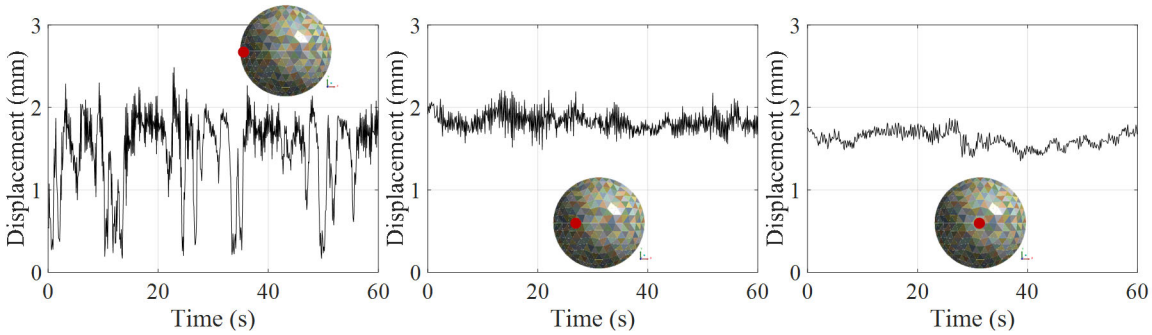

Figure 16. Time history of displacement induced by SL winds: (a) At point 1; (b) At point 2; (c) At point 3.

6. DETERMINATION OF *G*

To reflect non-stationary characteristics of tornadoes and their dynamic impact on the dome structure, *G* is calculated based on dynamic responses of the dome structure. First, the time variations of maximum displacement induced by tornadic winds and SL winds (Figure 13) are averaged every 3 s, respectively. To be more specific, as presented in Figure 17, the time history of maximum displacement is averaged from 0 to 3 s, from 3 to 6 s, from 6 to 9 s, and so on. Second, within each 3 s, the peak value is selected from

the time history of maximum displacement and defined as U_{3s}. The mean value is defined as $\overline{U}_{3s}$. Then, within this 3 s, G_{3s} is defined as the ratio of U_{3s} and $\overline{U}_{3s}$ ($G_{3s} = U_{3s}/\overline{U}_{3s}$). For example, in Figure 18, within 0-3 s under SL winds, U_{3s} is 0.0595 m and $\overline{U}_{3s}$ is 0.0520 m, and G_{3s} is 1.144 (0.0595 m/0.0520 m). G_{3s} is repeatedly calculated for each 3 s, and a series of G_{3s} are obtained, as presented in Figure 19. Third, the final *G* reflecting the dynamic impact of the wind field is defined as the peak value among the series of G_{3s}. Therefore, final *G* in the tornadic wind field is G_T =1.839 and final *G* in the SL wind field is G_{SL} =1.147. The ratio of G_T to G_{SL} is 1.60 (1.839/1.147).

As defined in ASCE 7-16, for tornadic wind field, *G* is increased from 0.85 to 0.90 for rigid structures. Therefore, the ratio of G_T to G_{SL} is 1.06 (0.90/0.85), which is about 34% lower than the simulated results. This suggests that *G* defined in ASCE 7-16 should be increased in order to fully reflect the dynamic impact of tornadoes.

7. CONCLUSIONS

In this study, CFD simulations are employed to reflect the dynamic impact of tornadoes on gust-effect factor, *G*, in ASCE 7-16. First, both tornadic wind field and equivalent straight-line wind field are developed and compared, regarding the obtained wind pressure acting on the structural surface and induced dynamic responses of the structure. Then, *G* is calculated based on dynamic responses of the structure induced by both wind fields. The obtained results show that building design should consider dynamic impact of tornadoes, and *G* defined in ASCE 7-16 should be increased in order to sufficiently reflect dynamic impact of tornadoes.

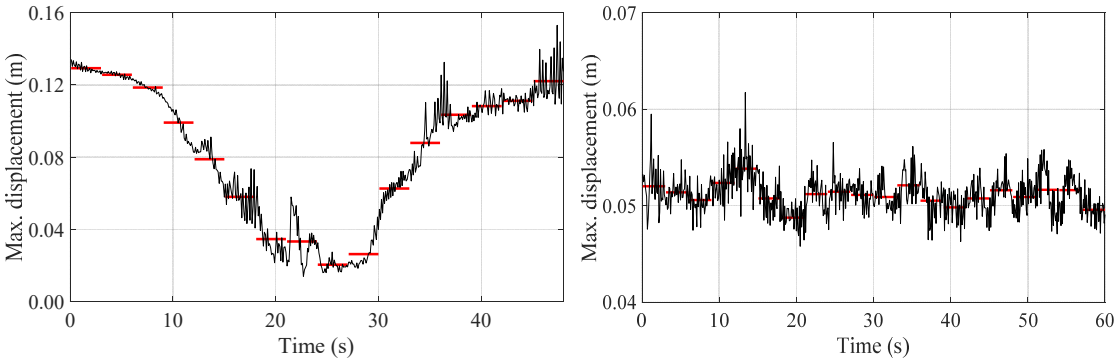

Figure 17. 3-s averaged maximum displacement: (a) Tornadic winds; (b) Straight-line winds. Note: black line represents time variation of maximum displacement and red line represents 3-s averaged value.

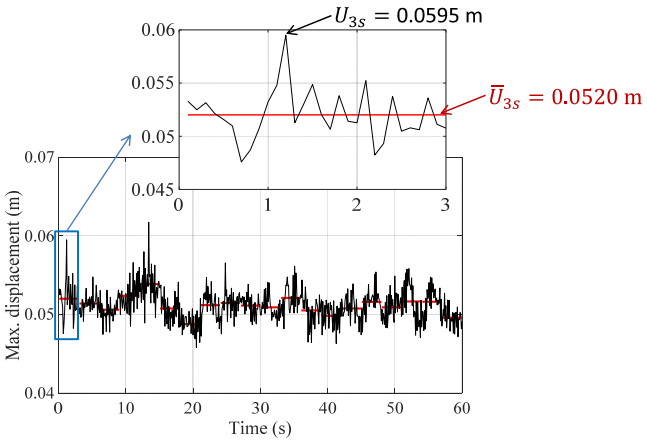

Figure 18. Definition of U_{3s} and $\overline{U}_{3s}$.

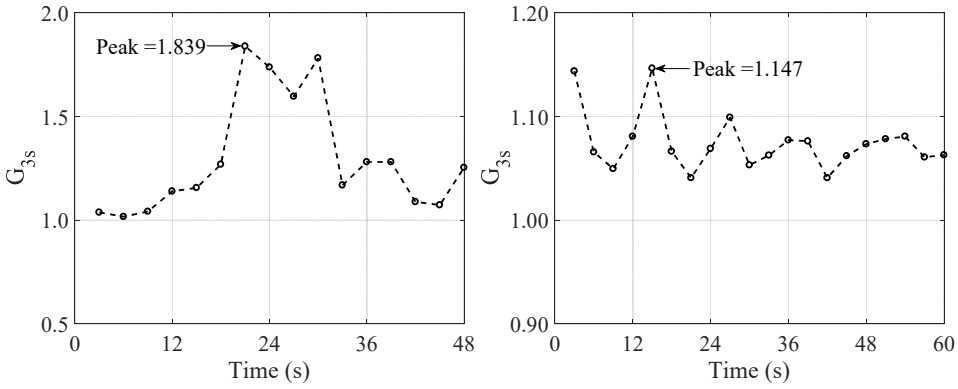

Figure 19. Time history of G_{3s}: (a) Tornadic winds; (b) Straight-line winds.

ACKNOWLEDGEMENT

This work was supported by National Science Foundation, the Hazard Mitigation and Structural Engineering program, through the project of "Damage and Instability Detection of Civil Large-scale Space Structures under Operational and Multi-hazard Environments" [award number 1455709].

REFERENCES

American Nuclear Society (ANS). (2011). "Estimating tornado, hurricane and extreme straight line wind characteristics at nuclear facility sites." *ANSI/ANS-2.3-2011*.

American Society of Civil Engineers (ASCE). (2016). "Minimum design loads for buildings and other structures." *ASCE/SEI 7-16*.

Blocken, B. (2014). "50 years of computational wind engineering: past, present and future." *Journal of Wind Engineering and Industrial Aerodynamics*, 129(6), 69-102.

Davies-Jones, R., Trapp, R. J. and Bluestein, H. B. (2001). "Tornadoes and tornadic storms." *Proc., Severe Convective Storms*, American Meteorological Society, Boston, MA, 167-221.

Fiedler, B. H., and Rotunno, R. (1986). "A theory for the maximum wind speeds in tornado-like vortices." *Journal of the Atmospheric Sciences*, 43(21), 2328-2340.

Federal Emergency Management Agency (FEMA). (2012). "Spring 2011 tornadoes: April 25–28 and May 22, Building performance observations, recommendations, and technical guidance." *Mitigation Assessment Team Report,* FEMA P-908, 512.

Federal Emergency Management Agency (FEMA). (2014). "Taking shelter from the storm: building a safe room for your home or small business." *FEMA P-320*.

Federal Emergency Management Agency (FEMA). (2015). "Safe rooms for tornadoes and hurricanes: guidance for community and residential safe rooms." *FEMA P-361*.

International Code Council (ICC). (2014). “Standard for the design and construction of storm shelters.” *ICC 500-2014*.

Kosiba, K., and Wurman, J. (2010). “The three-dimensional axisymmetric wind field structure of the Spencer, South Dakota, 1998 tornado.” *Journal of the Atmospheric Sciences*, 67(9), 3074-3083.

Kuligowski, E. D., Phan, L. T., Levitan, M. L., and Jorgensen, D. P. (2013). “Preliminary Reconnaissance of the May 20, 2013, Newcastle-Moore Tornado in Oklahoma.” *NIST SP-1164*.

Kuligowski, E. D., Lombardo, F. T., Phan, L. T., Levitan, M. L., and Jorgensen, D. P. (2014). “Technical investigation of the May 22, 2011, tornado in Joplin, Missouri.” *NIST NCSTAR 3*.

Li, T., Yan, G., Yuan, F., and Chen, G. (2018a). “Dynamic structural responses of long-span dome structures induced by tornadoes,” *Journal of Wind Engineering and Industrial Aerodynamics* (under review).

Li, T., Yan, G., and Han, D. (2018b). “Investigate the influence of flow structure of a tornado on wind effects.” *Engineering Structure* (under review).

Liu, Z., and Ishihara, T. (2012). “Effects of the swirl ratio on the turbulent flow fields of tornado-like vortices by using LES turbulent model.” *Proc., 7th Intl. Colloquium on Bluff Body Aerodynamics and Applications*, Shanghai, China.

Lott, N., Smith, A., Houston, T., Shein, K., and Crouch, J. (2012). “Billion dollar US weather/climate disasters, 1980-2011.” *National Climatic Data Center*.

Natarajan, D. (2011). “Numerical simulation of tornado-like vortices.” Ph.D. Dissertation, U. of Western Ontario.

National Institute of Standards and Technology (NIST). (2014). “Measurement science R&D roadmap for windstorm and coastal inundation impact reduction.” *NIST GCR 14-973-13*.

Prevatt, D.O., van de Lindt, J.W., Back, E.W., Graettinger, A.J., Pei, S., Coulbourne, W., Gupta, R., James, D., and Agdas, D. (2012). “Making the case for improved structural design: Tornado outbreaks of 2011.” *Leadership and Management in Engineering*, 12(4), 254-270.

Savory, E., Parke, G. A., Zeinoddini, M., Toy, N., and Disney, P. (2001). “Modeling of tornado and microburst-induced wind loading and failure of a lattice transmission tower.” *Engineering Structures*, 23(4), 265-375.

Selvam, R. P., and Millett, P. C. (2003). "Computer modeling of tornado forces on a cubic building using large eddy simulation." *J. Ark. Acad. Sci*, 57, 140-146.

Simiu, E., and Scanlan, R. H. (1986). *Wind Effects on Structures: Fundamentals and Applications to Design* (3rd ed.), Wiley, Hoboken, NJ.

Simmons, K. M., and Sutter, D. (2005). "WSR-88D Radar, Tornado warnings, and tornado casualties." *Weather Forecasting*, 20, 301-310.

Wurman, J., and Alexander, C. R. (2005). "The 30 May 1998 Spencer, South Dakota, storm. Part II: Comparison of observed damage and radar-derived winds in the tornadoes." *Monthly Weather Review*, 133(1), 97-119.

Zhou, Y., Kijewski, T., and Kareem, A. (2002). "Along-wind load effects on tall buildings: comparative study of major international codes and standards." *journal of Structural Engineering*, 128(6), 788-796.

V. IMPROVE WIND-INDUCED STRUCTURAL RESPONSES ON A CABLE-NET ROOF STRUCTURE USING TWO-WAY COUPLED WIND-STRUCTURE-INTERACTION SIMULATION

Tiantian Li, Guirong Yan, Fangping Yuan, and Genda Chen

ABSTRACT

Computational fluid dynamics (CFD) simulation offers an advantageous tool to quantify wind effects on civil structures. However, previous research is mainly focused on one-way wind-structure interaction (WSI), which neglects the effect of structural deformation on the wind field. This neglection is acceptable if the civil structure is rigid enough. But for flexible structures with large deformation, this neglection might lead to inaccurate estimation of wind effects on civil structures. In order to accurately estimate wind effects on flexible structures, a two-way coupled simulation considering the WSI will be conducted. A flexible cable-net roof structure is first studied under straight-line winds. Then, it will be studied under tornadic winds. The obtained results will help develop science-based building codes for tornado-resistance design and improve disaster resilience in Tornado Alley.

1. INTRODUCTION

Computational fluid dynamics (CFD) simulation offers an advantageous tool to quantify wind effects on civil structures. However, previous research is mainly focused on one-way wind-structure interaction (WSI), which neglects the effect of structural

deformation on the wind field. This neglection is acceptable if the civil structure is rigid enough. But for flexible structures with large deformation, this neglection might lead to inaccurate estimation of wind effects on civil structures. In order to accurately estimate wind effects on flexible structures, a two-way coupled simulation considering the WSI should be conducted.

Studies have been reported regarding the comparison between one-way and two-way coupling methods for numerical analysis of fluid-structure interaction in a broad sense [1-4], e.g. the interaction between pile structures and wave loads. It was concluded that two-way coupled simulation was more reasonable and closer to experimental results compared to one-way coupled simulation. The accuracy of the dynamic response from one-way coupled simulation compared to two-way simulation depended on the relationship of shedding frequency and the natural frequency of the structure. However, two-way coupled simulations are very expensive in terms of computational time. For example, the solution time for two-way coupled simulation was four to five times that for one-way coupled simulation [1]. A new technique of file sharing was proposed to reduce the computational cost [5]. A file (ds.dat file) was generated in ANSYS-MECHANICAL and saved in a separate folder, which was imported and ran in CFX solver. Then, an outer connection was made between the CFX and ANSYS-APDL solver, and finally the structural results were obtained from ANSYS-APDL. In comparison with experimental data, the proposed strategy for two-way coupled simulation was sufficiently precise and certain while the computational cost was reduced.

Regarding the WSI in a narrow sense, Hillewaere et al. [6] investigated the WSI of a closely spaced group of silos by three-dimensional numerical simulations. The

numerical results showed that the one-way and two-way simulations have similar results for a single silo. But, for silos in the group, ovalling vibrations from two-way simulations were significantly larger than that from one-way simulations. Also, the vibration amplitude obtained from two-way simulations was closer to the field observation during a storm in 2002. This demonstrated the accuracy of two-way simulations since the aeroelastic effect and/or interaction between the wake-induced excitation and the structural vibration can be captured. Wind-induced vibrations of flexible shells were studied by Gluck et al. [7], in which time-dependent WSI was considered. A partitioned but fully implicit coupling algorithm was applied to flexible L-shaped plates being loaded by a steady far-field flow. The coupling algorithm connected a three-dimensional, finite volume-based flow solver for incompressible fluids with a finite element code for geometrically nonlinear structural problems using a commercial coupling interface. The obtained results showed that the proposed coupling algorithm was possible to study dynamic interactions for engineering applications.

In this study, two-way coupled WSI simulations will be applied in order to obtain more reliable structural responses of a cable-net roof structure. Straight-line wind field is the focus of current study. The obtained results will facilitate the study of dynamic responses of flexible structures under tornadic winds considering two-way WSI.

2. METHODOLOGY

In this study, the two-way WSI is achieved by coupling the flow analysis (CFD simulation) and structural analysis (finite element analysis). Herein, after the wind

pressure on structural surface (hereafter “surface pressure”) at one time step is obtained from CFD simulation, it will be transferred to the finite element model of the structure though wind-structure interface. Then, a nonlinear, transient structural analysis will be conducted to obtain structural responses for this time step. Next, the obtained structural displacements will be transferred back to the CFD solver to set up the new boundary condition of the wind field for the next cycle of CFD simulation.

3. NUMERICAL SIMULATION SETUP

A saddle-shaped cable-net roof structure is investigated in this study. It spans 36 m and rises 3 m, and the height of the center node of the roof is 6 m. In order to simulate the straight-line winds, a rectangular cuboid computational domain is created (Figure 1a). The inflow is velocity inlet, and the outflow is pressure outlet. The ground is defined as non-slip wall. The top surface of the entire computational domain is defined as zero-shear stress wall. The remaining two side boundary surfaces of the entire computational domain are defined as symmetry boundaries. The velocity profile at the velocity inlet follows the atmospheric boundary layer in form of the power law, that is, $U(z)=53.6(z/6)^{0.28}$, where z is the vertical distance above the ground plane. A transient, incompressible, three-dimensional CFD simulation is conducted using the commercial software, ANSYS FLUENT. Large eddy simulation is used to model the turbulence. Large eddies are resolved with filtered time-dependent Navier-Stokes equations while small eddies are modeled with a subgrid stress model, i.e. the Smagorinsky-Lilly model.

The finite element model of the cable-net structure is developed in ANSYS Mechanical Module. This model is used to perform transient analysis of the roof structure under the wind pressure obtained from CFD simulations to calculate structural responses. The finite element model is shown in Figure 1b, cables are modeled using Link180, but only tension is enabled in this simulation. Shells are modeled using shell181. Each edge of the shell is connected to the adjacent link member by rigid connections along the length. The four walls of the roof structure are assumed to be rigid, and the bottom is assumed to be fixed. The roof is setup as the wind-structure interface to enable data transfer between CFD simulation and structural analysis.

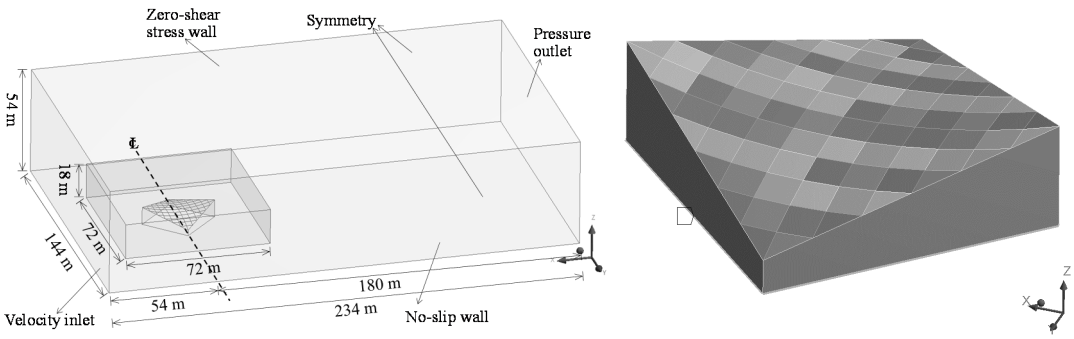

(a) (b)

Figure 1. (a) CFD model; (b) Finite element model of the cable-net structure.

4. NUMERICAL RESULTS

The streamline of velocity on the vertical plane is shown in Figure 2a. Vortices are found in front of the windward wall and in the wake. Distribution of wind pressure on the roof surface is shown in Figure 2b. From the time history of displacement at the

center of the roof (Figure 2c), severe vibrations are observed before 1 s. Then, the variation of displacement levels out and remains constant around 0.06 m.

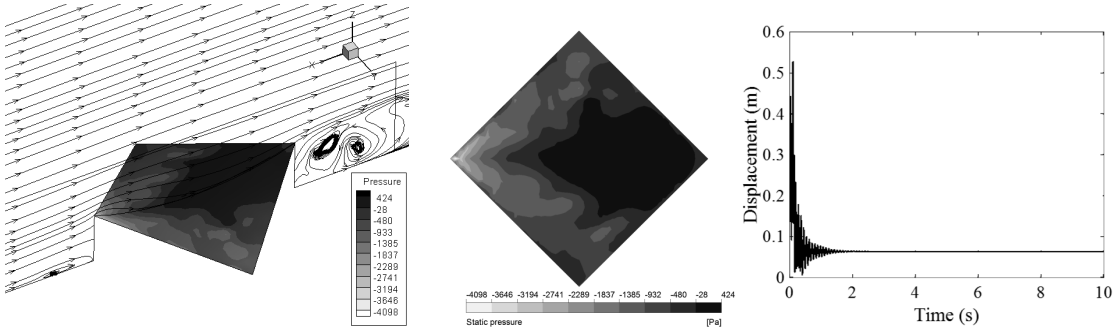

(a) (b) (c)

Figure 2. (a) Streamline of velocity on the vertical plane; (b) Wind pressure distribution on the roof surface; (c) Time history of displacement at the center of the roof.

5. CONCLUSIONS

In this study, dynamic responses of a cable-net structure under straight-line winds are obtained by two-way coupled wind-structure interaction simulation. The wind flow analysis and the structural analysis are coupled to account for the impact of structural deformation on the wind field, which in turn affects the wind pressure on structural surface. Severe vibrations are observed at the center of the roof at the initial stage. Further analysis about the dynamic responses of the cable-net structure under tornadic winds considering WSI will be conducted. The obtained research findings will facilitate the development of tornado-resistance design for flexible structures.

ACKNOWLEDGEMENTS

This work was supported by National Science Foundation, the Hazard Mitigation and Structural Engineering program, through the project of "Damage and Instability Detection of Civil Large-scale Space Structures under Operational and Multi-hazard Environments" [Award No.: 1455709].

REFERENCES

1 F.K. Benra, H.J. Dohmen, J. Pei, S. Schuster and B. Wan, A comparison of one-way and two-way coupling methods for numerical analysis of fluid-structure interactions, Journal of Applied Mathematics, 853560 (2011) 1-16.

2 X.L. Zhu, H. Zhang and H.Q. Ou, Numerical simulation of fluid-solid coupling on offshore platform and wave field, Proc. 35th IAHR World Congress, 2013, vol. iii and iv, pp. 319-320.

3 W. Yan and F. Lv, Numerical simulation of fluid structure interaction between flow and steel pipe pile platform in deep water, World Journal of Engineering and Technology, 4 (2016) 321-326.

4 T.R. Wu, C.J. Huang, C.Y. Wang and C.R. Chu, Dynamic coupling of multi-phase fluids with a moving obstacle, Journal of Marine Science and Technology, 19 (2011) 643-650.

5 S.S. Khalid, L. Zhang, X.W. Zhang and K. Sun, Three-dimensional numerical simulation of a vertical axis tidal turbine using the two-way fluid structure interaction approach, Journal of Zhejiang University SCIENCE A, 14 (2013) 574-582.

6 J. Hillewaere, J. Degroote, G. Lombaert, J. Vierendeels and G. Degrande, Wind-structure interaction simulations of ovalling vibrations in silo groups, Journal of Fluids and Structures, 59 (2015) 328-350.

7 M. Glück, M. Breuer, F. Durst, A. Halfmann and E. Rank, Computation of wind-induced vibrations of flexible shells and membranous structures, Journal of Fluids and Structures, 17 (2003) 739-765.

SECTION

2. SUMMARY, CONCLUSIONS AND RECOMMENDATIONS

2.1. SUMMARY OF RESEARCH WORK

The objective of this research is to investigate the tornado dynamics and its dynamic impact on civil structures in order to properly determine tornadic wind loading on large-scale space structures. This is achieved by systematic numerical simulations combining Computational Fluid Dynamics (CFD) simulation and Computational Structural Dynamics (CSD) simulation (finite element analysis). The research findings will help to develop science-based tornado-resistance building codes, eventually achieving tornado-ready and tornado-resilient communities.

To achieve this research objective, the following research has been conducted. First, wind effects of dome structures induced by straight-line winds are characterized using both wind tunnel testing and CFD simulations, in order to set a baseline for the comparison with tornado-induced wind effects and to gain experience in verification and validation of CFD simulations based on experimental results. In addition, three different turbulence models, Spalart-Allmaras, shear stress transfer (SST) k-ω, and LES models, are employed in the CFD simulations to investigate their influence on the wind effects acting on the dome structure. Second, a tornadic wind field is simulated based on a real-world F4 tornado and the corresponding CFD model is validated using the full-scale radar-measured data. After the validation, a large-scale dome structure is included in the computational domain of the tornadic wind field to determine wind effects acting on the

dome surface. Both wind characteristics of the tornadic wind field and wind effects of the dome structure are investigated regarding different flow structures of the tornadoes. Third, CFD and CSD simulations are combined to investigate dynamic responses of a large-scale dome structure. CFD simulations are conducted to determine tornado-induced wind pressure on the dome surface (hereafter "surface pressure"). The obtained surface pressure is imported onto the finite element model of the dome structure, and then a non-linear, transient analysis is carried out to quantify dynamic responses of the dome structure induced by tornadoes. Fourth, gust-effect factor, *G*, is calculated based on tornado-induced dynamic structural responses, in order to consider non-stationary characteristics of tornadoes and their dynamic impact on civil structures. CFD simulations of both tornadic wind field and equivalent straight-line wind field are conducted and compared. Finally, numerical simulations considering two-way coupled wind-structure interaction (WSI) are conducted to determine dynamic responses of a cable-net roof structure, which takes account into the effect of structural deflection on the wind field and vice versa. Although the two-way WSI is implemented based on the straight-line winds, it will improve the understanding of two-way WSI and will facilitate two-way WSI under tornadic winds, leading to more accurate tornadic wind loading.

2.2. CONCLUSIONS

This section presents the conclusions from the characterization of wind effects and induced dynamic structural responses of large-scale space structures under straight-line winds and tornadic winds. With regard to the wind effects of a dome structure under

straight-line winds obtained from wind tunnel testing and CFD simulations (Task 1), the following conclusions are drawn:

- Three different turbulence models are applied, i.e., Spalart-Allmaras, SST k-ω, and LES models. The simulated results associated with the Spalart-Allmaras model match the wind tunnel testing the best in terms of both the wind pressure distribution on the dome surface and the total suction force F_z. The simulated results associated with the LES model show the poorest accuracy of wind effects on the dome model, which is attributed to the earlier boundary layer separation compared to wind tunnel testing.
- The mismatch between the CFD simulations and the wind tunnel testing is mainly caused by the inaccurate prediction of boundary layer separation. This can be greatly improved by applying a proper turbulence model.
- Although the LES model is able to provide detailed, turbulent flow condition of the wind field, it may not be the best option when averaged quantities are targeted to be matched.

With regard to the verification of the tornadic wind field (Task 2), the following conclusions are drawn:

- The tangential velocity profile and the flow structure on the vertical plane extracted from the simulated tornadic wind field agree well with those extracted from the radar-measured data during Spencer Tornado, which demonstrates the appropriate setup for the CFD simulations.
- A double-celled, single-vortex tornado is formed with a high swirl ratio, while a single-celled, single-vortex tornado is formed with a low swirl ratio; a

touching-down downdraft is observed in the central region of the double-celled tornado, while no downdraft is observed in the single-celled tornado; the core radius of the single-celled tornado is much smaller compared to that of the double-celled tornado while its maximum tangential velocity is much larger, when the velocity input at the velocity inlet is the same; the pressure profile of the single-celled, single-vortex tornado have a narrow, single peak with a higher pressure gradient, but the corresponding profile for the double-celled , single-vortex tornado has a wide, flat distribution.

- Due to the central downdraft, the turbulence intensity of the double-celled tornado is much higher than that of the single-celled tornado in the core region, to be specific, in the region within half of the core radius. Also, the turbulence intensity of the axial velocity is the most significant among all the three velocity components.
- The force and moment induced by the double-celled tornado is more fluctuating and random than those induced by the single-celled tornado, which is caused by the presence of the central downdraft. This suggests that the wind loading induced by the double-celled tornado is more non-stationary than that induced by the single-celled tornado.
- The two drag forces (F_x and F_y) under the single-celled tornado follow a typical trend: 1) they reach their peak values when the dome center moves to the tornado core radius; 2) they change their direction approximately when the dome center passes the tornado center; and 3) F_x is much greater than F_y, indicating that the effect of the tornado sucking the dome towards its center is

much stronger. However, the corresponding variations under the double-celled tornado tend to be more random, and the effect of sucking the civil structure towards the tornado center is not obvious. Similar observations can be found from the two overturning moments (M_x and M_y).

With regard to the dynamic responses of a large-scale space structure induced by tornadic winds (Task 3), the following conclusions are drawn:

- Surface pressure becomes non-stationary when the dome center approaches the core radius of the tornado. At the same time, the dome structure experiences high vibration (high acceleration responses) on the leeward side, where the flow separation and/or potential flow reversal increases the non-stationary characteristics of surface pressure.
- The non-stationary characteristics of tornadic wind pressure is mainly caused by the change in wind angle of attack acting on the dome structure during the tornado translates.
- When the dome approaches the tornado center, existing structural deformation caused by positive surface pressure is cancelled out by some of the negative surface pressure. Therefore, the maximum deformation of the dome structure becomes very small. Although large negative pressure is developed because of atmospheric pressure drop when the tornado center is reached, structural deformation does not reach the worst scenario.
- Wind flow of EF4 and EF5 tornadoes are more turbulent than that of EF2 and EF3 tornadoes, and thus higher dynamic responses are experienced.

With regard to the reflection of gust-effect factor on design tornadic wind loads, the following conclusions are drawn:

- Dynamic impact of tornadoes should be considered when designing large-span dome structures.
- Gust-effect factor defined in ASCE 7-16 should be increased in order to sufficiently reflect dynamic impact of tornadoes on civil structures.

With regard to the dynamic responses of a cable-net roof structure under straight-line winds consider two-way WSI (Task 5), the following conclusions are drawn:

- Large fluctuations are observed of the time history of displacement at the center of the roof before 1 s, indicating severe vibrations at the initial stage.
- For flexible structures, it is necessary to conduct two-way WSI, in order to determine wind-induced vibrations more accurately.
- Further analysis about the dynamic responses of the cable-net roof structure under tornadic winds considering WSI will be conducted. The obtained research findings will facilitate the development of tornado-resistance design for flexible structures.

2.3. RECOMMENDATIONS

Based on the objective and scope of work of this study, the following aspects are recommended for future research:

1. Further investigations are needed to study the modifier of the gust-effect factor for other shapes of structures.

2. Two-way coupled WSI will be conducted in the tornadic wind field to investigate non-stationary characteristics of tornadoes and the induced dynamic impact on flexible structures.
3. Tornado-induced vibration phenomena need to be identified in order to fully understand failure mechanism of civil structures under tornadic winds.

BIBLIOGRAPHY

American Society of Civil Engineers (ASCE). (2016). Minimum design loads for buildings and other structures. ASCE/SEI 7-16.

Blocken, B. (2014). 50 years of computational wind engineering: past, present and future. Journal of Wind Engineering and Industrial Aerodynamics, 129(6), 69-102.

Edwards, R. (2014). Characteristics of supercellular satellite tornadoes. 27th AMS Severe Local Storms Conference, Madison, WI, 1-11.

Federal Emergency Management Agency (FEMA). (2012). Spring 2011 tornadoes: April 25–28 and May 22, Building performance observations, recommendations, and technical guidance. Mitigation Assessment Team Report, FEMA P-908, 512.

Lott, N., Smith, A., Houston, T., Shein, K. and Crouch, J. (2012). Billion dollar US weather/climate disasters, 1980-2011. National Climatic Data Center.

Selvam, R. P. and Millett, P. C. (2003). Computer modeling of tornado forces on a cubic building using large eddy simulation. Journal of the Arkansas Academy of Science, 57(1), 140-146.

Verbout, S.M., Brooks, H.E., Leslie, L.M. and Schultz, D.M. (2006). Evolution of the US tornado database: 1954–2003. Weather and Forecasting, 21(1), 86-93.

Wurman, J. (2002). The multiple-vortex structure of a tornado. Weather and Forecasting, 17(3), 473-505.

Wurman, J., Kosiba, K., Robinson, P. and Marshall, T. (2014). The role of multiple-vortex tornado structure in causing storm researcher fatalities. Bulletin of the American Meteorological Society, 95(1), 31-45.

VITA

Tiantian Li was born in Pizhou of Jiangsu Province, China. She received her Bachelor of Science (B.S.) degree in Civil Engineering in July 2010 from China University of Mining and Technology, Xuzhou, China and Master of Science (M.S.) degree in Bridge and Tunnel Engineering in July 2013 from Tongji University, Shanghai, China. During her graduate study at Tongji, her main research activities involved the seismic study of bridge structures and seismic performance of urban viaduct precast segmental concrete columns.

In 2014, she enrolled as a Ph.D. student in the Department of Civil, Architectural, and Environmental Engineering at Missouri S&T. In the course of her study, she was involved in several projects, including "Damage and Instability Detection of Civil Large-scale Space Structures under Operational and Multi-hazard Environments" and "Breaking Wire Detection and Strain Distribution of Seven-Wire Steel Cables with Acoustic Emission and Optical Fiber Sensors". These projects were supported in part by National Science Foundation (NSF) and by Missouri S&T. Her main research work was focused on non-stationary characteristics of tornadoes and induced dynamic impact on large-scale space structures. She published two journal papers and had five additional papers under review.

In July 2019, she received her Ph.D. in Civil Engineering from Missouri University of Science and Technology.